2018

Crystallization Study Of Polymers Under High Pressure Gas / Supercritical Fluid

Sandra Romero
University of Vermont

CRYSTALLIZATION STUDY OF POLYMERS UNDER HIGH PRESSURE GAS / SUPERCRITICAL FLUID

A Thesis Presented

by

Sandra Romero Diez

to

The Faculty of the Graduate College

of

The University of Vermont

In Partial Fulfillment of the Requirements
For the Degree of Master of Science
Specializing in Mechanical Engineering

October, 2018

Defense Date: June 29, 2018
Thesis Examination Committee:

Patrick C. Lee, Ph.D., Advisor
Ehsan Ghazanfari, Ph.D., Chairperson
Dryver Huston, Ph.D.
Cynthia J. Forehand, Ph.D., Dean of the Graduate College

Abstract

The global demand for polymers especially Polypropylene (PP) foams is increasing rapidly. Foam structures can be very beneficial for producing structural components which can be significantly larger than the raw material formed by volume expansion. In this context, the objective of this work is to develop uniform fine-cell and low-density polymer foams with improved mechanical properties. In order to promote a deeper understanding of the low-density ($<$0.1 g/cc) and microcellular structure (10^8 cells/cm^3), a novel foaming-visualization system was developed. This novel custom-made system captures in situ crystallization-induced foaming behaviors of polymers. The shear effect on bubble and crystal growth processes were investigated independently in an isolated manner. Based on data observed from the visualization system, a two-dimensional model of the foam nucleation process was developed. The model was extended to account for the simultaneous cell nucleation, growth, and collapse processes of the foaming bubbles. By means of connection among neighboring bubbles, secondary nucleation behaviors emerged from multi-bubble interactions were attempted in simulations. Finally, the effects of gas pressure, temperature, additive content, and shear stress were thoroughly investigated for the sake of optimizing the processing conditions and foamed products. Potential applications from these researches lie in the analysis of the resulting micro-/nano-cellular structures and the development of innovative plastic foaming technologies and foams.

"Under the microscope, I found that snowflakes were miracles of beauty; and it seemed a shame that this beauty should not be seen and appreciated by others. Every crystal was a masterpiece of design and no one design was ever repeated. When a snowflake melted, that design was forever lost. Just that much beauty was gone, without leaving any record behind"

Wilson Bentley

Contents

List of Figures

List of Tables

List of Abbreviations

ASTM	American Section of the International Association for Testing Materials
CBA	Chemical Blowing Agent
CD	Cell Density
CSD	Cell Size Distribution
DSC	Differential Scanning Calorimeter
HMS	High Melt Strength
HP-DSC	High Pressure Differential Scanning Calorimeter
HP-SPC	High Pressure Sliding Plate Chamber
LVDT	Linear velocity displacement transducer
PID	Proportional–integral–derivative
PLA	Polylactic Acid
PP	Polypropylene
PS	Polystyrene
RGB	Red Green Blue Image
SAXS	Small Angle X-ray Scattering
SEM	Scanning Electron Microscopy
SST	Shear Stress Transducer
TGA	Thermal Gravimetric Analysis
WAXS	Wide Angle X-ray Scattering
het	Heterogeneous
hom	Homogeneous
sc	Supercritical Fluid
wt%	Weight percentage

List of Symbols

γ	Surface tension	N/m
ρ	Density	g/cc
ρ_0	Density of water	g/cc
τ	Specific volume	cc/g
A	Surface area	mm^2, μm^2
C_0	Concentration of gas molecules	units/mol
G	Rate of linear crystal growth	μm/s
N	Number of nuclei	#
P	Pressure	psi, MPa
R_{cr}	Critical Radius	mum
T	Temperature	°C
T_c	Crystallization Temperature	°C
T_iso	Isothermal Temperature	°C
T_m	Melting Temperature	°C
V	Volume	mm^3, μm^3
W	Work to generate a bubble	J
W_B	Apparent immersed weight	g
X_c	Crystallinity	%
f_0	Frequency factor	-
k	Boltzmann constant	m^2 kg s^{-2} K^{-1}
n	Avrami exponent	-
p	Probability of bubble nucleation	-

r	Bubble radius	μm
t	time	s, min
$t_{1/2}$	Half-time of Crystallization	min

Chapter 1

Introduction and Problem Definition

1.1 Thermoplastic Foams and Their Classification

Thermoplastic foaming is a process during which gaseous blowing agents(s) diffuse into the polymer matrix and later expand and diffuse out of the polymer through inducing a sudden thermodynamic instability (Faruk, Bledzki, and Matuana 2007).

Thermoplastic foams are a type of plastics that are fabricated with porous or cellular structures. These materials offer various advantages over their non-foamed analogs; they are more cost-effective, impact-resistant characteristics, exhibit better buoyancy, insulating properties, and strength-to-weight ratios. Thermoplastic foams are often classified by cell size or cell density, by expansion ratio or bulk foam density, and by cell structure.

First, plastics can be classified by virtue of cell size or cell density into three categories: fine-celled foams, microcellular foams, and nanocellular foams with average cell size above 100 μm, between 10 and 100 μm, between 100 nm and 10 μm, and below 100 nm, respectively. Accordingly, the cell densities for these four kinds of foams are $< 10^6$ cell/cm^3, 10^6-10^9 cell/cm^3, $10^9 - 10^{12}$ cell/cm^3, and $> 10^{15}$ cell/cm^3 (Costeux 2014). In the last decade, efforts have been made to reduce the cell size and

to enhance cell uniformity, in order to improve mechanical and thermal properties thus exhibited (Baldwin and Suh 1992).

Foamed plastics can also be classified on the basis of the expansion ratio (or equivalently the bulk foam density or the void fraction). Expansion ratio is defined as the ratio of polymer density to foam density, which can be categorized as high density (i.e., $<$4 fold), medium density (i.e., between 4 to 10 fold), or low density (i.e., $>$10 fold). High-density foams are often used in structural applications where mechanical properties are important, while low-bulk density foams can be used for shock mitigation, insulation, or rigid packaging.

There is a third category regarding the foam structure indicating the percentage of open or closed cell content. An open-cell foam has cell with openings, or pores, in the cell walls which interconnect with adjacent cells. Open-cell foams can be obtained when each spherical or polygonal cell has at least two pores or two broken faces, and a majority of cell ribs belong to at least three cells. Compared with open-cell or reticulated foams, closed-cell foams generally have higher mechanical strength, better thermal insulation properties, and greater resistance to the moisture and gases due to their structure. Therefore, closed-cell foam structures can have high ability to dampen impact force, which makes them suitable for packaging and cushioning materials (Patrick Lee 2006, Ding 2016).

1.2 Research Motivation

Polypropylene (PP) has been proposed as a substitute for other thermoplastic foam materials in the last few decades. However, some studies have shown that it is challenging to foam PP for several reasons. First of all, PP is a semi-crystalline polymer and gases are difficult to dissolve in the crystalline region; thus, the microcellular structure originated during foaming will be non-uniform. Secondly, the melt strength of PP is relatively weak and this is one reason why cell walls may

not have enough strength to support extensional forces and rupture during foaming producing high cell content. Finally, the viscosity of PP depends on the foaming temperature. That is even small increase in temperature may lead to a very large drop in viscosity and the coalescence of bubbles. This results in relatively narrow operating window for the selection of foaming temperature.

One potential solution to these challenges is the increase of PP crystalline phase. It is well-established that PP's crystallization kinetics can enhance the PP's low melt strength and thereby its foamability (Nofar et al. 2013). The increased melt strength through a network of crystals can result in producing low-density foams by minimizing gas loss. Furthermore, based on experimental observation, it has been shown that the crystalline phase of polymers facilitates the bubble nucleation in polymer foaming. This means, the crystalline phase could be also used as an alternative bubble nucleation agent in the polymer foaming process.

As an example of improved foam behavior, Koga and Saito studied CO_2 bubble nucleation between lamella of polymer crystallites using light scattering measurements and microscope observations (Koga and Saito 2006). A fine-layered porous structure of 500 nm HDPE was obtained. Porous were attributed to CO_2 being excluded from the crystal growth front and pushed into the inter-crystalline amorphous region. However, too high crystallinity may lead to the suppression of the foam expansion due to the resultant excessive stiffness. These two couple processes may cancel or add together.

If the main purpose is to increase crystallinity, this can be done in at least two different ways. First, the significant plasticization effect of CO_2 will increase the segmental mobility of PP and enhance the transport process between the amorphous and crystalline phase. Secondly, the long chain branching in PP increases the size of holes and content of free volume, resulting in the enhancement in segmental mobility. Mobility chain decreases the crystallization barrier and hence tends to increase the crystallization rate and broadened the crystallization temperature (Zhai et al. 2007). However, one must be careful since at high concentration of branching, the

molecular entanglement reduces segmental mobility and hence diminishes the crystallization rate.

Hence, to clarify the complex effect of the crystalline phase on bubble nucleation in polymer foaming, further discussion on the growth rate of the polymer crystalline phase is essential.

1.3 Objectives of the Thesis

The goal of this research is to close the knowledge gap in understanding the microstructural evolution and crystal nucleation/growth mechanisms in batch foam processes. Several research tasks are proposed for this purpose:

- **Task 1**. To develop an innovative foaming visualization system to capture and study plastic foaming processes in situ under static conditions. This system will simulate the batch foaming process under high pressures and should allow direct control of experimental conditions in microscopic-scale (target spatial resolution of ≈ 2 μm.)

- **Task 2**. To develop theoretical and numerical models of cell nucleation and growth mechanisms in batch foam processes. A physics-based model needs to be developed to understand and predict the effects of the gas/supercritical fluid. Experiments will be conducted to verify the model.

- **Task 3**. To develop effective strategies to analyze the crystal formation and foaming of polymers under high pressure gases and various stress states. In particular, direct observation of crystal nucleation and growth phenomena under controlled shear flow has never been achieved in an isolate manner previously under high pressures (up to 3,000 psi CO_2 pressure). It is believed that the overall crystallization rate and crystallinity of PLA and PP can be significantly enhanced due to CO_2 pressure and shear flow.

- **Task 4**. To develop uniform fine-celled PP foams with improved mechanical properties. The target properties are low bulk density (or equivalently at least ten-fold foam expansion) and high cell-population density in the region of 10^9 cells/cm^3. To accomplish the aforementioned research objective, the research will be focused on: (i) the effects of processing parameters such as temperature, blowing agent amount, pressure, pressure drop rate, and material blending on foam morphologies, (ii) the optimization of the processing, and material parameters for achieving the desire foam qualities such as high cell density and high expansion ratio.

1.4 Overview of the Thesis

This thesis is organized into following seven chapters.

Chapter 1 presents an introduction to thermoplastic foams and their classification, commonly used foam processing methods, and current challenges and future outlook for plastic foam industry. The research motivation, objective, and scope of the current research are presented.

Chapter 2 presents a detailed literature review and theoretical background relevant for the thesis topics. Fundamentals of microcellular foaming are introduced, together with background on polymer crystallization and significant techniques to polymer crystallization studies.

Chapter 3 illustrates the development of a novel foaming visualization system to observe plastic foaming processes under uniform and controllable shear stress and shear strain rate. This visualization/measuring system provides a reliable way of determining both rheological and optical properties of plastic simulated under dynamic conditions like that of industrial plastic processes.

Chapter 4 presents the efforts towards the development of a new two-dimensional model of the foam nucleation process. The model was extended to account for the simultaneous cell nucleation, growth, and collapse processes of the foaming bubbles

at different viscosities. The cell size distribution and morphologies obtained from the numerical simulation show good agreement with experimental results qualitatively and quantitatively.

Chapter 5 investigates the crystallization behavior of PLA and PP under various CO_2 pressure conditions using a high-pressure differential scanning calorimeter (HP-DSC) and a novel custom-made sliding plate chamber. Results showed that the PLA crystallization growth rate and nucleation density for the PLA/pressurized CO_2 system can be tuned by increased CO_2 pressure and controlled shear strain and shear strain rates.

Chapter 6 describes the detailed investigation of the material and processing parameters which significantly affect the final foam structure. The effects of temperature, additive type and amount, blowing agent, pressure, pressure drop rate, and blending ratio are reported. Finally, it presents a summary of effective strategies for promoting a high expansion ratio and high cell density foam morphologies.

Chapter 7 serves as a summary of this thesis. A list of major contributions of this thesis is presented.

Chapter 2

Literature Review

2.1 Fundamentals of Microcellular Foaming

2.1.1 Formation of Polymer/Gas Solution

Thermoplastic foams can be produced through various manufacturing methods, such as batch foaming, extrusion foaming, foam compression molding, injection molding, and bead foaming. Microcellular foams were first developed using batch processing and later in compression molding, continuous extrusion, and injection molding in this order (Faruk, Bledzki, and Matuana 2007).

The majority of plastic foams and manufacturing methods are based on the concept of a polymer/gas system under high-pressure. After saturation, a thermodynamic instability is introduced to trigger the bubble nucleation, cell growth, and stabilization. The bubble or cell nucleation starts to occur at the early state when the polymer has been supersaturated with the blowing agent.

The type of blowing agent used in plastic foam processing is a gaseous phase that may be generated by the gas release of a chemical reaction (Chemical Blowing Agent - CBA), the separation of a dissolved gas (Physical Blowing Agent - PBA) or the vaporization of a volatile liquid.

In the early days, chlorofluorocarbons (CFCs) were widely used as blowing agents in industrial practice. But they become less and less common due to the serious ozone depleting effect and they were gradually substituted by hydrofluorocarbons

(HFCs) and hydrocarbons (HCs). As a key feature, the gas blowing agents should have high volatility, and thereby high diffusivity so that they can diffuse into the polymer chain, but not high enough so that they can also be partially retained within the cell structure long enough to promote cell expansion. Therefore, it is a challenge to obtain low foam density and fine-celled microcellular foams simultaneously.

2.1.2 Thermodynamics of Cell Nucleation

Nucleation is a critical step in the production of fine-celled foaming processes. Cell nucleation is refereed to the process during foaming that leads to the formation of a bubble in the polymer or polymer composite matrix (Leung 2009). The sudden change in solubility, upon either temperature or pressure drop is the driving force for the cell nucleation. This force needs to reach a minimum amount for the system to break the free energy barrier. According to the classical nucleation theory, if a cell has a radius smaller than the critical radius R_{cr}, it will collapse. In contrast, if a cell has a radius greater than R_{cr}, it will grow spontaneously in order to minimize the free energy.

Two types of nucleation mechanisms can be observed: homogeneous and heterogeneous nucleations. In homogeneous nucleation, cells are nucleated randomly throughout the polymer matrix. It requires higher energy than heterogeneous nucleation. The theoretical required work to generate a bubble or radius r is given by

$$W = \gamma A - \Delta P V \tag{2.1}$$

where the first term, γA, is the work required to create a bubble with surface tension γ, and surface area, A, and the second term, $\Delta P V$, is the work done by the expansion of gas inside a bubble of volume V. The difference between the two terms is the actual work required to generate a cell. Eqn. 2.1 can be written in terms of volume:

$$W = 4\pi r^2 \gamma - \frac{4}{3}\pi r^3 \Delta P \tag{2.2}$$

Differentiating W with respect to r we obtain:

$$\Delta G = \frac{16\pi\gamma}{3\Delta P^2} \tag{2.3}$$

Finally, the nucleation rate for homogeneous nucleation can be described as follows:

$$N_{hom} = C_0 f_0 \exp\left(-\frac{\Delta G_{hom}}{kT}\right) \tag{2.4}$$

where C_0 is the concentration of gas molecules in the polymer/gas solution, f_0 is the frequency factor of gas molecules joining the nucleus, and k is the Boltzman constant.

In contrast, the rate at which the bubbles nucleate heterogeneously is given by the following equation:

$$N_{het} = C_1 f_1 \exp\left(\frac{-\Delta G^*_{het}}{kT}\right) \tag{2.5}$$

where C_1 is the concentration of gas molecules, f_1 is the frequency factor of gas molecules joining the nucleus, k is the Boltzman's constant, and T is the temperature in K.

G^*_{het} is the Gibbs free energy and can be expressed as follows:

$$\Delta G^*_{het} = \frac{16\pi\gamma^3}{3\Delta P^2} f(\theta) \tag{2.6}$$

where $f(\theta)$ is function of the wetting angle of the polymer-additive gas interface θ.

Therefore, as a main difference between homogeneous and heterogeneous nucleation is that by inserting an additive into the polymer matrix, nucleation is more likely to occur due to lower energy barrier. However, in general, it is difficult to generate a large number of microsized cells using additive because of poor dispersion and agglomeration of the particles in the nanoscale.

2.1.3 Cell Growth and Stabilization

Once cells are nucleated, they will continue to grow until they are either stabilized by cooling or ruptured by overstretching (Wang 2009). Since the pressure inside the cells is greater than the surrounding pressure, cells tend to grow in order to decrease the pressure difference between the inside and the outside of the cell (Klempner and Sendijarevic 2004). There are multiple factors that can affect the cell growth such as viscosity of the polymer, diffusion coefficients, gas concentration, number of cell nuclei, etc.

The amount of growth can be controlled by temperature, pressure, and the amount of shear. In particular, temperature and shear will affect at least two important parameters: diffusivity and melt viscosity. Pressure can modify the driven force during pressure drop.

In polymer processing, maintaining the gas in the polymer matrix by close temperature, pressure, and shear control is essential for achieving good cell growth, and thus, cell morphology. In extrusion dies, for example, the pressure can go below the solubility pressure and some nuclei can be produced. Any small change in temperature or pressure before the die will promote premature cell growth. This will produce the prefoamed extrudate to come out of the die with nucleated cells much bigger than expected. Thus it can be a good way to generate a bicellular structure, but it can be dangerous to have a big pressure or temperature drop before the die exit.

Also premature pressure drop and shear are a big threat to foam injection molding (FIM), especially low-density FIM. The cell nucleated at the gate or even along the cavity if subjected to severe shear because of the high shear from the walls in the narrow injection mold cavity. Near the wall, there is a severe shear and the nucleated cells will be elongated in most cases. The stretched bubbles can easily coalesced because of the increased contact area at high temperature and therefore, these elongated bubbles will grow faster because of the large surface area through which the dissolved gas will diffuse into the bubbles.

As a result, careful control of experimental variables, especially pressure, temperature, and shear in our case, are essential for the proper formation of the foam microcellular structure.

2.2 Polymer Crystallization Kinetics

2.2.1 Polymer Crystal Growth

The polymer crystallization is associated to the alignment of the polymer chains. These chains fold together and form ordered regions called lamellae, which compose larger spheroidal structures named spherulites (Carraher Jr 2003). In multiples studies, where the growth of spherulites has been measured it is found that at a fixed temperature or isothermal conditions, the radius increases linearly with time regardless of the size of the spherulite (Price 1959, Burnett and McDevit 1957, Takayanagi and Yamashita 1956). This implies that the growth process is not controlled by either diffusion of heat. In the temperature region below the melting point the growth rate has an extremely high negative temperature coefficient. As the temperature is lowered, the growth rate increases and then decreases as we approach to the crystallization temperature. Previous theories proposed after the study of temperature coefficients that crystal growth was nucleation-controlled. This concept is useful in explaining why spherulites should form at all. Almost certainly the nucleation controlling growth is heterogeneous in nature, meaning the nucleation is promoted by interfaces or voids between the melt and a solid surface. If the existing crystallites at the boundary between the spherulite and the melt are nucleating, new crystallites will form faster due to secondary nucleation. Then the new crystallites will form preferentially at the spherulite-melt boundary.

There are three facts that must be taken into account for the study of crystal growth: first, the growth is most likely controlled by heterogeneous nucleation; second, the growth produces a dendritic surface or needle-like protrusion of the

boundary into the melt; and third, the crystal structure is capable to twist and alter the optical behavior of the spherulite.

Overall the degree of crystallinity in polymers ranges between 10 and 80%, with spherulites size between 1 and 100 micrometers. The final properties of the material will be determined not only by the degree of crystallinity, but also by the size and orientation of the molecular chains.

2.2.2 The Avrami Analysis

When semi-crystalline polymer crystallize below the melting temperature, it is possible to measure time-dependent spherulitic growth via polarized optical microscopy (POM). Heterogeneous nucleation represents a crystallization mechanism where crystals grow radially outward from nucleation seeds. One requirement of POM is that the focal plane of the microscope and the equatorial plane of the crystal spherulite must be coincident. Then the temperature-dependent growth rate G can be defined by the time rate of change of the radius r of a single spherulite;

$$G(t) = \frac{dr}{dt} \tag{2.7}$$

G is essentially constant during primary growth or early stages of isothermal crystallization, and one can calculate the spherulite radius as follows:

$$r(t) = \int_0^r dr = \int_{t_0}^t G(T)dt = G(T)(t - t_0) \tag{2.8}$$

The volume of one crystal spherulite is then:

$$V = \frac{4}{3}\pi(r(t))^3 = \frac{4}{3}\pi G^3(T)(t - t_0)^3 \tag{2.9}$$

Since all nucleation centers are initialized at $t = t_0$, the number density of nucleation centers N_s is the same as the number of spherulites per unit volume of the polymer. Hence, crystallinity can be defined as the volume fraction of spherulites per volume

of polymer:

$$X_c(t,T) = \frac{4}{3}\pi N_s G^3(T)(t-t_0)^3 \tag{2.10}$$

which is an accurate representation of the crystalline volume fraction during the early stages of spherulitic growth before impingement occurs. The scaling law for this process at early times (meaning $t \sim t_0$) is,

$$X_c(t) = (t-t_0)^n \tag{2.11}$$

where n is the Avrami exponent for dimensionality of crystal growth. As an example, two-dimensional disc-like growth occurs when n ranges from 2.23 to 2.5, whereas for n values higher than 2.5 under isothermal treatments the crystal growth would be three-dimensional spherulitic growth.

In the Avrami analysis, the relative degree of crystallinity of the polymer developed over a time t can be defined as follows:

$$1 - X_c(t) = \exp(-k \cdot t^n) \tag{2.12}$$

where k is the crystallization kinetic constant for the crystal nucleation and growth rate. The modeling equation can be further rewritten into the following equation:

$$\ln(-\ln(1-X_c)) = \ln k + n \ln t \tag{2.13}$$

By plotting $\ln(-\ln(1-X_c))$ versus $\ln t$, the Avrami exponent (n), as well as the logarithm of the crystallization kinetic constant (k) can be determined. In addition, the crystallization half-time ($t_{1/2}$), or time elapsed between the onset of the crystallization and the time at which 50% of the final crystallinity had been developed, should be considered for future crystallization analysis.

2.3 Techniques to Polymer Crystallization Studies

2.3.1 In-situ Visualization

Polarized optical microscopy (POM) has been used to characterize the spherulite nucleation and growth behavior under quiescent conditions (Padden Jr and Keith 1959). The polarized light microscope is designed to observe and photograph specimens that are visible primarily due to their optically anisotropic character. The microscope must be equipped with both a polarizer, positioned in the light path somewhere before the specimen, and an analyzer, placed in the optical pathway between the objective rear aperture and the observation tubes or camera port. Image contrast arises from the interaction of plane-polarized light with a doubly-refracting specimen to produce two individual wave components that are each polarized in mutually perpendicular planes.

Isotropic materials demonstrate the same optical properties when probed in all directions. These materials have only one reactive index and no restriction on the vibration direction of light passing through them. In contrast, anisotropic materials have optical properties that vary with the orientation of incident light with the crystallographic axes. A crystalline polymer will have both amorphous and crystalline areas in varying degrees. The amorphous and crystalline regions will respond to polarized light through interference. When using the dark field setting on the cross polarizer, the amorphous part of the polymer is optically transparent and will appear in the image, while the light passing through the crystalline regions will appear white.

The linear polarizing side of the circular polarizer (if any) must face the observer. In this alignment, randomly polarized ambient light will be linearly polarized before it passes through the retarder side of the film and becomes circularly polarizer. In the case of linear polarizer, the direction of the light does not matter.

2.3.2 High-Pressure Differential Scanning Calorimeter (HP-DSC)

Much fundamental research has been undertaken to characterize the crystallization kinetics of various polymers using regular and high-pressure differential scanning calorimeters (DSC and HP-DSC). High pressure measurements are of great importance from the thermodynamic point of view. The change of pressure enables a better insight into the thermodynamic behavior of materials, and it is often used during production and processing of materials. While high pressure differential thermal analysis (DTA) already exists for a longer time in several laboratories worldwide at pressures up to 1 GPa, the number of high pressure DSCs is very limited (Schmidt et al., 1994).

DSCs are used to measure the heat capacity of materials. Heat capacity is a measure of how much thermal energy a material can store with a given temperature increase. It includes contributions from vibrations of the atoms, translations and rotations of the molecules or molecular segments, phase transitions and chemical reactions.

The measuring system consists of two identical microfurnaces which are mounted inside a thermostatted aluminum block (see Fig. 2.1). The furnaces are made of platinum-iridium alloy, each of which contains a temperature sensor and a heating resistor. During the heating-up, the same heating power is supplied to both microfurnaces via a control circuit in order to change their mean temperature in accordance with the present heating rate. When asymmetry between measurements occurs, for example, as a result of a sample reaction, a temperature difference results between the microfurnace accommodating the sample and the microfurnace containing the reference sample. In the DSC the measurement signal ΔT is always obtained as electric voltage.

For this technique it is not very difficult to have 5 °C and greater thermal lags if sample size and heating rates are not choose wisely. The quantification of thermal lag assumes the small and large samples differ in mass by changing the height, which in turn influences the thermal lag. The other extreme is if the mass changes

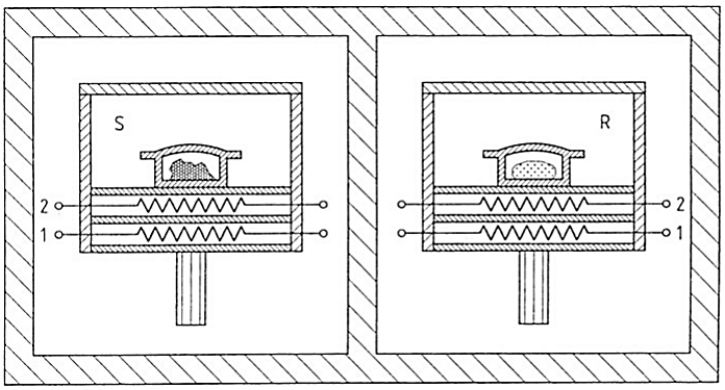

FIGURE 2.1: Power compensation DSC. Set-up of the measuring system. S sample measuring system with sample crucible, microfurnace and lid, R reference sample system (analogous to S), 1 heating wire, 2 resistance thermometer. Both measuring systems - separated from each other - are positioned in a surrounding block at constant temperature) (Höhne, Hemminger, and Flammersheim 1996).

due to an increase in diameter. In theory this would not change the thermal lag since heat flow is from the bottom and top (if a lid pan is used). Most differences in sample size will be a combination of height and diameter. Therefore, it is recommended to minimize the height dimension.

Other relevant parameters that allow direct comparison between measurements are listed below. These parameters should be as similar as possible.

1. The heating rate
2. The thermal conductivity of the sample
3. The mass and heat capacity of the sample
4. The structure of the sample
5. The thermal resistance between sample and temperature sensor
6. The location of the sample in the crucible or measuring system
7. The kind of purge gas in the measuring system

Depending on the modulation of temperature and the underlying heating rate, we can distinguish between two main modes of operation.

1. Heating or Cooling Mode. The heating or cooling rates are always positive and negative, respectively. The advantage of this mode is that all processes only occurring during cooling of the sample are suppressed and the remaining processes are easier to evaluate. The disadvantage is clear from the rather low amplitude which gives a bad signal-to-noise ratio, especially at high pressures.

2. Quasi-Isothermal Mode. In this mode the underlying heating rate is zero and the temperature varies around a constant temperature. The advantage of using this mode is the possibility to determine heat capacities even in the isothermal case what otherwise is not possible.

Characterization of polymers by DSC measurements is mostly carried out in the heating, cooling, or the isothermal modes (see Fig. 2.2). A heating run is advantageous when it is important to characterized the 'as received' glassy state (e.g., glass transition or melting temperatures). Values of T_g and T_m are only meaningful with respect to the chosen experimental conditions (e.g., heating rate). Similarly, degree of crystallinity and crystallization temperature can be characterized under isothermal or cooling modes.

2.3.3 X-ray Scattering, SAXS, and WAXS

Wide-/small-angle X-ray diffractometer (SAXD and WAXD) are other common techniques to characterize the crystalline structure and morphology and degree of perfection, which cannot be characterized using DSC. SAXS/WAXS determine the microstructure and phase behavior of multi-components systems. The basic differences between SAXS and WAXS is the length-scale they correspond to: WAXS detects ordering of individual atoms and SAXS probes larger structures based on electron density differences. In these techniques a monochromatic X-ray beam points to a sample and scattered due to spatial fluctuations of the internal electron density within the material. The particle-particle repulsion (among other inter-particle forces) leads to a so-called short-range order. This means that there is an increased

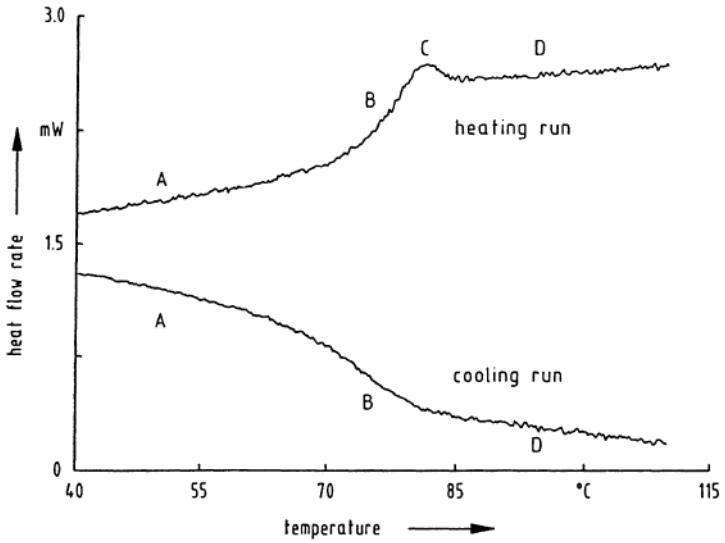

FIGURE 2.2: Typical DSC curves of amorphous polymers in the glass transition region. A: the glassy non-equilibrium state, B: glass transition region, C: enthalpy relaxation peak, D: the equilibrium liquid state (sample:linear epoxi-amine polyadduct, heating and cooling rate: 5 K min^{-1}, Höhne, Hemminger, and Flammersheim 1996).

probability to find a next-neighbor particle at a specific distance. At larger distances, however, the relative positions become more and more random to each other. The results of this short-range order is the build-up of a structure factor in the SAXS pattern.

The peaks in the structure factor become more and more pronounced, when the particle positions become increasingly ordered. When the domain size of ordered particles increases (i.e., formation of long-range order), the system is said to crystallize.

Orientation and its degree can be observed in a 2D scattering pattern by the amplitude of intensity modulation, when measured in a circle around the primary beam. When the sample is randomly oriented (isotropic), such as dilute dispersions or crystal powders, the scattering pattern has equal intensities along concentric circles around the incident beam (see Fig. 2.3). This shows intensity modulations when the sample is partially oriented, such as in sheared liquids or spun fibers (Schnablegger and Singh 2011).

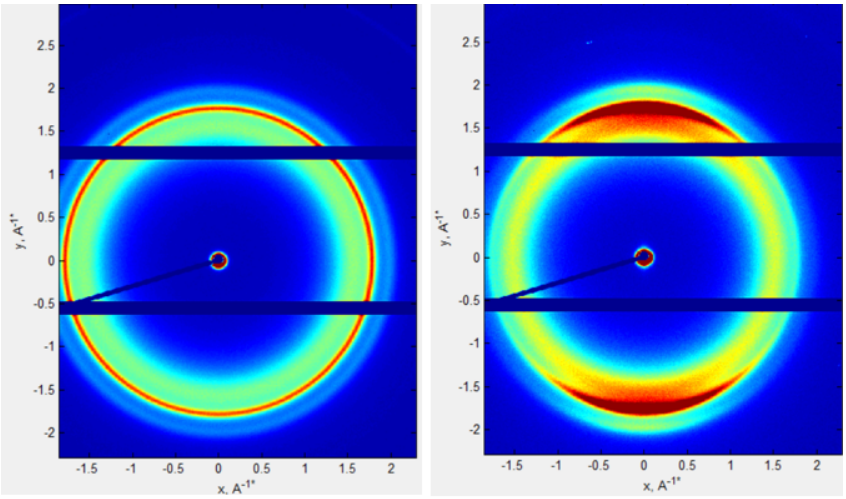

FIGURE 2.3: The 2D scattering of (left) randomly oriented patters of randomly (isotropic) and (right) partially oriented PP samples.

When two media are separated by a sharp interface, the scattered intensity follows an asymptotic law called the Porod's limit. The validity of a Porod's law can cover several decades, giving information about the particle sizes. When various types of particles, with different characteristic scales exist in the sample, it is possible to measure different Porod's law.

Fig. 2.4 shows a typical pair of scattering profiles of foam PP samples at different foaming temperatures. At very smalls angles, the shape of the scattering can be used to give us an idea of the radius of gyration of any distinct structures that are on this range of length scale. At higher angles, if we have a system of relatively uniform particles that is dilute enough for mutual interactions, we might be able to see broad peaks that would also give us information on the shape of the particles. The area under the curve is a measure of the amount of scattering material seen by the X-ray beam. Changes in the invariant are useful to follow crystallization in polymer materials.

In this case, we observe at $q = q*$ a maximum for both intensity curves, which can be attributed to the most probable distance between the center of mass of the crystallites $d* = 2\pi/q*$ with the inter-crystallites structure factor. This distance between crystallites is increasing with percentage crystallinity.

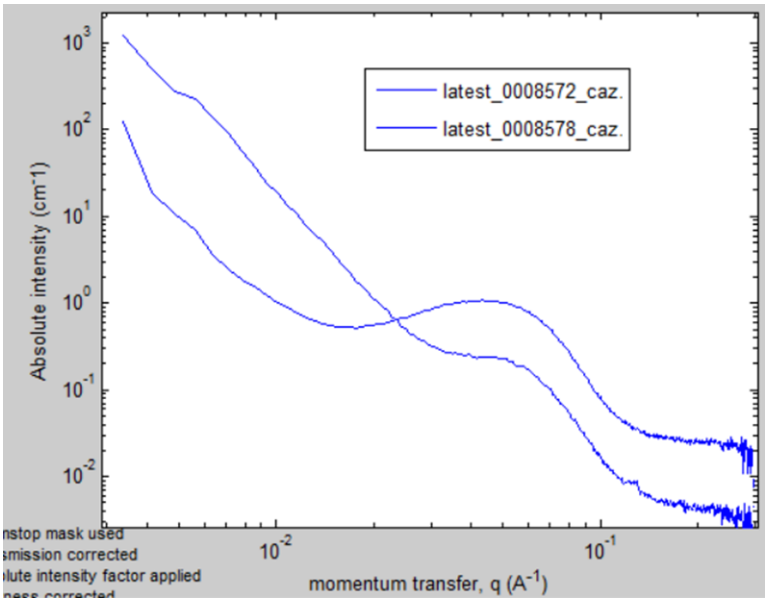

FIGURE 2.4: Example of scattering intensity profile measured between q_{min} and q_{max} until the pair distance distribution (intensity) naturally approaches to zero. The q_{min} value can be adjusted to exclude data that exhibits inter-particle effects or noise.

Chapter 3

In-Situ Visualization and Cell Growth Modeling in a Polymeric Foaming Process

3.1 Introduction

Nucleation is a well-studied problem from boiling to crystal growth. In the foaming process, the cell nucleation is a very critical step, as it directly influences the cell size distribution and thus the mechanical and thermal properties of the polymer foam matrix. The heterogeneous nucleation can start with the formation of micro-bubbles trapped on the inside of small crevices or cavities (Feng and Bertelo 2004). These cavities are randomly distributed across the polymer matrix and act as nucleation sites when temperature and pressure become favorable. Once the micro-bubbles are nucleated, some of them can continue to grow due to the induced energy given to the system. Experimentally, this energy can be provided by lowering the solubility of gas in the polymer/gas solution and by inducing a rapid pressure drop (Kee 2010). The pressure difference between the bubble and the ambient pressure provides the driven force for the gas diffusion through the bubble surface and the bubble growth.

If the dissolved gas concentration within the influence region of the bubble is below the nucleation threshold, new micro-bubbles form around the primary bubble as shown in Fig. 3.1. These bubbles keep on growing by consuming the dissolve gas in their own influence region or cell until reaching a plateau behavior. The simultaneous nucleation and growth of secondary bubbles are attributed to the tensile stresses generated in the surrounding melted plastic of the primary bubble (Wong 2012). Beyond this point, the experimental foaming process showed a significant bubble-to-bubble interaction that may change the overall growing rate for the bubble expansion.

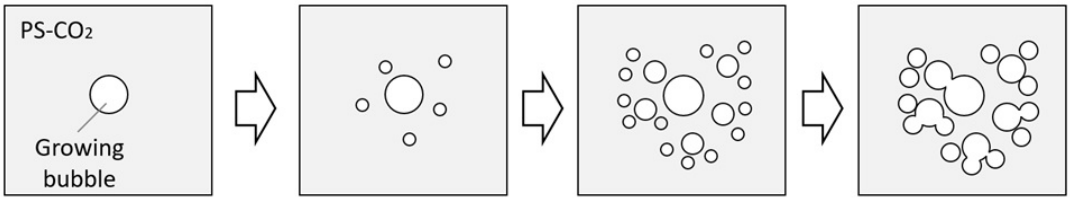

FIGURE 3.1: Schematic sketch of the dynamics of bubble formation in PS-CO_2 system. (Figure adapted from Wong 2012).

Simple computational models have addressed some of these issues in regard to the simultaneous nucleation, cell growth, and collapse, and their effects on the cell size distribution of the final foam structure. In particular, the diffusion-induced bubble growth with simultaneous nucleation and growth has been described by several integral models of coupling of mass transfer and momentum equations (Taki 2008). A simple model of continuous nucleation and detachment of time that scales with the diffusion time was presented in Feng and Bertelo 2004. Here a cell model is developed to simulate the effects of neighboring bubbles, where the term 'cell' makes reference to the union of a single bubble and the surrounding influence volume. The limitation of this work was determined by multibubble systems, where the nucleation rate breaks away from the single cell picture.

Similarly, M. Emami et al. analyzed in the bubble diameter and the cell size distribution of an evolved cellular structure during different stages of the foaming process (Emami, Thompson, and Vlachopoulos 2014). From their visual experiments,

it was observed how the bubble density decreases towards the end of the foaming process due to coalescence effects and the gas redissolution between bubbles. However, these effects were not reflected in the proposed numerical model.

Finally, to account the remaining stages of the foaming process, bubble growth models have been extended in a large number of papers (Tammaro et al. 2016 Venerus 2015, Fan, Mitchell, and Blanshard 1994). As the number of bubbles increases, the gas concentration profile around the bubble decreases and the intercellular distance between cells becomes narrower. This leads to the termination of the bubble nucleation and the coalescence between cells. The coalescence stage and the morphological change of a group of nano-cells in a PS-CO_2 system was tracked by W. Zhu et al. in Zhu, Zhou, and Wu 2006. Experimental results exhibit the shrinkage and eventual collapse of the smaller cells after the bubble-bubble interaction, which makes it difficult for fresh cells to survive in practical foaming processes. Therefore, the cell size distribution concluded to depend on both the nucleation rate, and the bubble growth dynamics (Shafi, Lee, and Flumerfelt 1996).

In the present study, a novel computational model approach is proposed to further clarify the effect of the interaction between neighboring bubbles during the foaming process. Secondary nucleation effects are considered as a result of the interconnected multibubble system. The model proposed was verified based on analyzing the experimental data available in the literature. Since most of the common nucleation models include a good basis on nucleation and cell growth, simultaneous nucleation, cell growth, and collapse were considered in this study.

3.2 Experimental

3.2.1 Materials and Sample Preparation

PS MB3150 used in this study was supplied by AmSty North America LLC. It has a MFI 3g/10 min at 200 °C /5 kg and a glass transition temperature of 95 °C. The physical blowing agent is CO_2 (99% purity). After melt blending, PS samples

were compression-molded with a Carver Press into disks of 4 mm diameter and 0.4 mm thickness.

3.2.2 Experimental Procedure

This study was conducted using a modified version of the batch foaming visualization system developed by A. Wong et al. that allows the in-situ observation of the PS foaming process Wong et al. 2011). The visualization system consists of a batch foaming chamber (see Fig. 3.2), a syringe pump (ISCO 500D), and two cartridge heaters with Proportional-Integral-Derivative (PID) feedback control.

To conduct the experiment, a PS sample is loaded into the foaming chamber, which was pre-heated at temperature of 160 °C during 10 minutes. This temperature was maintained throughout the experiment. Then the CO_2 was injected into the foaming chamber and the content was adjusted by controlling pressures through the syringe pump. The high injection pressure promotes the CO_2 to diffuse into the polymer sample. In this study, the residential time for the saturation of the samples was about 60 minutes. Finally, a sudden pressure drop was induced by opening the gas exit valve.

3.2.3 Sample Characterization

Cell count characterization of the microscopy images presented in Figure 3.3 is conducted using basic computer techniques of image process analysis in Matlab. The presented method uses basic morphological operations and Watershed transforms to segment the cells as a red-green-blue (RGB) image (see Fig. 3.3.d). Morphological operations include preliminary local contrast adjustments and adaptive filtering that eliminate the noise before the extraction of the dimmer cells. This follows by binarization techniques preformed to extract the perimeter of cells and/or cell groups. The cell borders and the image background are clearly differentiated by a scale range of intensities from positive to negative. The local minima in the image approximately corresponds to the cell nuclei, while the highest intensity is identified

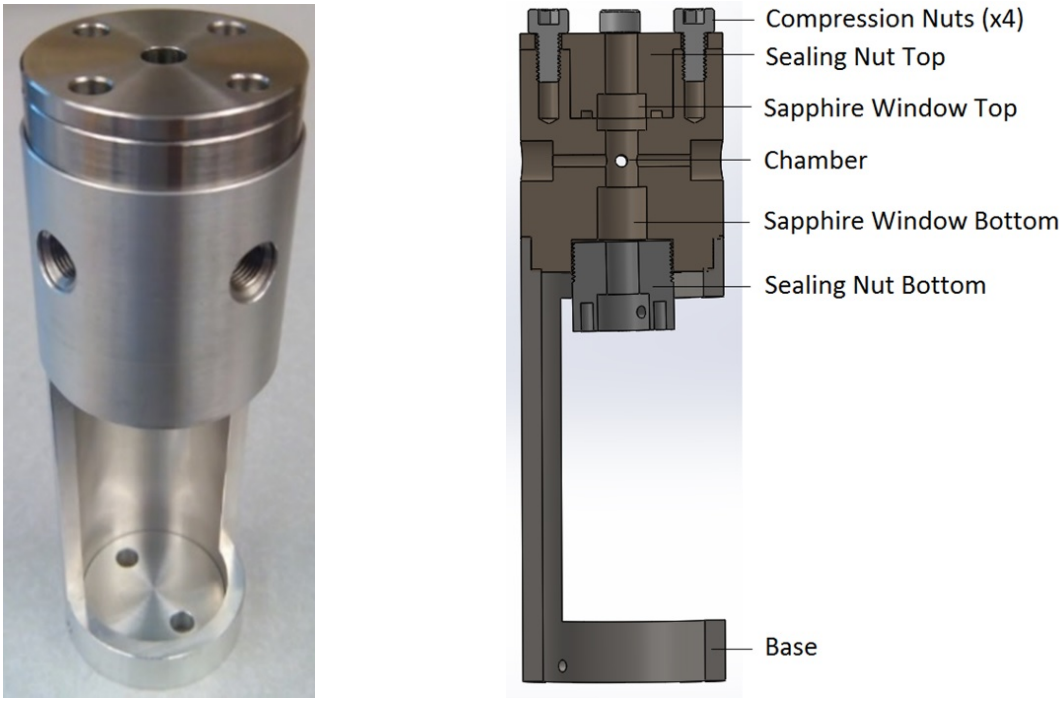

FIGURE 3.2: Figure 2. (Left) A photograph and (Right) CAD Schematic diagram of the visual observation apparatus for batch foaming.

with the cell borders. Finally, the resulting RGB image determines the approximate value of the number of cells.

3.3 Simulation Model Description

The notion of free volume is used to explain some aspects of the polymeric behavior and our own model definition of the foaming process. The proposed model has the advantage of having very clearly quantifiable output, as it is measured against a cross-section of a two-dimensional hard core lattice. It quantifies the particular amount of free space that would be occupied by the lattice (either polymer or gas) in a solid-like manner.

The increase of free space is associated with the increase in the amount of bubbles or with the increase in the bubble size. In simulation domains, the expansion associated with the increase in the free space, occurs when the number of nearest

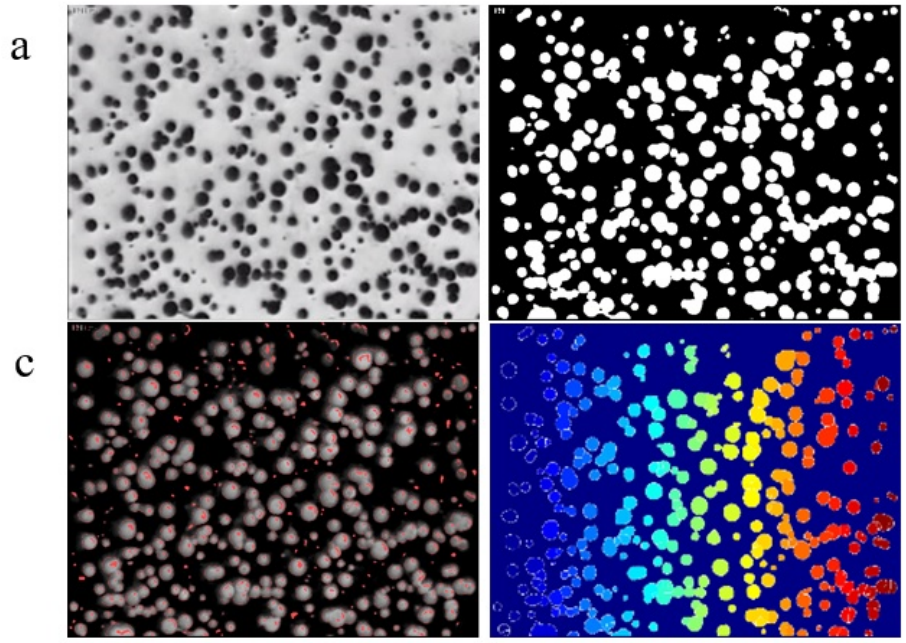

FIGURE 3.3: Image process analysis for in-situ cell counting: a. Original microscopy image; b. Binarization technique; c. Extraction of cell perimeters and cell nuclei; d. RGB image and final cell count (320 cells).

lattice neighbors increases or the distance to nearest neighbors decreases. Therefore, the model prediction reflects the maximum amount of the potentially (thus 'free') space available in the system due to the interaction between bubbles.

Based on this general conception of free volume, a simple pattern formation has been used to recreate the interaction between bubbles, simulating the different phases of the foaming process. Initially, a lattice of 106 sites (1,000 x 1,000 sites) is randomly populated with several small seeds that nucleate at a constant rate (homogeneous nucleation). The initial probability of these sites to nucleate and to become bubbles is p. Bubbles can also nucleate as a result of defects of the polymer matrix in the case of heterogeneous nucleation. From the simulation point of view, these defects are considered as nucleated bubbles in the cell that nucleate as a result of the initial seeds. Once formed the bubbles are in a metastable phase and grow at a constant rate as there is enough available free volume for expansion.

At each time step, all bubbles and nearest neighboring sites are investigated once

as to the possibility p of growing in size. The investigation sequence is randomly ordered. Each bubble is allowed to peripherally grow by one cell (increase the size to one cell in any direction) assuming that there is no overlapping with other bubbles. As soon as two or more bubbles touch each other, the growth of all of the adjoined bubbles stop. The touching bubbles can be considered as belonging to the same stable cell, a cell that no longer grows over time unless other evolving cells happen to touch it.

The system continues to evolve until no other cell can grow in time, so that all of them have at least one adjoining cell. The snapshots of typical evolutions of the system can be found in Figs. 3.5 and 3.6 (Upper raw).

3.4 Results

Figure 3.4 shows a series of micrographs obtained by visual observation experiments of PS foaming. The black dots are bubbles. After CO_2 pressure was released, numerous bubbles were nucleated and grown in the PS sample. These pictures suggest that the nucleation and bubble growth occurred simultaneously. The nucleation rate, however, seemingly slows down in speed, while the bubble growth continues until coalescence starts. As it was expected, the effect of coalescence and interaction between bubbles are visible at a very early stage of the foaming process.

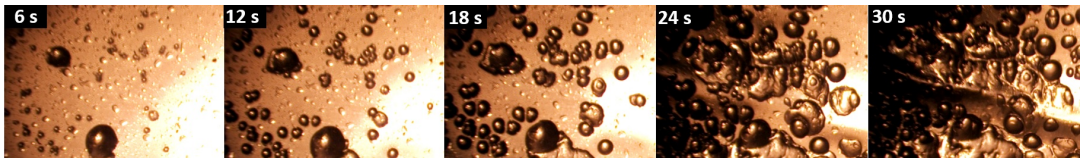

FIGURE 3.4: Visual observation of CO_2 bubbles nucleation and growth in PS.

Direct measurements of the simulated number of bubbles found in the literature further confirmed the dynamic changes in the foam structure observed by the experimental results (Taki, Hayashizaki, and Fukada 2014). The profile of the bubble surface density presented in Fig. 3.7 consists of four characteristic stages. Initially,

a slow introduction period is required to establish steady-state nucleation conditions in stage I. According to K. C. Russell (Russell 1980), the probability of bubble nucleation in this stage is proportional to exp(-W*/KT), where W* is the minimum work required to make the system unstable with respect to transformation, and kT is the product of Boltzmann's constant and the absolute temperature. This is followed by a steady state nucleation (stage II), where the number of bubbles increases linearly with respect to time. During stage III the bubble nucleation decreases significantly due to supersaturation and secondary nucleation effects. Immediately after the secondary nucleation, early stages of coalescence and gas redissolution promote a rapid decline in the number of bubbles (stage IV). As a result, the number of nucleated bubbles that are generated and survive through stages II and III decreases in stage IV at a progressively slower rate.

The trend of the decline in bubble density after nucleation is notably similar for both resins; however, resins with higher melt viscosity of the polymer matrix effectively restricted the mechanism of bubble coalescence. This behavior indicates that higher melt viscosity/elasticity resulted in a lower rate of bubble density reduction.

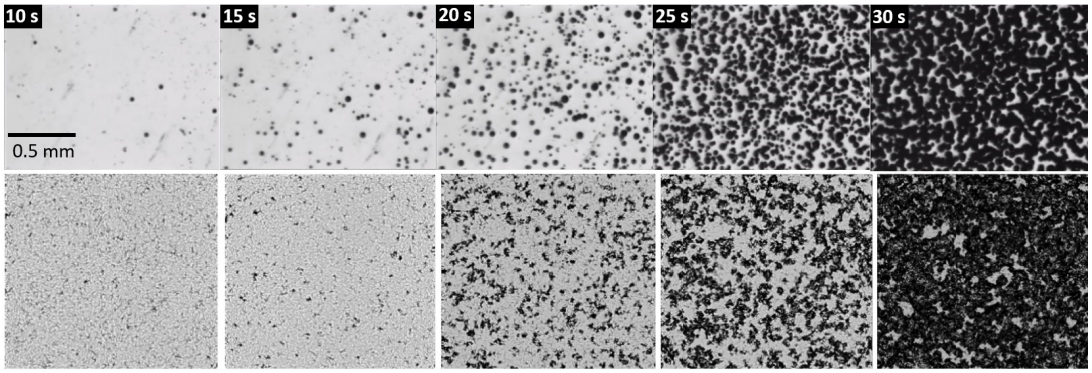

FIGURE 3.5: (Upper Raw) Series of micrographs of batch foaming of High Viscosity (HV) Polystyrene (Taki, Hayashizaki, and Fukada 2014). (Lower Raw) UVM Simulation results.

Simulated results by the bubble nucleation, growth, and collapse model were compared with the experimental data observed in the literature (Taki, Hayashizaki, and Fukada 2014). Figures 3.5 and 3.6 show good agreement between the experimental and simulation series of micrographs obtained at different stages of the foam

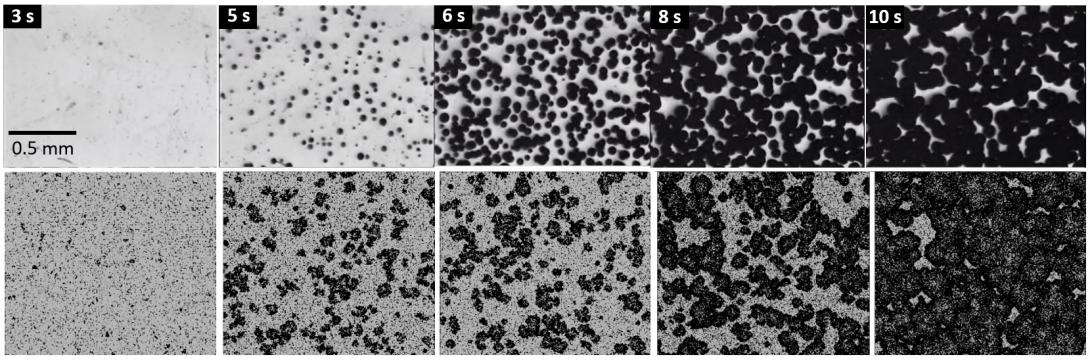

FIGURE 3.6: (Upper Raw) Series of micrographs of batch foaming of Low Viscosity (LV) Polystyrene (Taki, Hayashizaki, and Fukada 2014). (Lower Raw) UVM Simulation results.

development. In addition, a Gaussian distribution was applied as a fitting curve with 95% confidence bounds to the experimental results of the number of bubbles at the two different viscosities (Fig. 3.7).

Generally, the polystyrene samples with high viscosity resulted in lower average bubble diameters during all stages of the foaming process (see Fig. 3.9). This can be explained by the remaining gas around each bubble in the polymer matrix. Higher viscosity yields to a higher bubble density at the early stage of growth. With the larger number of formed bubbles, the amount of gas consumed for creating the bubbles becomes larger and hence, the concentration of remaining gas in the polymer matrix decreases. Consequently, the rate of mass transfer for dissolved gas from the matrix polymer to bubbles decreases, which leads to the lower bubble diameter and lower rate of bubble growth.

Figure 3.8 shows the ranked cell size distribution (CSD) at the final stage of the foam development. Small cells are more frequent than large cells. The logarithm of frequency declines linearly with the logarithm of size. We observe that to a first approximation, the CSD plotted in a log-log scale is consistent with a simple power law form. This relation was observed after cell stabilization with the final foam structure of both simulation and experimental results. From the simulation point of view, and as many other processes in nature, recursive repetition of simple multiplicative transformations result from initial random conditions. In this case, average

diameters of the multiplicative transformation determines the slopes of the power law lines. In the case of the experiments, we must also account for the fact that bubbles cannot grow indefinitely. The upper bound on growth causes the cell size distribution in Fig. 3.8.b to reduce into a narrower frequency distribution and the slope to drop below the power law line obtained for the simulation case.

3.5 Conclusions

A high-pressure chamber with glass windows made the visual observation of foaming possible. Using the chamber, batch foaming experiments were conducted by pressure release, and the simultaneous nucleation, bubble growth rate, and collapse were observed at very early stages of the foaming process. Series of micrographs of PS samples with different viscosities were analyzed using process image analysis techniques. The simulation model and experimental results showed good agreement. This provided a mean to directly analyze the foaming process via the number of bubbles, the bubble diameter, and the cell size distribution. In the first stage, an introduction period establishes the required time for the steady state nucleation conditions. Then the number of bubbles increases linearly with time, due to the spontaneous appearance of more bubbles. Immediately after the secondary nucleation, coalescence effects result in fewer but larger bubbles. An underlying result of power law distributions was found in the cell size distribution of the final foam structures of experimental and simulation data.

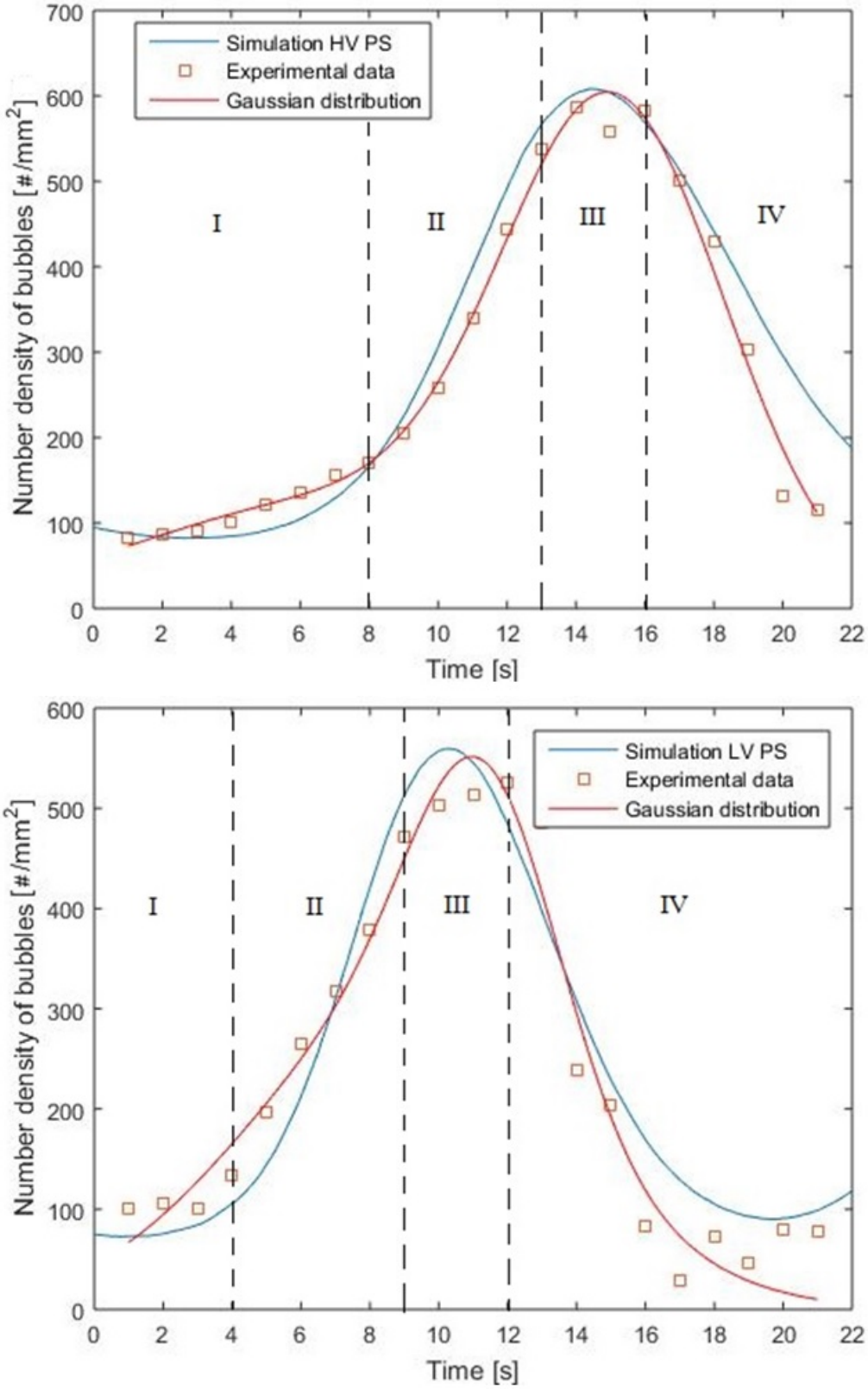

FIGURE 3.7: (Upper) High and (Lower) Low Viscosity PS. Fitting the calculated number of bubbles to the experimental data using simulation results and the two-term Gaussian model with 95% confidence bounds. The four regions are, I: Introduction period; II: Steady state nucleation; III: Decreasing nucleation rate due to decreasing supersaturation; and IV: Ostwald ripening, or bubble coarsening.

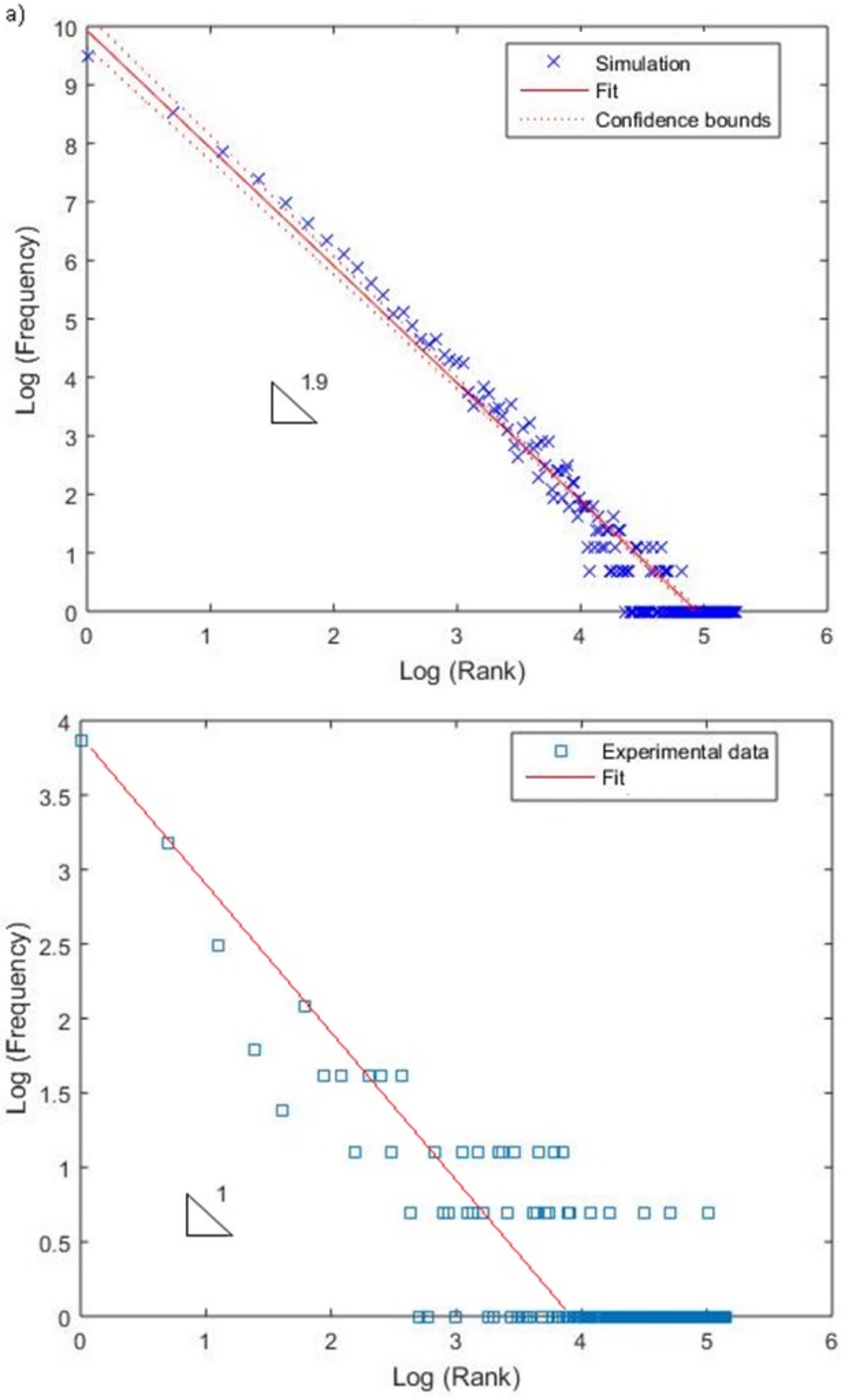

FIGURE 3.8: Comparison between the experimental and numerical simulation results of cell size distribution of bubbles in log-log scale. The group sizes in the plots are rank according to decreasing size (hence Zipf-like). A power law distribution was observed for both experiments and simulation of the resulting HV and LV polystyrene final foam structure.

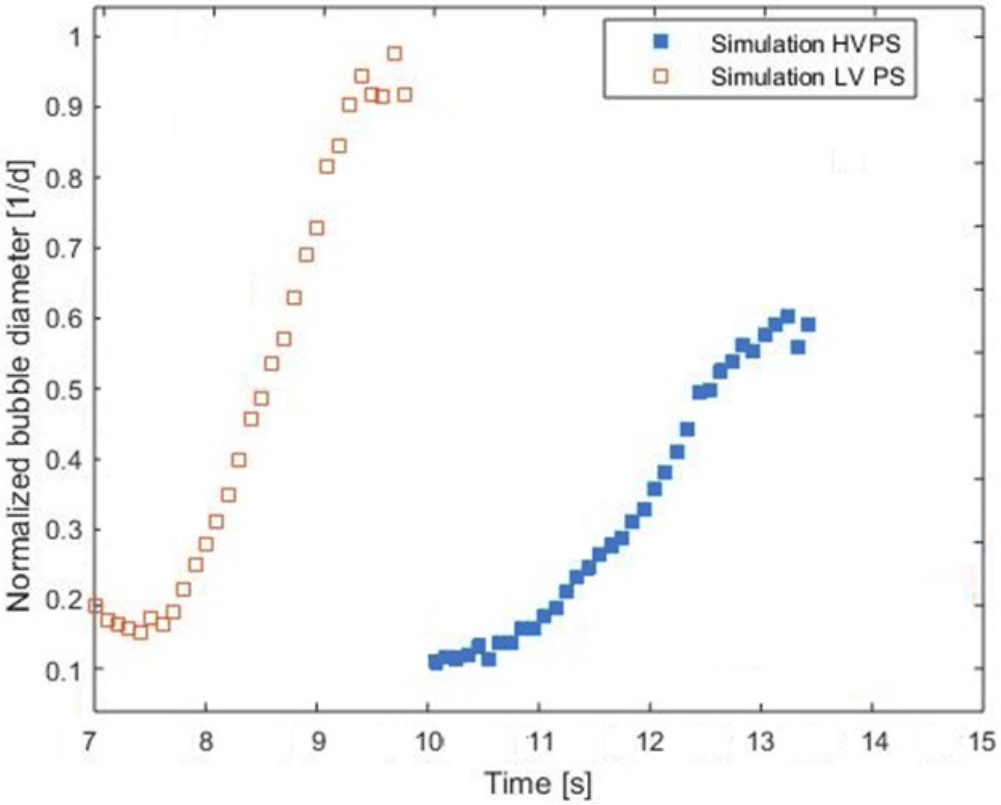

FIGURE 3.9: Temporal change in diameter of selected foaming bubble.

Chapter 4

In-Situ Visualization of Crystal Nucleation and Growth Behaviors of Polymers under High Pressure CO_2

4.1 Introduction

Global efforts are being made to create green polymer from renewable resources which are biodegradable and environmental-friendly. Over the last decades, polylactic-acid (PLA) has been established as one of the most promising sustainable alternatives to fossil fuel-derived polymers due to its low cost and high performance. However, a few drawbacks such as slow crystallization rate, low glass transition and service temperatures (i.e., low melt strength) limit PLA's applications.

In foam processes, maintaining the biodegradability and improving the PLA's mechanical properties is possible by increasing crystallinity. It is well known that crystallinity can improve stiffness, melt strength, chemical resistance, and heat distortion temperature (Harris and Lee 2008, Zhang et al. 2017, Xu et al. 2012). Furthermore, crystallinity can promote cell nucleation via the heterogeneous nucleation mechanism. The cell nucleation rate at the interface between spherulites and

the amorphous section increases by excluding CO_2 that accumulates around the spherulite interface. Therefore, CO_2 plasticization effect in the amorphous phase leads to an increase in the bubble nucleation (Taki, Kitano, and Ohshima 2011).

However, the polymer's final crystallinity does not necessarily increase consistently with the increased content of dissolved CO_2 (Takada, Hasegawa, and Ohshima 2004, Nofar et al. 2013, Oda and Saito 2004). This is because at various CO_2 pressures, different kinetics (i.e., crystal nucleation and growth) dominate the PLA's crystallization.

Additionally, in subsequent processes such as extrusion, injection molding, blow molding, fiber spinning, and film blowing, the existence of shear and/or extensional flow during processing can significantly promote PLA's crystallization kinetics as well as nucleation due to the CO_2 plasticization (Wong 2012, Janeschitz-Kriegl et al. 1983).

In this study, we contribute towards a better understanding of the polymer's crystallization kinetics by direct observation of crystal nucleation/growth process under static using a high-pressure differential scanning calorimeter (HP-DSC) and under a steady shear flow using a custom-made high-pressure sliding plate chamber (HP-SPC).

4.2 Experimental

4.2.1 Materials and Sample Preparation

Semi-crystalline IngeoTM 8052D linear PLA (4.5 mol% D-content) was supplied by NatureWorks LLC. Its reported D-isomer content is 4.3 mol%. The density and melt flow index of this PLA are 1.24 g/cm^3 and 14 g/10min (210 °C/2.16 kg), respectively.

To decrease the moisture level, the PLA pellets were dried in a vacuum oven at 65 °C overnight before being used. The material was used as received without

any further purification. Carbon dioxide (CO_2), (99% pure) supplied by Airgas, was used as a saturation gas for the HP-DSC and in-situ visualization measurements.

For visualization purposes, PLA pellets were melt-pressed at 200 °C to a thickness of 60 μm and left for 5 minutes at that temperature. They were cooled subsequently to room temperature with a cold-water circulation around the press at a rate of approximately 30 °C/min at atmospheric pressure to obtain fully amorphous samples.

4.2.2 High-Pressure Differential Scanning Calorimeter (HP-DSC)

A high-pressure differential scanning calorimeter (NETZSCH DSC 204 HP Phoenix, Germany) was used for the crystallization kinetics study of PLA. The HP-DSC was calibrated with In, Sn, Bi, and Zn under ambient and high CO_2 pressures. The following procedure was applied for every DSC measurements. After a sample between 5-10 mg was loaded, the system was evacuated using a vacuum pump for 5 min. The sample was scanned at the selected CO_2 pressures during the whole process. Then, sample was heated to a molten state at a rate of 10 °C/min and equilibrated at 200 °C for 10 min to dissolve the CO_2 into it and to remove all previous stress and thermal histories.

In order to investigate the non-isothermal crystallization behavior of PLA, tests were conducted cooling from the equilibrium temperature to room temperature at rate of -5 °C /min. The melting (T_m) and crystallization temperatures (T_c) of PLA were recorded during the heating and cooling process under various CO_2 pressures (0.1, 1.5, 3.0, 4.5, and 6 MPa). Same heating-cooling cycle is repeated twice, and T_m and T_c of the polymer are recorded from the second heating and cooling scan, respectively. Experiments were conducted at least three times to examine repeatability of the results.

4.2.3 High-Pressure Sliding Plate Chamber (HP-SPC)

To carry out in-situ observation of the plastic crystallization under controllable shear strain and shear strain rate conditions, a novel custom-made HP-SPC was designed. The HP-SPC was constructed of stainless steel with an inner volume of 356.96 mL, as shown in Figure 4.1. The HP-SPC includes a sliding plate assembly controlled by a linear actuator (Oriental Motors EZA6) consisting on a stepper motor with accurate feedback control. The stepper motor, together with a high accuracy linear variable displacement transducer (Omega LD620-50) allow to convert and measure rotary motion to linear displacement. The motion of the motor was programmed and executed using the HyperTerminal software.

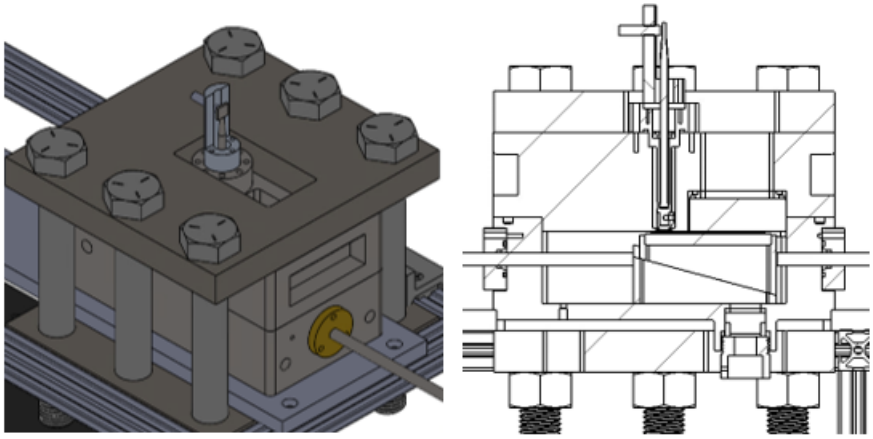

FIGURE 4.1: Isometric and cross-section view of the High-Pressure Sliding Plate Chamber (HP-SPC).

In order to allow visibility of the sample at any point during the experiment, two sapphire glass windows were mounted on the top cover of the chamber, compressing a rectangular-shaped PLA sample of size 30 mm x 50 mm. After the system was evacuated for 1 h to degas the film specimen, high-pressure CO_2 was injected into the chamber with a syringe pump (Teledyne 500D).

Isothermal tests were conducted heating the PLA sample at a constant rate of 10 °C/min, equilibrating at 200 °C for 10 min, and quenching the sample from the melt state to the selected isothermal temperature (T_{iso}) at a rate of -5 °C/min. As it is well known from experiments on quiescent melts, the speed of the growth of spherulites

is temperature dependent (Janeschitz-Kriegl et al. 1983). Therefore, in order to isolate the CO_2 pressure effect, isothermal temperatures were selected 20 °C above T_c at the corresponding CO_2 pressure. Temperature was monitored and controlled by two resistive thermal detector (RTD) (Omega PT110), four electric cartridge heaters, and a single temperature controller (Omega CN7523).

Right after reaching the isothermal temperature, a small-magnitude shear strain was applied to the PLA sample along the longest dimension during a few seconds. Before shear strain was applied to the film specimen, the bottom plate was maintained in a low position during gas saturation. After this, the bottom plate rises up to a higher level in order for the free surface of the sample to make contact with the upper shearing surface.

After the desired strain and the desired strain rate have been achieved, the motor stops, and the development of PLA spherulites during the isothermal annealing at the corresponding T_c was observed using a digital high-fidelity camera (Sony Alpha-99). The camera is equipped above the HP-SPC and couple to objective lens with (x10) magnification (Mitutoyo M Plan APO). For a clear image of the structure, halogen light was irradiated onto the specimen from the lower part of the HP-SPC passing by two high contrast linear polarizers (Edmund 85919). This microscopic system provided real-time observation onto the specimen collecting images from a remote control every 30 seconds until crystallization is completed.

4.2.4 Sample Characterization

The crystal morphology of the microscopy images presented in Figure 4.2 is conducted using basic computer techniques of image process analysis in Matlab. The presented method uses basic morphological operations and Watershed transforms to segment the crystal structure as a red-green-blue (RGB) image (see Fig. 4.2.d).

Morphological operations include preliminary local contrast adjustments and adaptive filtering that eliminate the noise before the extraction of the dimmer cells.

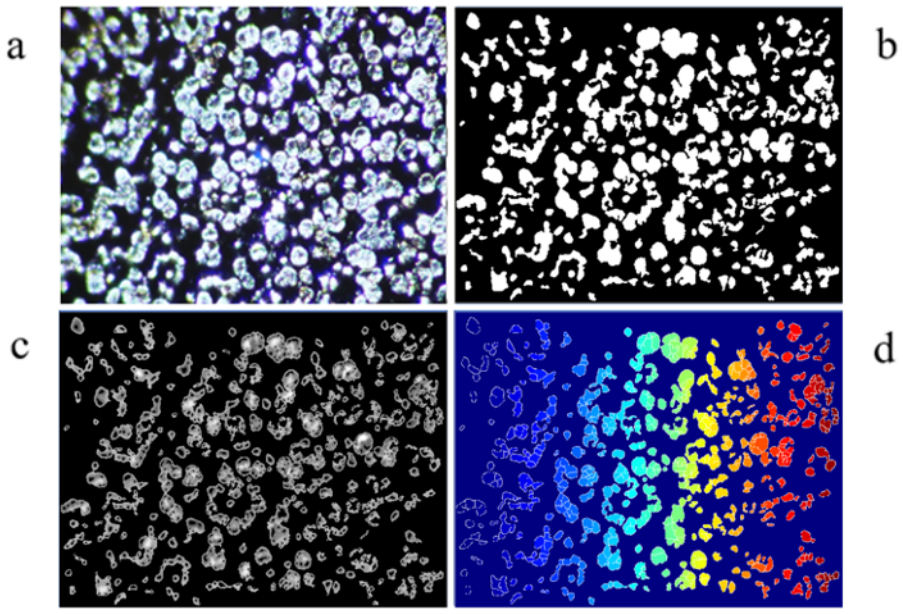

FIGURE 4.2: Image process analysis for in-situ crystallization growth: a. Original microscopy image; b. Binarization technique; c. Extraction of crystal perimeters and crystal nuclei; d. RGB image and average crystal diameter (50 μm).

This follows by binarization techniques preformed to extract the perimeter of crystals and/or crystal groups. The crystal borders and the image background are clearly differentiated by a scale range of intensities from positive to negative. The local minima in the image approximately corresponds to the crystal nuclei, while the highest intensity is identified with the crystal borders. Finally, the resulting RGB image determines the approximate value of the number of crystals.

4.3 Results and Discussion

4.3.1 Non-Isothermal Crystallization Study

Previous investigations showed that T_m and T_c decrease roughly linearly with increasing pressure, and the same tendency was obtained in our study at CO_2 pressures in the range (0.1-6 MPa) (Takada, Hasegawa, and Ohshima 2004, Huang et al. 2016, Ding 2016). The CO_2 pressure dependence of T_c and T_m of PLA using a HP-DSC was found to induce a drop in T_c and T_m at a rate of approximately -4.54

°C/MPa and -2.01 °C/MPa respectively, which are in fairly good agreement with literature results (see Figures 4.3 and 4.4).

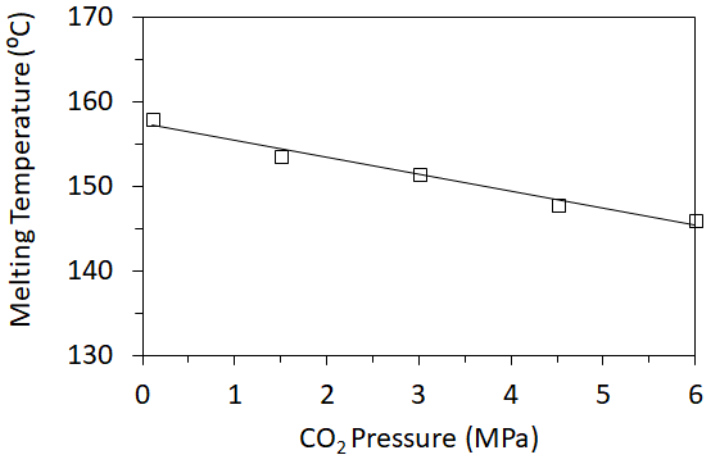

FIGURE 4.3: Depression in T_m as a function of CO_2 pressure.

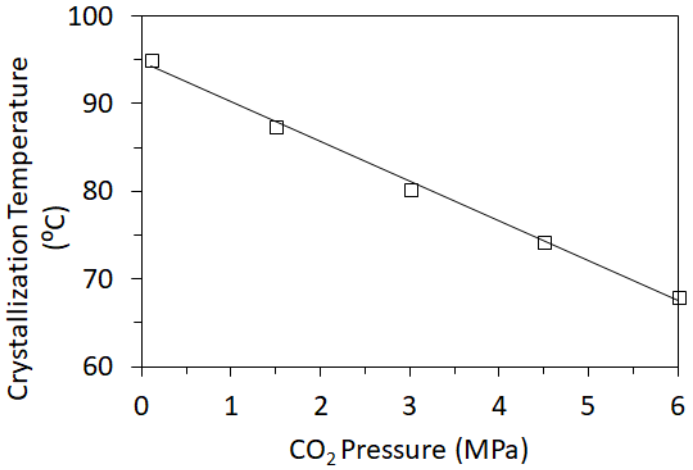

FIGURE 4.4: Depression in T_c as a function of CO_2 pressure.

The drop in T_m caused by the dissolved CO_2 may indicate that the melting temperature of final products could be suppressed during the foam processing of PLA/CO_2 mixtures due to the formation of less perfect spherulites. This will be subject of further discussion in the next section.

4.3.2 Isothermal Crystallization Study

Crystal visualization under static conditions

Crystal nucleation density and crystal growth rate phenomena of PLA under various CO_2 pressures were investigated using a custom-made HP-SPC. Polarized optical micrographs of the PLA spherulites obtained by crystallization under 0.1, 3, and 6 MPa CO_2 pressure are shown in Figure 4.5 as an example.

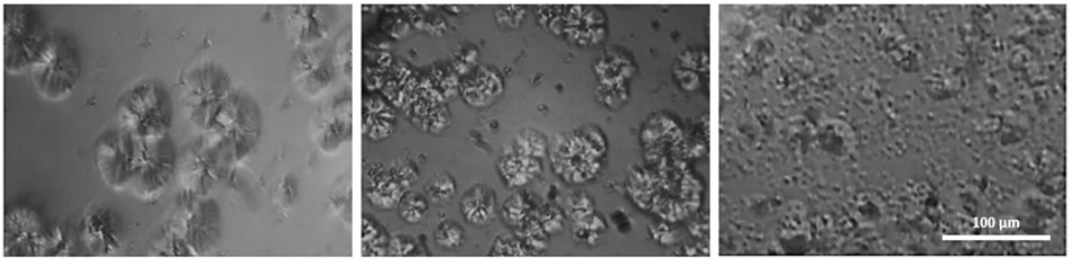

FIGURE 4.5: (From left to right) Polarized micrographs of PLA spherulites under atmospheric, 3 MPa, and 6 MPa CO_2 pressure.

Fibrils of several micrometers wide can be seen in the spherulites, as they radiate from the center. The fibrils are straight and long in the PLA spherulites obtained under atmospheric CO_2 pressure. A similar structure has been obtained by crystallization of PLA at higher CO_2 pressure (3 MPa). However, the fibrils are distorted and branched in the spherulites obtained under CO_2 above 3 MPa. Results obtained with polypropylene are similar to those described above for PLA (Oda and Saito 2004).

The crystalline domains are considered to be impenetrable for CO_2 molecules because of the compact chain packing. This produces CO_2 expel from the advancing crystalline-amorphous phase interface during the crystallization (Li et al. 2017). Indeed, according to Keith and Padden Jr the interfibrillar amorphous region becomes larger as the degree of exclusion of CO_2 increases (Keith and Padden Jr 1964, Keith and Padden Jr 1963). Presumably, this is due to higher degree of exclusion of CO_2 from the spherulitic growth front, which results from the higher CO_2 concentration dissolved in the polymer (Okada, Saito, and Inoue 1994).

Additionally, the radius of the spherulites, r over time was obtained using image process analysis techniques described in section Sample Characterization. The time variation of r at various CO_2 pressures was proved to increase linearly with time t, meaning that the radial growth rate is constant throughout the PLA crystallization. This is generally accepted except when growing particles are near impingement (Sherwood 1977).

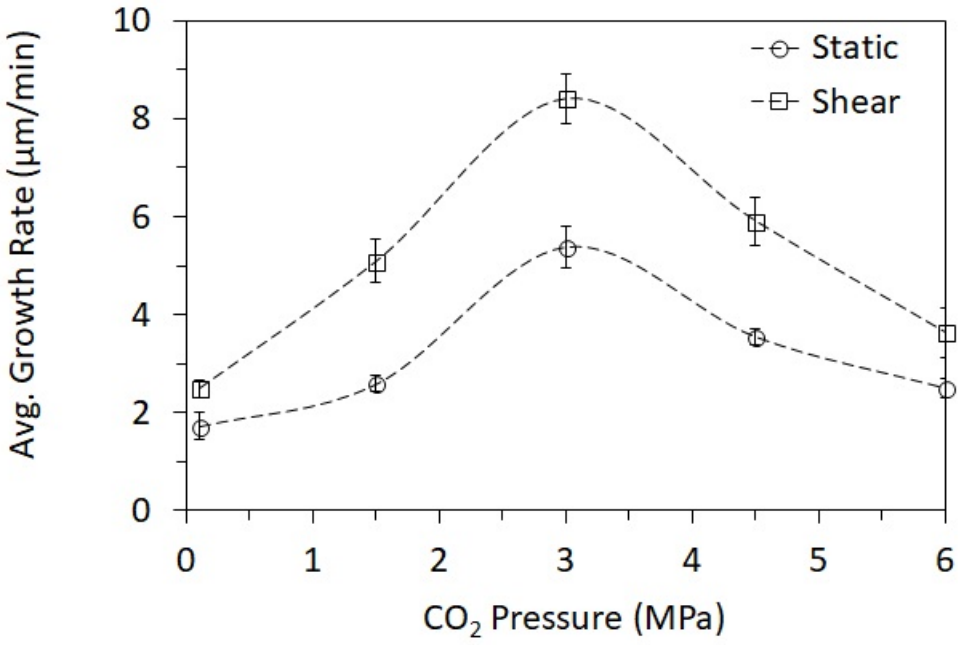

FIGURE 4.6: Depression in T_m as a function of CO_2 pressure.

As shown in Figures 4.6 and 4.7, the crystal growth rate and nucleation density increase with the dissolved CO_2, achieving a maximum value at around 3 MPa. At low CO_2 pressures (i.e., 1.5 MPa) larger and more perfect crystals formed. Low CO_2 pressure enhances PLA's molecular mobility and facilitates the crystal growth with more perfect structure and slower crystal growth rate (see Fig. 4.8a). At the peak around 3 MPa, we observe the highest nucleation density and smaller crystals due to higher CO_2 plasticization effect (see Fig. 4.8b).

Therefore, as CO_2's plasticization effect increases, PLA molecule's entanglement also increases. As a result, the crystal growth increases producing spherulites with

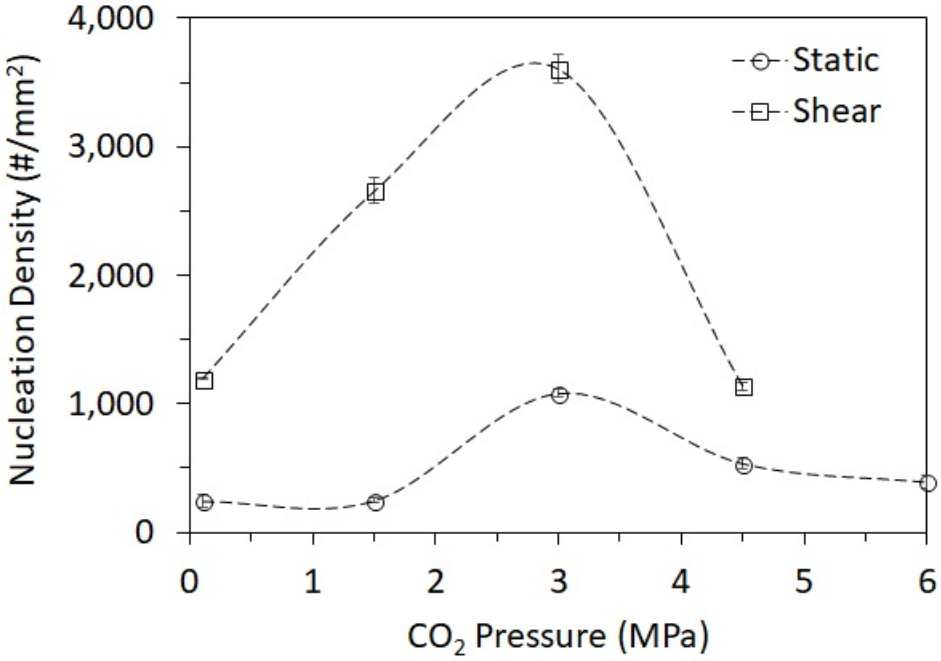

FIGURE 4.7: Depression in T_c as a function of CO_2 pressure.

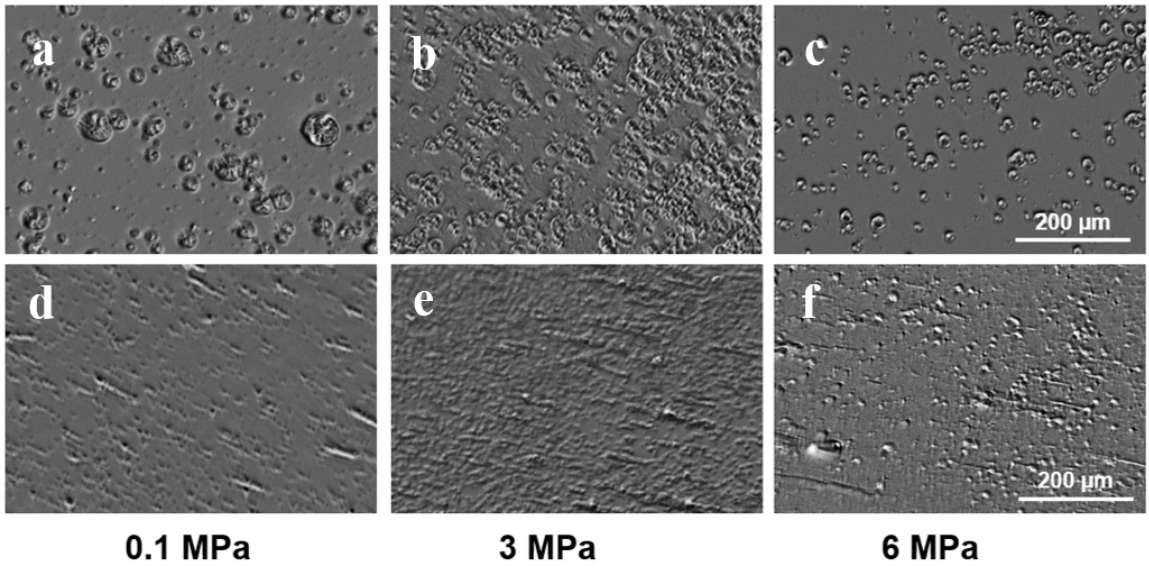

FIGURE 4.8: POM micrographs of PLA at various CO2 pressures during isothermal melt crystallization under static (upper raw) and shear conditions (γ = 25, $\dot{\gamma}$= 30 s^{-1})) (lower raw).

less perfection (i.e., higher crystal growth rate). Such accelerated crystallization behavior is similar to that reported in refs (Takada, Hasegawa, and Ohshima 2004,

Oda and Saito 2004). Note that as it was mentioned earlier, the Tm of PLA depressed with CO_2 pressure, which also seems to support our observation of smaller and more imperfect crystal formation (see Non-Isothermal Crystallization Study).

However, at increased CO_2 content beyond 3 MPa, the crystal growth rate was suppressed most likely through CO_2's dominant hydraulic pressure effect. The nucleation density decreases, reducing crystal growth rate and thereby the PLA's final crystallinity. In other words, two competitive effects control the crystal growth in the crystallization of the PLA-CO_2 system: the hydraulic pressure decreasing the molecular mobility of the polymer and the plasticization effect increasing the crystal-to-crystal network through PLA molecule's entanglement.

Crystal visualization under shear conditions

In order to separate the crystallization induced by shear from crystallization without shear effect, isothermal temperatures were selected 10 °C above T_c (see Figure 4.4) at which crystallization occurs even without shear.

Isothermal DSC measurements and visualization tests with HP-SPC under static conditions were performed to conform this temperature at various pressures. Figure 4.8 shows typical snapshots of the observation under the HP-SPC. Upper raw images were observed under static conditions and lower raw images were observed under steady shear flow (γ = 25, $\dot{\gamma}$= 30 s^{-1}). Without shear, complete crystallization was observed within approx. 30 minutes at the set up T_{iso} and atmospheric conditions; this is consistent with our results of DSC. Under shear conditions, soon after reaching T_{iso}, distorted (slightly anisotropic) spherulites are suddenly induced following by high nucleation density and rapid crystal growth rate (see Figure 4.8 d-f).

Figure 4.8 d-f shows a typical row-nucleated crystal structure in the direction of the flow direction during shear. This implies that highly deformed regions were generated under shear after certain amount of time. We suppose that the spherulites develop more easily in the highly oriented bands rather than in the matrix region as response to the local increase in stress of the melt and the lower (heterogeneous)

energy barrier. Other authors pointed out that the enhanced crystallization under shear cannot be attributed only to effects caused by heterogeneities, rather it is the combination of the molecular extension arising from chain entanglements (Sherwood 1977).

A main result from our shear experiments is that the crystal growth rate of spherulite radius, even at the lowers shear rates applied, is considerably faster at the same temperature than under static conditions. In addition, crystal nucleation density and crystal growth can be controlled by CO_2 pressure and shear stress/strain.

4.4 Conclusions

The effects of shear and CO_2 pressure on the crystallization kinetics of polylactic acid (PLA) were investigated. Shear strain/stress improved the PLA's crystallization kinetics by higher nucleation density and faster crystal growth rate. Maximum nucleation density and crystal growth rate were achieved at CO_2 pressures around 3 MPa by facilitating more perfect crystals through the CO_2's plasticization effect. Therefore, we conclude that the PLA's crystallization behaviors can be engineered by CO_2 pressures and shear strain/stress.

Chapter 5

Batch Foaming Study

5.1 Introduction

The industry faces ever increasing demands of creating more efficient and optimum products to meet the sustainability goals. Creating lightweight structures without compensating other critical properties is one of the main focus areas. In plastics industry, plastic foaming using physical and/or chemical blowing agents is a well-established method to manufacture lightweight structures for various applications such as packaging, insulation or construction.

Additionally, the mechanical properties and applications of polymeric foams are to a large extent determined by their cell morphologies, that is, the cell size, cell density and cell shape (closed/open). For instance, macro-cell polymeric foams can be used in packaging, thermal insulation, cushioning and construction of low cost housing. Whereas, microcellular polymeric foams with cell sizes smaller than 10 μm and cell densities larger than 10^9 cells/cm^3 can reduce the mass and thereby the cost of products considerably while only slightly deteriorating part properties. Hence they could be employed in more demanding fields where both light-weight and high mechanical properties of products are required, such as the aerospace and the automotive industries.

In this study, we proposed to understand the picture of newly synthesized polypropylene (PP) resins' foaming behaviors with respect to various process parameters and

to compare the thermal conductivity performance against prevailing foam grade resins on the market.

5.2 Experimental Procedure and Apparatus

5.2.1 Materials and Sample Preparation

The plastics used were two linear PP (PP2, w and w/o NA) and three types of branched PP (PP5241E1 and PP1; MFX6, Waymax; WB140, Borealis; 1025MA, Braskem) are listed in Table 5.1. The melting temperature (T_m) and crystallization temperature (T_c) of all polymers were measured using HP-DSC analysis (see Figures 5.24 and 5.25). The polymer resins were compression molded to disk shape samples 0.3 mm in thickness with a hot press at 200 °C after breaking the extrudates into smaller pieces. Upon pressure release, the molded films were immediately quenched with a large reservoir of water at 13 °C. The blowing agent used was CO_2 (99.8% pure, Airgas).

Category	**Distributor**	**Chemical Characterization**	**Material**
High-Melt Strength Polypropylene (HMS PP)	Under protected agreement	Homopolymer	PP5341E1
			PP1
			PP2
			PP2 w/o NA
Control	Waymax		MFX6
	Borealis		WB140
	Braskem		1025MA
Cell Nucleating Agent (NA)	Bergen International	Chemical Blowing Agent (CBA)	XO-286
	Heritage Plastics	Talc	HT4HP
Physical Blowing Agent (BA)	Airgas	Supercritical Fluid	CO_2

TABLE 5.1: Material List

5.2.2 Foaming Chamber and Foaming Process

Foams were generated by a batch foaming process in a high temperature and pressure foaming chamber as shown in Fig. 5.1. The temperature (T) is measured in the center of the chamber cavity and is controlled based on its reading. The pressure (P) is measured on top of the chamber cavity, and the values can be recorded by a PC. The maximum operating T and P are 250 °C and 4,500 psi, respectively. There are three different ports connected to a valve to give different pressure drop rate (-dP/dt) at each pressure. Each port was carefully designed and calibrated to give around 2X differences in -dP/dt. For example, at 1,500 psi, opening Port A gives 4, Port B gives 9, and Port C gives 18 MPa/s. It was found that the -dP/dt is a very weak function of T but a strong function of P. Table 5.2 shows the -dP/dt at given T and P for opening each port. Table 5.3 shows how characterized data will be reported in a table format. The pressure drop rates which cannot be achievable appear as 'X' sections.

T (°C)	Port	P (psi)		
		1500	3000	4500
140	A	4	9	18
	B	9	18	35
	C	18	35	60

TABLE 5.2: Pressure drop rates, dP/dt (MPa/s) at various P at 140°C. Deviations are within 10% and there is no significant difference at other temperatures.

T (°C)	dP/dt (MPa/s)	P (psi)		
		1500	3000	4500
140	4		X	X
	9			X
	18			
	35	X		
	60	X	X	

TABLE 5.3: Reporting table

One to four disk samples were placed into the chamber at a test temperature, and then the chamber was closed. The chamber was purged with CO_2 for 30s prior

FIGURE 5.1: High temperature and pressure foaming chamber. (Left) Closed setup. (Right) Open setup. Top has a thermocouple.

to pressurization. Then the chamber was pressurized with CO_2 up to the desired test pressure. Meanwhile, we expect CO_2 to diffuse into the sample.

After one hour of sorption time at given T and P, a valve was quickly opened to induce foaming. Once the top of the chamber was opened, the foam was cooled down in cold water. After removing residual water, the foam samples were stored in a Ziploc bag.

5.2.3 Foaming Conditions and Design of Experiments (DOE)

To reveal model relations between an input, or effect, and an output, or response, the best approach is to deliberately change the former and see whether the latter changes, too. Actively manipulating factors according to a pre-specified design is the best way to gain useful, new understanding.

However, whenever there is more than one factor, a design that changes just one factor at a time is inefficient. To properly uncover how factors jointly affect the response, we used design of experiments (DOE) with JMP for this study.

Our goal is to create an experimental design that takes into account pressure (P), pressure drop rate (dP/dt), and additive type and amount. For this purpose we construct a design customized to our problem, so we don't have to force our problem to fit a prescribed textbook design such as classical or split-plot designs. Proposed DOE can be found in Appendix B.

5.3 Characterization Methods

Seven different properties were determined for both unfoamed and foamed materials. An average value was taken over three time measurements. Table 5.4 summarizes necessary apparatus and base protocols. Detailed principles and procedures can be found in the relevant protocols, and only essential features and key equations are described in this section.

Property	**Apparatus**	**Protocol**
Foam density / Specific volume	Balance with density kit	ASTM D792
Cell density	EVOS AMG Microscope, Scanning Electron Microscope (SEM)	[Refs]
Open/closed cell contents	StereoPycnometer	ASTM D6226
Flammability	Stand, torch, timer	ASTM D3801
Crystallinity	High Pressure Differential Scanning Calorimeter (HP-DSC)	ASTM E794

TABLE 5.4: Characterized properties, apparatus, and protocols.

5.3.1 Foam (bulk) density and specific volume

The test method is based on ASTM D 792 (Standard Test Method for Density and Specific Gravity [Relative Density] of Plastics by Displacement). Density (ρ) and the specific volume (ν) of a solid sample can be easily obtained by:

$$\rho = W/V \tag{5.1}$$

$$\nu = 1/\rho \tag{5.2}$$

where W is the weight and V is the volume of the sample. However, when the shape of the specimen is irregular, it is difficult to calculate its volume. The volume can be determined by Archimedes' principle: 'Any object, wholly or partially immersed in a stationary fluid, is buoyed up by a force equal to the weight of the fluid displaced by the object' by measuring buoyancy force upon submerging the solid into water. The weight of the displaced water is directly proportional to the volume of the displaced fluid, and thus the volume of the sample can be obtained.

First, the weight (W) is measured on top of the black dish, which is connected to the balance sensor (Fig. 5.2). After submerging the sample in the water in the beaker by pushing down using the spiral wire, which is connected to the balance sensor, another value is read (apparent immersed weight, W_B). The density of the sample can be determined by:

$$\rho = \rho_0 \frac{W}{W - W_B} \tag{5.3}$$

where ρ_0 is the density of water at the test temperature.

5.3.2 Cell density

Cell density (CD), the number of cells (bubbles) with respect to the unit volume of the unfoamed polymer, is obtained by:

$$CD\ (cells/cm^3) = \left(\frac{n}{A}\right)^{1.5} \frac{\rho_{solid}}{\rho} \tag{5.4}$$

where A is the area (cm^2) of the microscope image, n is the number of cells in the image, and ρ_{solid} and ρ are the densities of the before and after foaming, respectively.

The reason to consider the unit volume of the unfoamed polymer, not foamed polymer is to exclude the effect of bulk volume for comparison of CD among the foams with different bulk volumes.

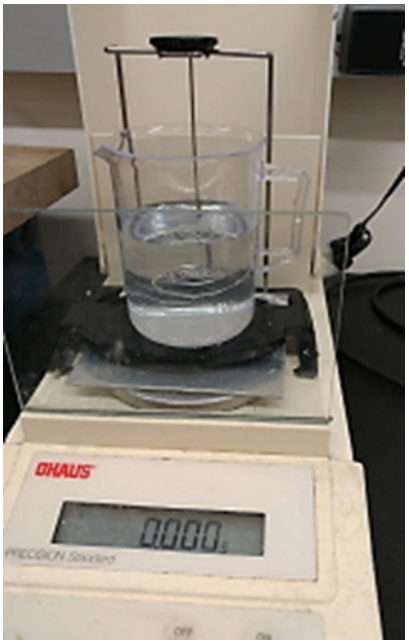

FIGURE 5.2: A microbalance with a density measurement kit. The beaker is not on the balance sensor but on a separate base.

FIGURE 5.3: (Left) Foam morphology observed by a microscope.(Right) JEOL 6060 Scanning Electron Microscope (SEM)

5.3.3 Closed cell / open cell contents

The test method is based on ASTM D 6226 (Standard Test Method for Open Cell Content of Rigid Cellular Plastics). There are two chambers in a pycnometer to allows us to measure a sample volume. A sample is cut to fit Chamber A, and its

weight (W) is measured. The sample volume (V) can be determined by:

$$V = W/\rho \tag{5.5}$$

where ρ is the foam or bulk density of the sample. The sample volume (V) consists of three components:

$$V = V_{solid} + V_{closed} + V_{open} \tag{5.6}$$

where V_{solid}, V_{closed}, and V_{open} are volume of solid walls or matrix of plastic, void volume of closed cells, and void volume of open cells, respectively.

FIGURE 5.4: SPY-6DC StereoPycnometer. The pressure values are shown for demonstration purpose only. (Left) A sample is placed in Chamber A. (Right) Chamber is closed for pressurization.

Once the sample is placed in chamber A (Fig. 5.4), after closing the top, chambers A and B are purged at 1 atm. Around 3 psig nitrogen (N_2) is applied into only chamber A, and pressure (P_1) of the chamber is measured. By opening a valve, which is between cambers A and B, pressure drops to lower pressure (P_2) due to the increases in the internal volume of the apparatus. Since the volumes of chambers A and B (V_A and V_B) are known, the sample volume excluding open channels, i.e.

(V_{solid}+V_{closed}) where N_2 cannot reach, can be determined as follows:

$$V_{solid} + V_{closed} = V_A - \frac{V_B}{\frac{P_1}{P_2} - 1} \tag{5.7}$$

Since the solid volume can be known ($V_{solid} = W/\rho_{solid}$), the closed cell volume can be easily obtained by the above equation. Since the total void volume is obtained by:

$$V_{void} = V_{closed} + V_{open} = V - V_{closed} = V - \frac{W}{\rho_{solid}} \tag{5.8}$$

the open cell volume can also be obtained. The percent volume fraction of each component can be obtained by:

$$f_{void} = 100 V_{solid}/V \tag{5.9}$$

$$f_{closed} = 100 V_{closed}/V \tag{5.10}$$

$$f_{open} = 100 V_{open}/V \tag{5.11}$$

5.3.4 Flammability

Flammability can be determined after ignition either by how fast the flame can propagate or how long (time or length) the flame can survive until it is extinguished by itself (ASTM D3801). Due to the limited size of the foam samples, only the latter method (burning time) was performed in this study.

As shown in Fig. 5.5, a sample of 1 cm (W) x 1.5 cm (L) x 0.3 cm (T) was held vertically in a fume hood. A 7 cm-long torch flame was applied to the end of the sample for 3 seconds (Fig. 5.5a), and then it was removed (Figs. 5.5b and c). The burning time while there was a flame on the sample was recorded. Some foams extinguished by itself (Fig. 5.5b) while the others never did (Fig. 5.5c). All the measurements were performed around the same time to minimize daily variations of the environment. While recording burning times, the flame on the torch was not

turned off but only put aside (Fig. 5.5c) to keep the same flame length for all tests. During the flammability tests, the flame length did not change.

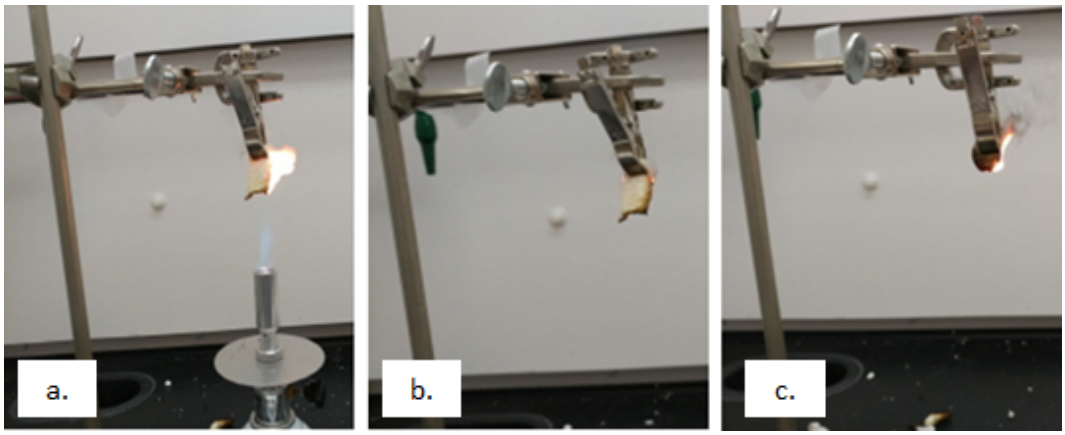

FIGURE 5.5: Flammability test. a. Ignition, b. Extinguishing by itself, and c. Burning without extinguishing flame.

5.4 Results and Discussion

5.4.1 Batch Foaming Study

Pressure Drop Rate Effect, dP/dt

The pressure drop rate is an important parameter to affect PP foaming. Much attention has been given to the influence of pressure gradient or pressure drop rate on batch or continuous processes. It was shown that a high pressure drop and a high pressure drop rate are the necessary conditions to nucleate a great number of small cells because the pressure drop provides the direct driving force for phase separation (Klempner and Sendijarevic 2004). In our study, the pressure drop rate could be affected by the opening of high-pressure ball valves with various port diameters (see Fig. 5.1).

After pressure drop, the density (ρ) was first determined. Note that the bulkiness of material is directly proportional to the specific volume (ν). Figures 5.6-5.9 show both high and low pressure drop rate data for both foamed control PP samples and studied materials. As it is shown, increased pressure drop rate tends to increase

the foam expansion up to 31 MPa. More specifically, the lowest foam density and highest cell density values are obtained with Borealis WB140 material at high pressure drop rate and 3,000 psi CO_2 pressure (0.01 ρ/cc and 10^8 cells/cc, respectively). These results fall clearly within the low-density foam range and very closed to the microcellular structure. This is not surprising because higher pressure drop rates decrease the nucleation energy for cell nucleation, according to classical nucleation theory.

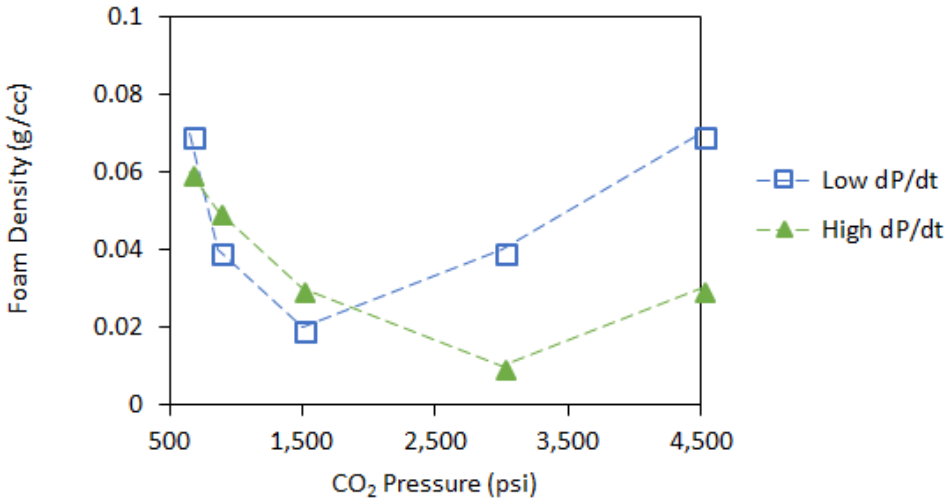

FIGURE 5.6: Effect of pressure drop rate (high and low) under various CO_2 pressures on the foam density of Borealis WB140.

Gas Pressure Effect, *P*

The SEM micrographs in Fig. 5.10 illustrate the cell morphology of foamed Borealis WB140 and branched PP1 at saturation CO_2 pressures of 1,500 psi, 3,000 psi, and 4,500 psi and given depressurization rates of about 16 MPa/s, 30 MPa/s, and 55 MPa/s respectively. The cell parameters as a function of CO_2 pressure are shown in Figures 5.11-5.14. Note that complete saturation of the sample is assumed before depressurization based on the sample thickness (e.g., 3 mm). Observation indicates that the cell morphology was greatly improved when the supercritical fluid (SCF) was added in the PP matrix. Furthermore, as it can be clearly seen from Fig. 5.10, the

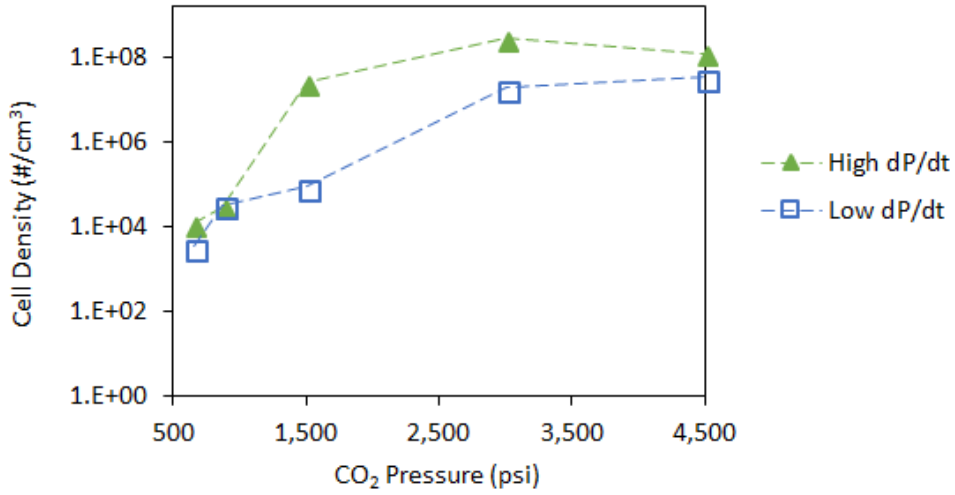

FIGURE 5.7: Effect of pressure drop rate (high and low) under various CO_2 pressures on the cell density of Borealis WB140.

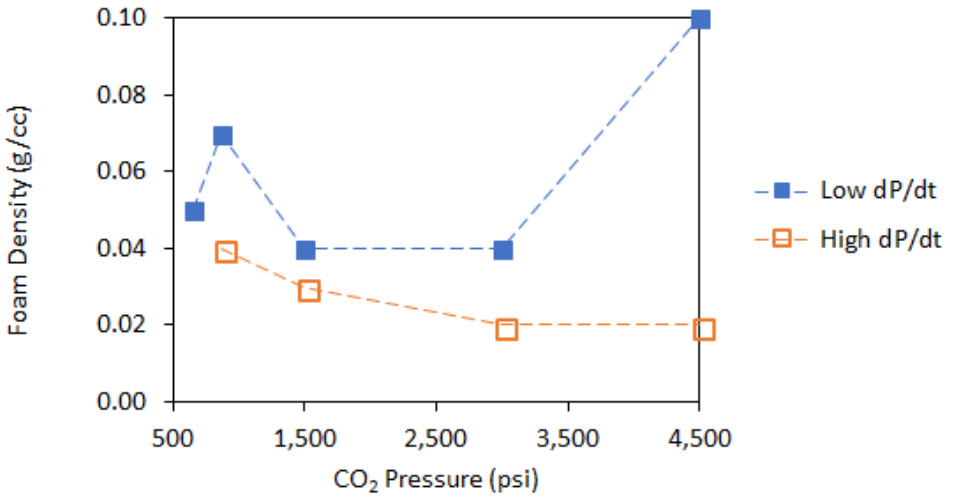

FIGURE 5.8: Effect of pressure drop rate (high and low) under various CO_2 pressures on the foam density of branched PP1.

cell size decreased and the cell density increased with the increase of SCF content. The lowest mean cell diameter obtained was approximately 50 μm at 4,500 psi CO_2 pressure.

The optimal foaming temperatures for each pressure condition were found experimentally and recorded in Table 5.5. This data is based on optimal foam density and cell density values. In general, the volume expansion behavior was changed

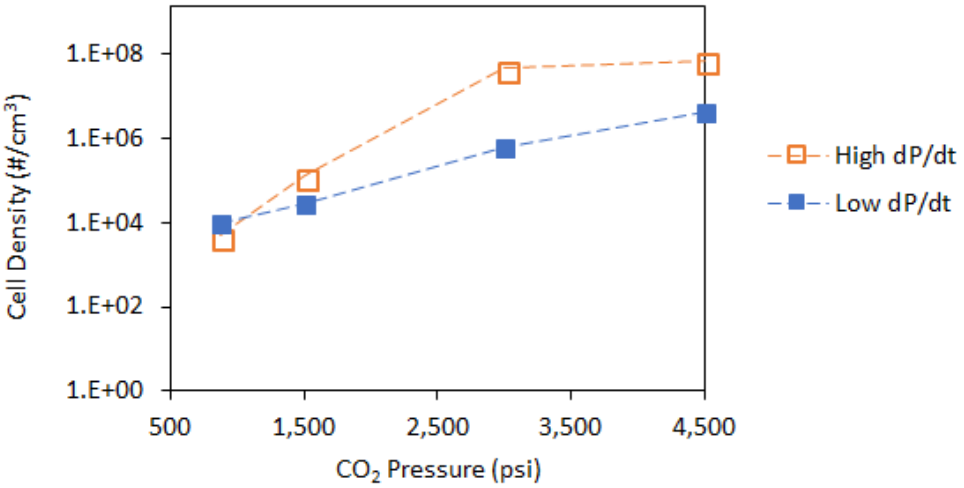

FIGURE 5.9: Effect of pressure drop rate (high and low) under various CO_2 pressures on the cell density of branched PP1.

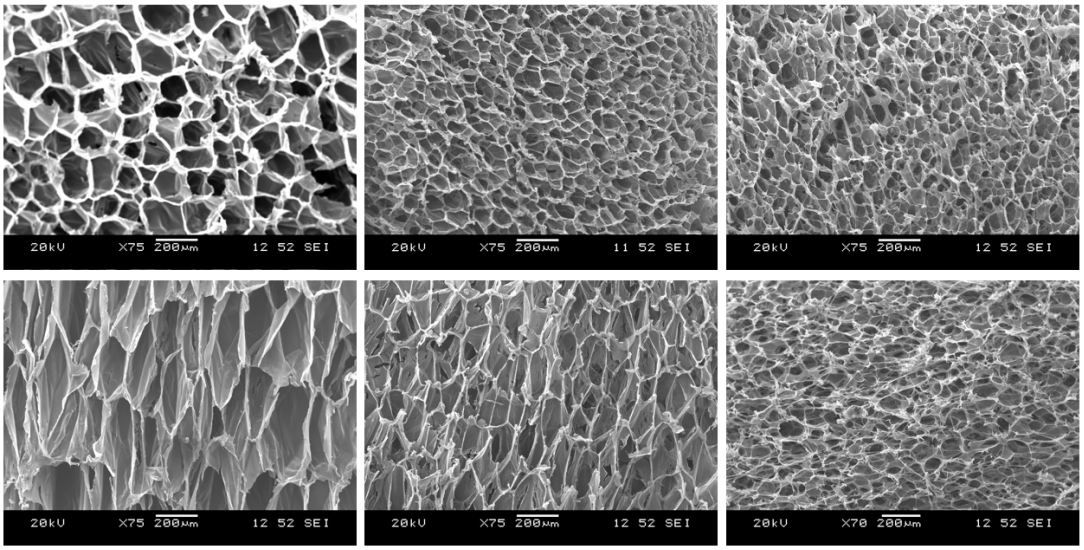

FIGURE 5.10: Cell population increases under (a) 1,500 psi, (b) 3,000 psi, and (c) 4,500 psi CO_2 pressure for both Borealis WB140 (upper raw) and branched P1 (lower raw) materials.

with the temperature in the same way as observed in previous studies: At high temperature, the volume expansion was governed by gas loss. Because of the high diffusivity of gas, the gas quickly escaped out to environment at elevated temperatures. As the temperature decreased, the amount of gas lost decreased because of the decreased diffusivity, and as a consequence, a greater amount of retained gas in

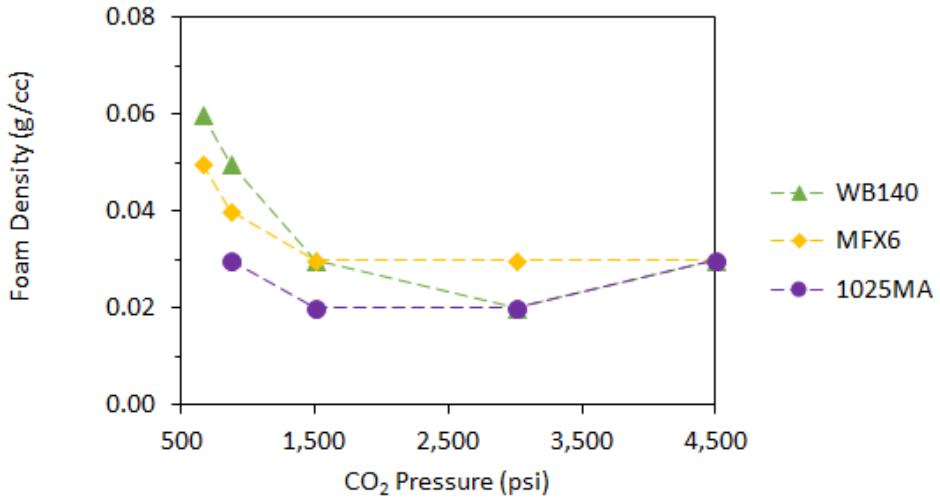

FIGURE 5.11: Effect of pressure on the foam density of control PP samples.

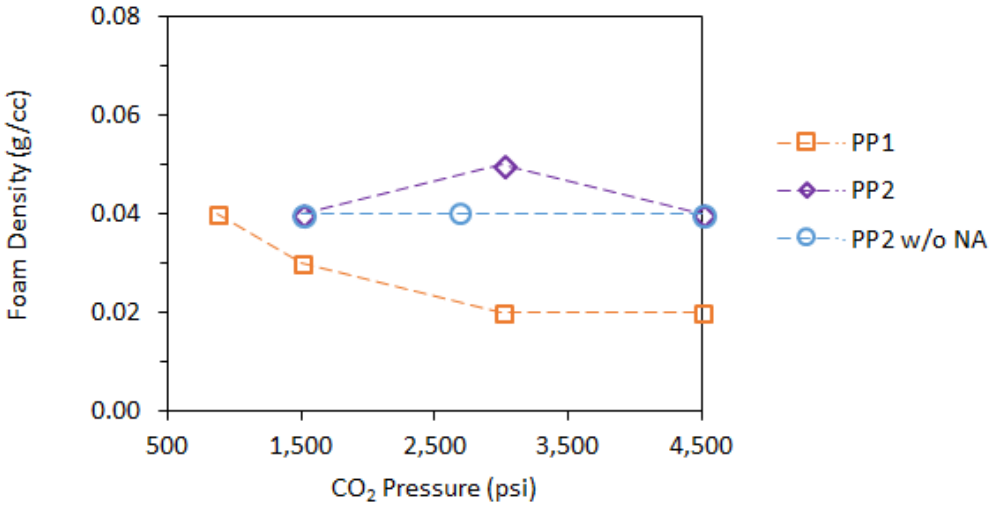

FIGURE 5.12: Effect of pressure on the cell density of control PP samples.

the foam resulted in an increased expansion ratio. But when the temperature was too low, the retained gas was not fully utilized to expand the foam because of the increased stiffness of polymer matrix, although the amount of gas lost could have been further decreased. So there seems to be an optimum temperature existing at each pressure condition where the retained gas is fully utilized to maximize the expansion ratio of the foamed PP samples.

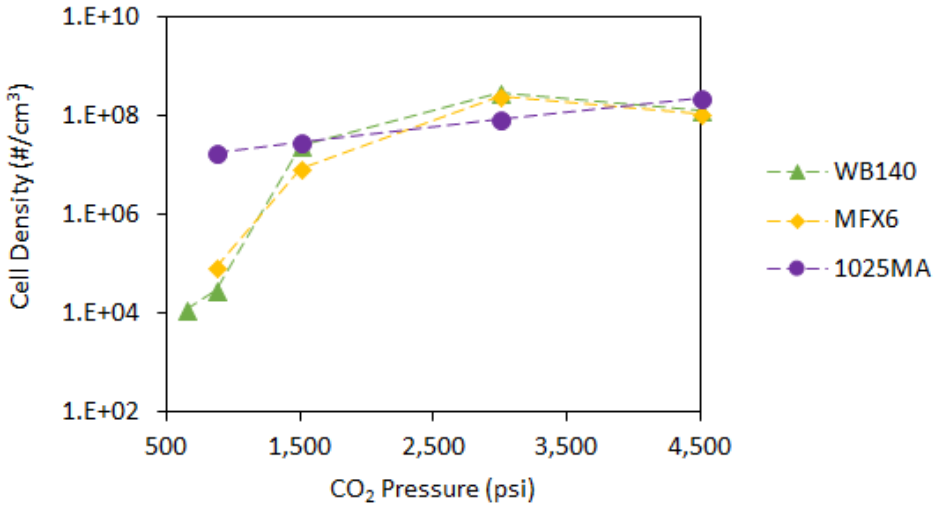

FIGURE 5.13: Effect of pressure on the foam density of linear and branched PP samples.

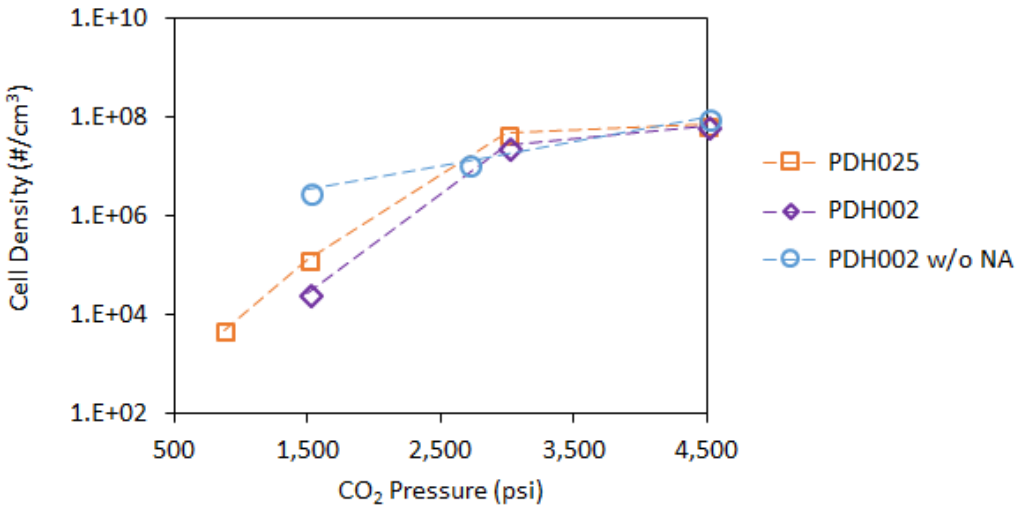

FIGURE 5.14: Effect of pressure on the cell density of linear and branched PP samples.

No trend was observed between CO_2 gas content and the open/closed cell contents. Open cell portion can contribute, for example, to convection mechanism since air can flow from one side to another in the foam, and such a flow can be seen upward or downward direction. Thus, convection in open cells can be a matter for

floor or ceiling insulators. However, one can assume that convection effect is negligible based on foam density values at various CO_2 pressure vs. open cell content results.

Material	**Port**	**Sorption and Foaming T** (°C)					T_{avg} (°C)
		653 psi	870 psi	1,500 psi	3,000 psi	4,500 psi	
WB140	2	158	150	155	155	150	155
	3	160	155	155	155	149	
PP1	2	150	150	150	150	155	150
	3	-	155	155	155	155	
PP2 w NA	2	-	-	-	150	-	155
	3	-	-	155	155	155	
MFX6	2	-	-	145	145	-	145
	3	145	145	140	140	140	
PP2 w/o NA	2	-	-	155	153	-	155
	3	-	-	150	155	153	
1025MA	2	-	157	155	155	155	155
	3	-	155	155	158	155	

TABLE 5.5: Foaming window and optimal foaming/saturation temperature at various CO_2 pressure conditions.

Additive Effect - Type and Amount

Microcellular polymer materials are widely used in industrial applications because of their lightness, thermal, sound insulation, and vibration absorption properties. However, these materials have lower mechanical, surface properties and dimensional stability in comparison to unfoamed polymers (Goren et al. 2010).

The addition of particles, as nucleating agents, followed by a careful control of the foaming conditions, could result in the formation of polymer foams having specific mechanical properties even better than their unfoamed polymer. One of the reasons is that the presence of particles (like talc) in the polymer matrix reduces the critical radius of the bubbles and the energy barrier needed for the bubble to reach the stabilization stage as explained in section 2.2.1.

In this experimental study, PP-based composite materials were produced by adding up to 3.0 wt% of talc and chemical blowing agent (CBA). The aim is to examine the effects of talc and CBA content on the foam morphology. The findings of this

work may further help to find the optimal processing window for HMS PP foams such as in structural or automotive applications.

There are two main processes to produce microcellular polymeric foams, basically depending on the way to introduce the gas into the polymer matrix. The first group involves the use of physical foaming agents (PBA). PBAs are gaseous products that are introduced directly into the barrel of an extruder or of the plasticating unit of an injection molding machine and mixed with the polymer matrix. As example, several types of PBAs such as CO_2, N_2, chlorofluorocarbons or argon are compatible for polypropylene foaming applications.

The second group of foaming processes involves the use of chemical blowing agents (CBA). Chemical blowing agents come in a variety of types, usually solid products. Some produce exothermic reactions, some produce endothermic reactions, some have a single component, while others are mixtures of many; and the temperatures at which they activate can vary. Despite these variables, all CBA's have one thing in common: The molecules are designed to decompose at a specific temperature and to produce a gas as part of that decomposition. This process effectively turns the batch foaming chamber into a 'chemical reactor' where time and temperature can influence the activation of the CBA. For this study XO-286 provided by Bergen International is used. Thermal characterization using HP-DSC and thermal gravimetric analysis (TGA) was carried out to determine the CBA activation temperature under various CO_2 foaming pressures.

Preliminary HP-DSC characterization at atmospheric pressure is presented in Fig. 5.15. A heating rate of 10 $^{\circ}C/min$ was chosen to assure similar heating rate as in the experimental foaming expansions. Two peaks between 100 °C and 220 °C correspond to the decomposition of XO-286 and endothermic reactions. Then, TGA measurements were performed to determine the quantity of gas released by the reactive elements in the CBA particles (Fig. 5.16). The relative weight loss refers to the original weight of the granule. The main weight loss (15.03%) corresponds to the second peak in the DSC scan at 217.3 °C. This means, to ensure decomposition

under atmospheric conditions our operating temperature should be approximately 220°C under atmospheric pressure.

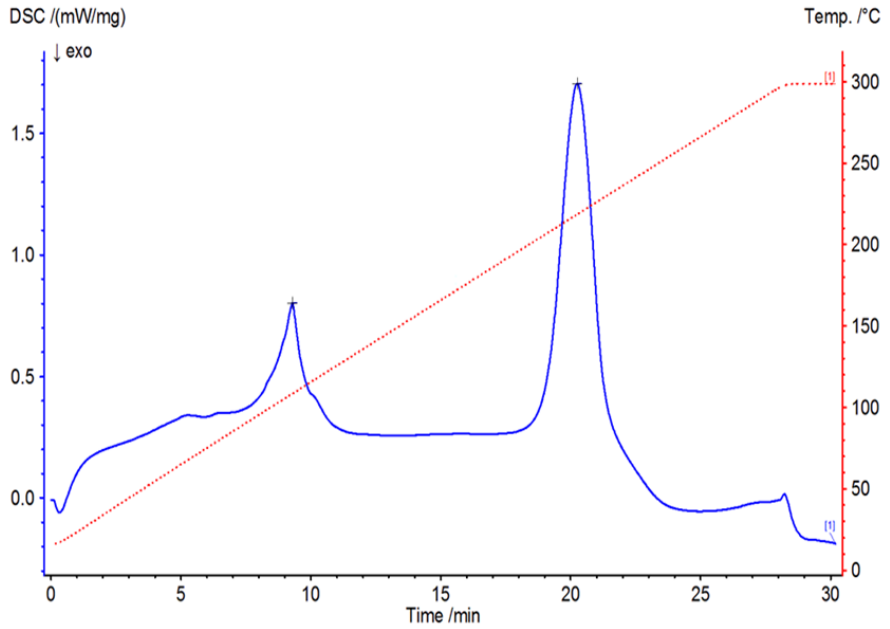

FIGURE 5.15: HP-DSC scan of CBA XO-286 shows two endothermic reactions at 100 °C and 220 °C.

In addition, the CBA was activated under high CO_2 pressures to simulate batch foaming conditions. Fig. 5.17 and 5.18 show decomposition temperatures of the CBA for first and second endothermic reactions respectively. As can be observed, activation temperatures decrease under CO_2 pressure. This suggests a recommended minimum activation temperature for the CBA of 130 °C under foaming conditions (653-4,500 psi). This temperature is conveniently lower than experimental foaming (e.g. saturation) temperatures used for this study. Therefore, we can ensure full decomposition of the CBA during the foaming process.

Importantly, SEM images presented in Fig. 5.19 suggest that increase of talc wt% and/or CBA wt% may led to a higher cell nucleation rate and cell density.

In this case, we can see that density of foamed PP (both control and studied foams) increased first and then decreased with increased additive content (see Figs. 5.20 and 5.21). On the other hand, when the additive content increases, cell count

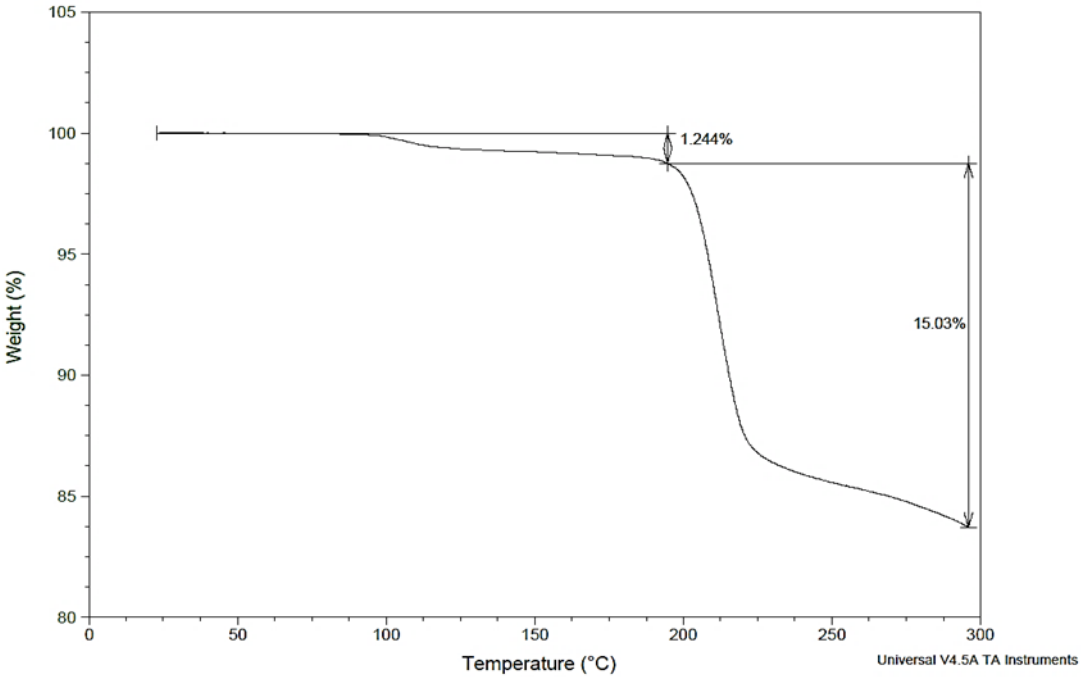

FIGURE 5.16: The TGA analysis showed main weight loss of CBA XO-286 at 200 °C.

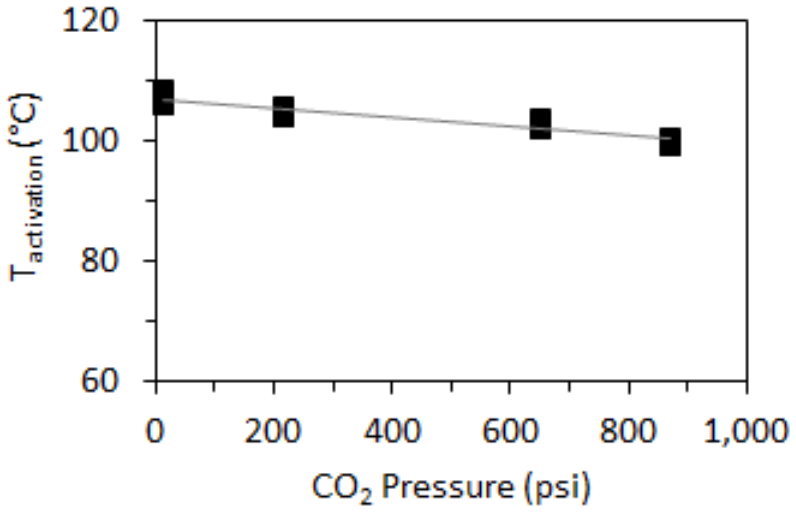

FIGURE 5.17: First activation peak of CBA XO-286 under various CO_2 pressure.

also increases (see Figs. 5.22 and 5.23). We believed that talc could work negatively to increase the open cell fraction and thereby increase foam density.

If the additive content is 1.5 wt%, a sharp increase in cell count of foamed PP is

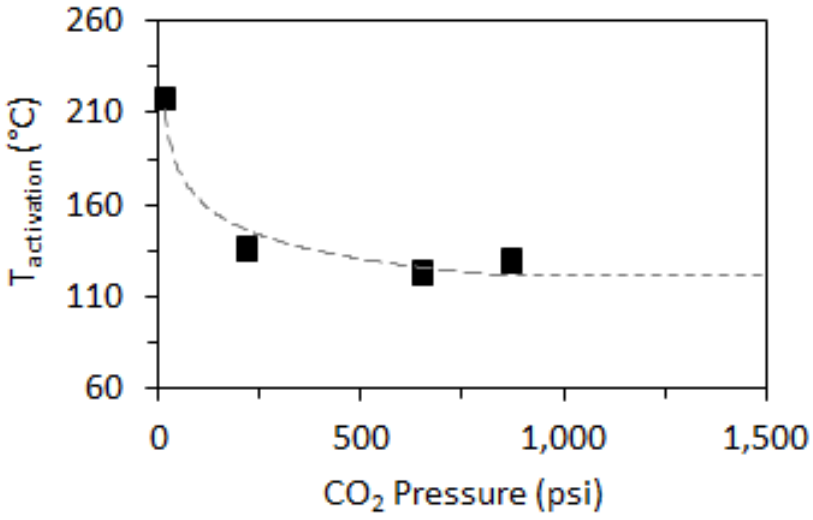

FIGURE 5.18: Second activation peak of CBA XO-286 under various CO_2 pressure.

obtained with $1.07 \cdot 10^7$ cells/cc, which is relatively closed compared to previous cell density values presented previously after increasing CO_2 pressure (see Fig. 5.11). However, not much difference was observed between 1.5 wt% and 3.0 wt%, which suggest an optimum additive content between 0.5 wt% - 1.5 wt%. Similar results were found in previous studies (Kaewmesri et al., 2006), where 0.8 wt% talc was found to produced optimum expansion ratio of HMS PP foams.

As a result, preliminary data suggest than in batch foaming and extrusion foaming processes, both CO_2 pressure and additive content can be used as measures to enhance the cell count and foam density of HMS PP foams.

Summary

In this study, low density, fine-celled PP foams were successfully produced by using various types of linear and branched HMS PP resins as polymeric matrix. A high pressure drop rate was selected to promote optimum conditions at various foaming temperatures and CO_2 pressures. Furthermore, CO_2 pressure and additive content were utilized as a blowing agent. The effects of varying CO_2 and additive

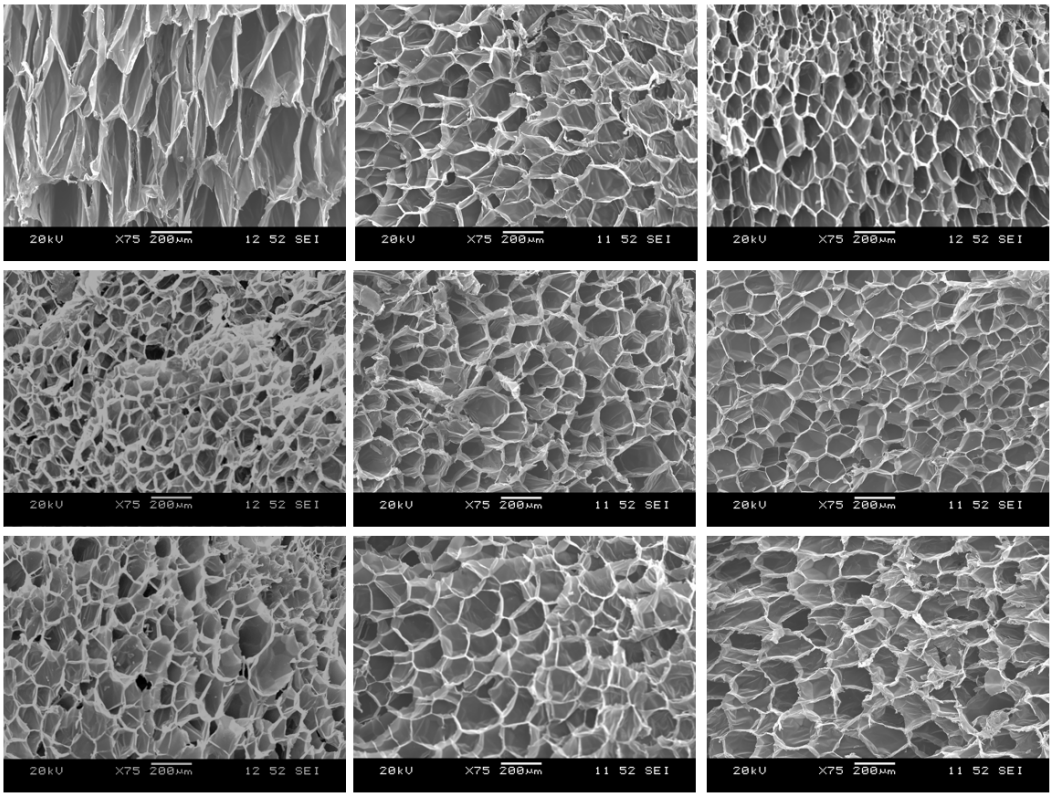

FIGURE 5.19: SEM micrographs of PP1 with chemical blowing agent (CBA XO-286) content increase: (upper raw) 0%, (middle raw) 1.5% and (lower raw) 3.0%, and talc content increase (Talc HT4HP) (a) 0%, (b) 1.5%, and (c) 3.0% foamed at 1,500 psi CO_2 pressure and high pressure drop rate (12.4 MPa/s).

contents on volume expansion ratio and cell nucleation behaviors were thoroughly investigated. The experimental results were concluded as the following:

- Foam density decreased as CO_2 content and CO_2 **pressure drop rate** increased, and the expansion ratios showed mountain shaped curves. The lowest foam density 0.01 g/cc (WB140) was successfully obtained at 3,000 psi CO_2 pressure.
- The **CO_2 content** played an important role on the cell nucleation behavior when foaming these polymers without additive particles. The cell density was noticeably increased as the CO_2 content was increased while the bubble size decreased. The maximum number of cells, up to 10^8 cells/cm^3 and small cells (less than 100 μm), were easily achieved in this experiment.

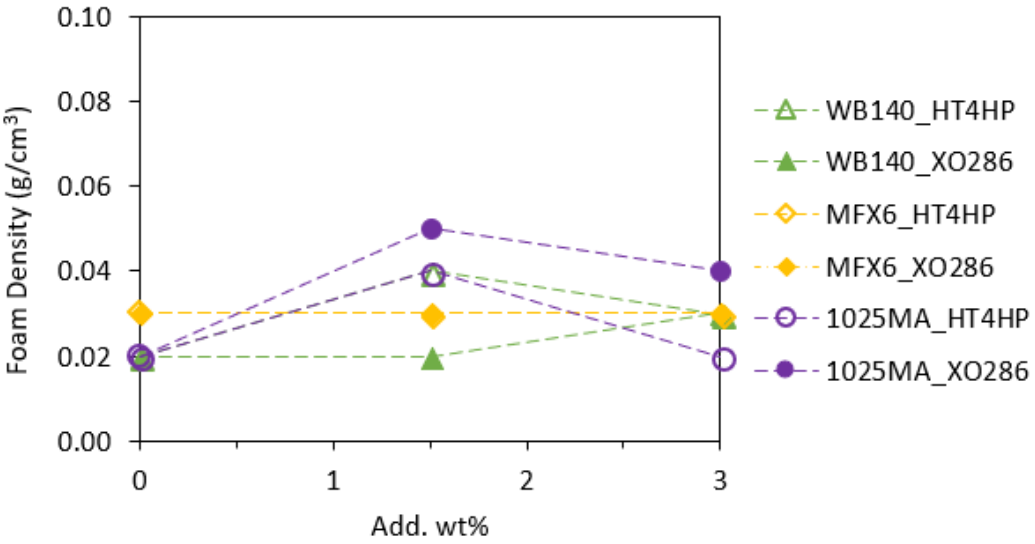

FIGURE 5.20: Effect of additive on the foam density of control PP samples under 1,500 psi CO_2 pressure and high pressure drop rate (12 MPa/s).

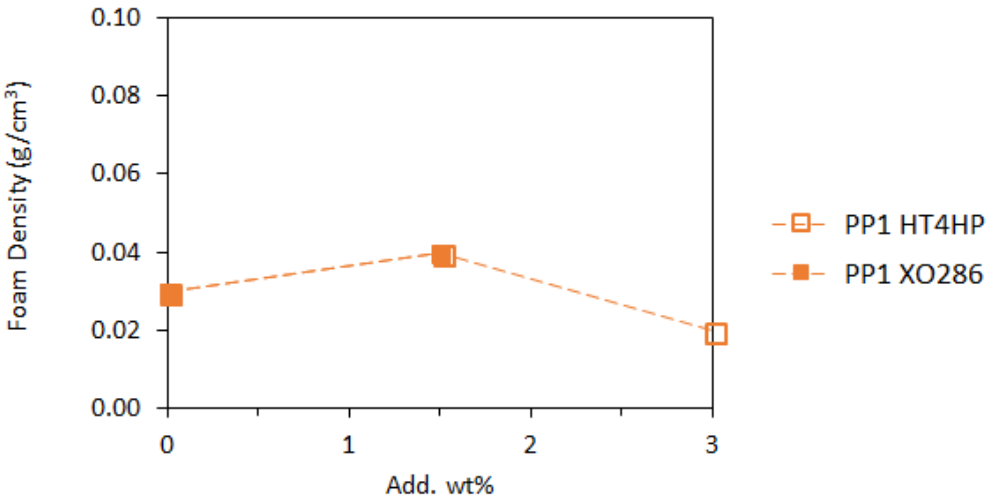

FIGURE 5.21: Effect of additive on the foam density of linear and branched PP samples under 1,500 psi CO_2 pressure and high pressure drop rate (12 MPa/s).

- Similarly, cell density increased as **additive content** increased, and the expansion ratios was maintained fairly constant. The highest cell density 10^8 cells/cc was successfully obtained at 1.5 %wt, which is in the same order of magnitude that the optimal value achieved under CO_2 pressure.

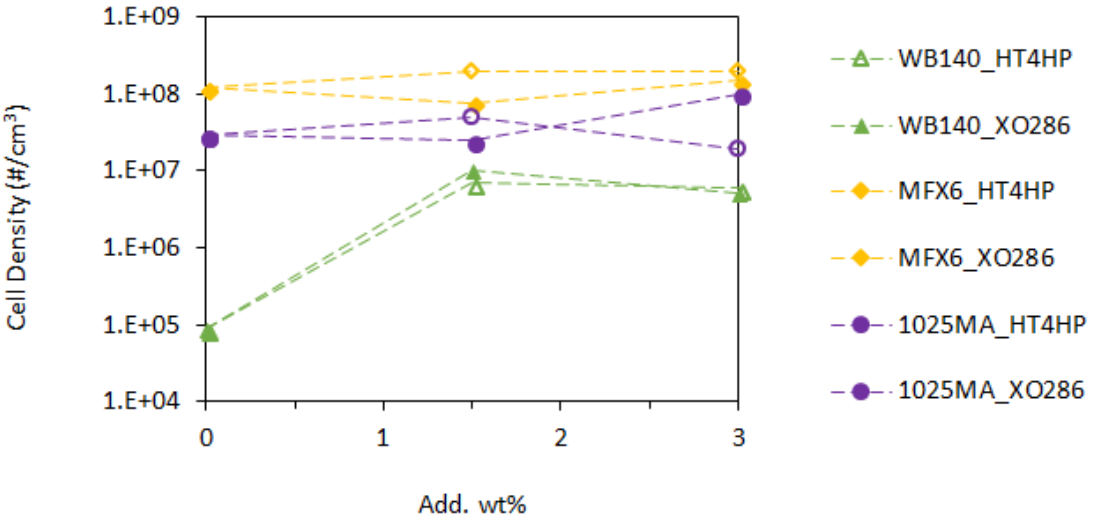

FIGURE 5.22: Effect of additive on the cell density of control PP samples under 1,500 psi CO_2 pressure and high pressure drop rate (12 MPa/s).

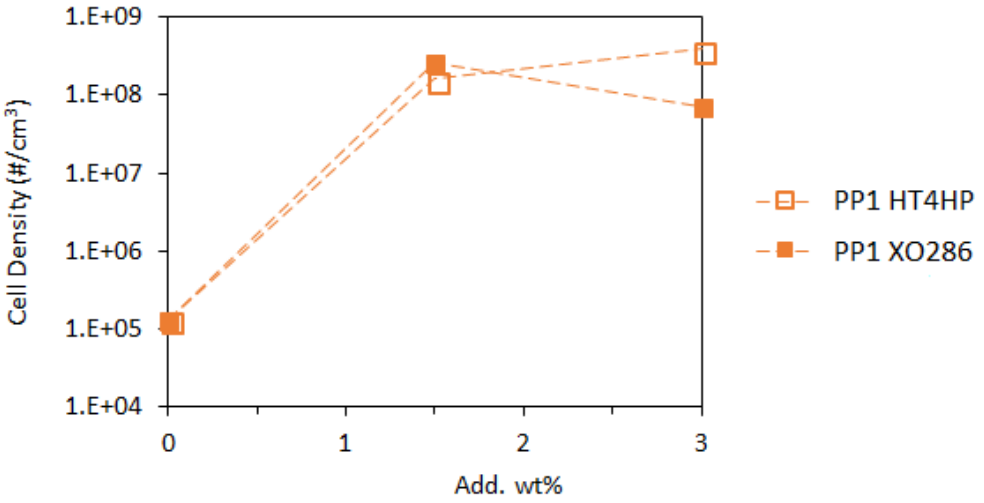

FIGURE 5.23: Effect of additive on the cell density of linear and branched PP samples under 1,500 psi CO_2 pressure and high pressure drop rate (12 MPa/s).

- The additive content efficiency did not increase proportionally to the increase in wt%. The maximum additive efficiency was achieved between 0.5-1.5 %wt for both talc and CBA.

- Additive content showed little effect in cell density and cell size when subjected to high CO_2 pressure drop rate. This could be due to the effect of additive masked by the pressure drop rate effect. Therefore, studies on additive type and amount should be done under low CO_2 pressures and low CO_2 pressure drop rates.

5.4.2 Crystallization Study

The melting temperatures T_m and crystallization temperatures T_c of various polymer/gas systems were characterized using a HP-DSC (DSC 204 HP Phoenix). The gas pressure was increased to the required level using an ISCO 500D syringe pump. The HP-DSC was calibrated with In, Sn, Pb, and Zn under ambient and high pressure. The following procedure was applied for every measurement. After the sample is installed, the system was evacuated for 5 min. Samples were heated up at a constant heating rate of 10 °C/min to 200°C during 10 min in order to erase the thermal history of the polymer. During the cooling and heating processes, the crystallization and melting patterns of the samples were recorded. The degree of crystallinity was determined based on the heating cycle in the DSC thermogram. DSC scan were obtained in J/g.

Gas Pressure Effect, P

The effect of CO_2 pressure on the crystallization behaviors of PP materials was analyzed. Because the solubility of CO_2 in PP is relatively high, a linear decrease in T_m and T_c could be observed in Figs. 5.24 and 5.25, respectively. Based on the experimental results for the six polymers, it seems that the dissolved CO_2 accelerates the crystallization rate under non-isothermal conditions reducing T_c for every case. Similar results have been reported in Mizoguchi et al. (1987) and Handa, Zhang, and Wong, 1997, where it was postulated that gas dissolved into the polymer increases the free volume, hence the mobility of polymeric chains by reducing the interchain interactions. The increased mobility accelerates the transport processes

at the amorphous phase-crystalline phase interface. Therefore, when the polymer is non-isothermally crystallized, we could observed that CO_2 dissolution accelerates the overall crystallization rate.

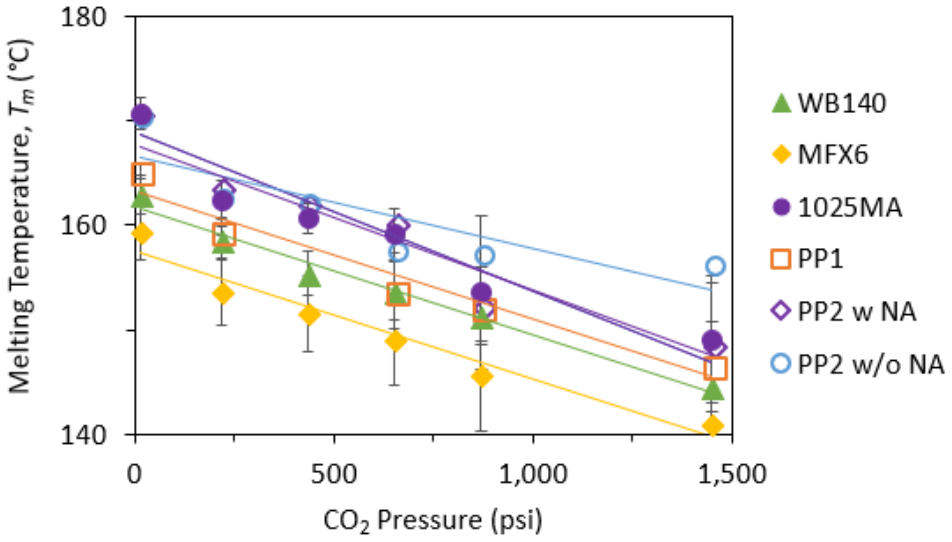

FIGURE 5.24: Melting temperatures of various PP samples under CO_2 pressure.

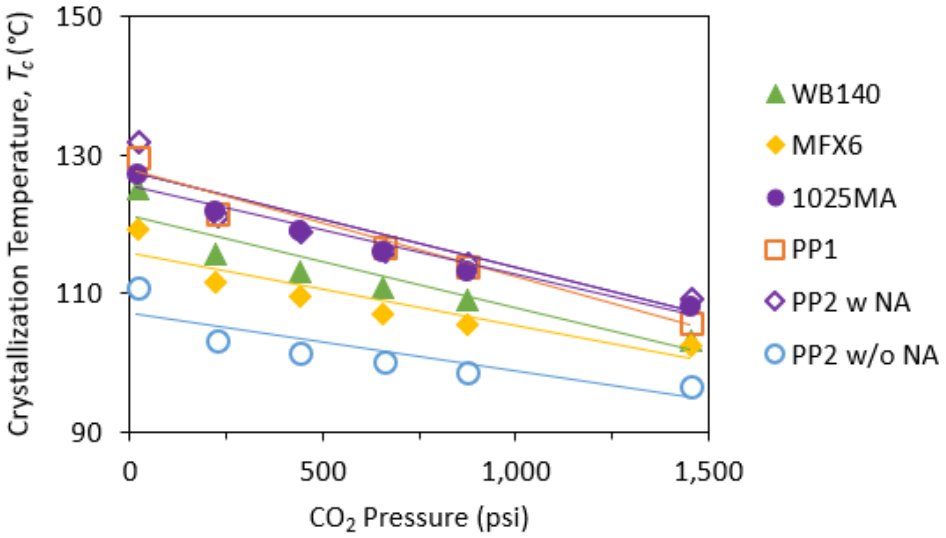

FIGURE 5.25: Crystallization temperatures of various PP samples under CO_2 pressure.

Additive Effect

In addition to the effects of the processing parameters on the cell morphology of foamed samples, the materials parameters and foaming additives can also contribute to changes in crystallization temperatures. Therefore, the identification of the crystallization behavior of PP resin with talc additives plays an important role in the study of foaming. Therefore, thermal behaviors of linear and branched PP resins with foaming additives were investigated in this study. The concentration of CBA was changed from 0 to 1.5 wt%.

Fig. 5.26 shows the effect of CBA amounts on the crystallization temperatures of PP materials under CO_2 pressures. It was observed that the degree of crystallinity of branched PP increased moderately as the CBA concentration increased. However, no particular trend was found in the case of T_m (see Fig. 5.27) with increase additive content.

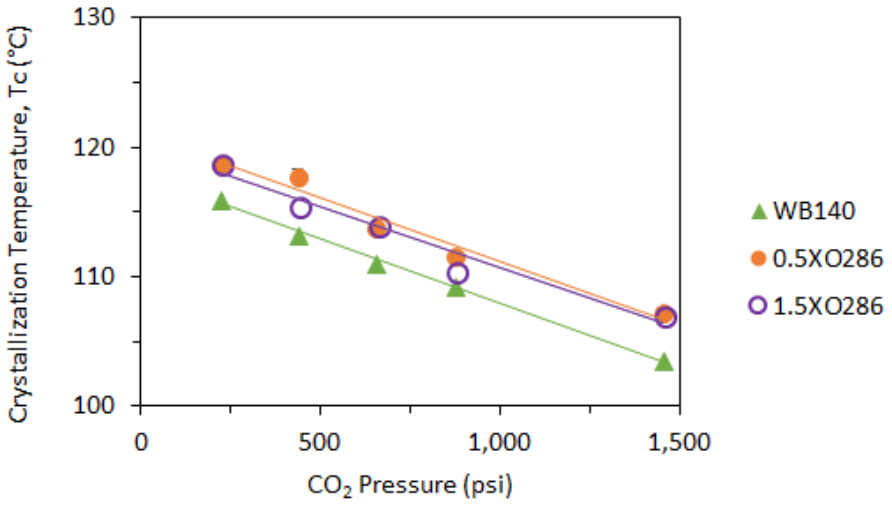

FIGURE 5.26: Effect of additive on the crystallization temperatures of Borealis WB140 PP under CO_2 pressures.

It is believed that the presence of the talc particles in the PP melt decrease the mobility of the polymer molecules, which led to an early crystallization and hence a high crystallization temperature was obtained (Naguib, Park, and Lee 2003).

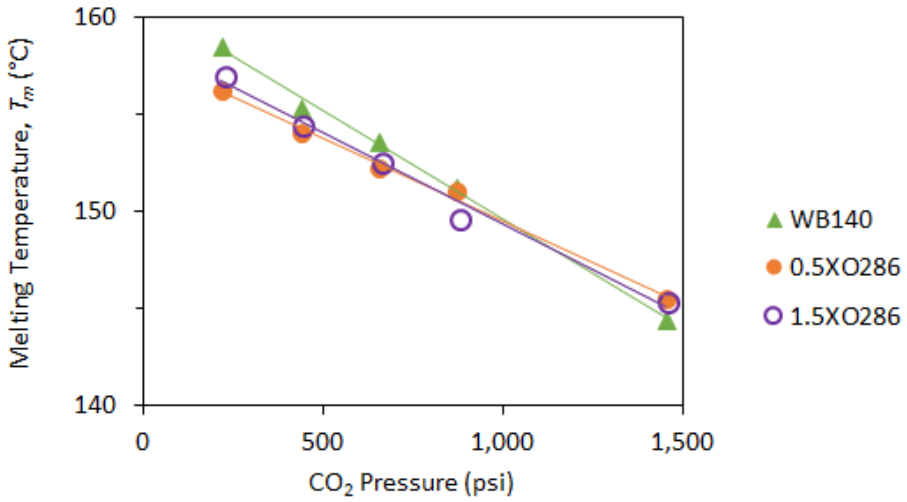

FIGURE 5.27: Effect of additive on the melting temperatures of Borealis WB140 PP under CO_2 pressures.

Effect of Isothermal Temperature, T_{iso}

For this study, we investigated the melting and crystallization temperatures of random copolymer (RC-PP) and poly(propylene-co-ethylene) block copolymer (BC-PP) resins. A RC-PP resin has a random configuration of two monomers in the backbone of the copolymer, because the polymerization reaction begins with two monomers mixed in the same reactor from the beginning. But a BC-PP resin is polymerized through a stepwise process. In this way, a homo PP resin, which is polymerized with a pure propylene monomer at the first stage is transferred and blended with the two propylene and ethylene monomers in the second stage. This is done to further polymerize the amorphous ethylene-propylene rubber (EPR), which enters a dispersed phase in the homo PP's matrix.

Similar to previous sections, the first part of this study focuses on the thermal properties of the two copolymers using differential scanning calorimeter (DSC 204 HP Phoenix) under non-isothermal conditions. The DSC experiment samples were taken from the initially received pellets with a sample size between 5-10 mg. The

samples were heated from the room temperature up to 200 °C, and then were maintained at 200 °C for 10 minutes to eliminate their thermal histories. Next, the samples were cooled at a ramp rate of -10 ° C/min under a nitrogen purge, and then a second heating and a second cooling were performed at a ramp rate of 10 ° C/min, and -10 °C/min respectively. We recorded the two copolymers' melting and crystallization behaviors during the second heating and cooling processes (see Table 5.6).

Sample	P (psi)	T_m (°C)	T_c (°C)
BC-PP	14.5	167.26	121.55
BA212E	653	156.65	111.40
RC-PP	14.5	144.63	105.36
CR200P	653	132.99	89.55

TABLE 5.6: Melting and crystallization temperature of BC- and RC-PP under atmospheric and 653 psi CO_2 pressures.

The second part of the study was performed under isothermal conditions at the given CO_2 pressure of 653 psi. DSC thermograms for both BC and RC are shown in Figs. 5.28 and 5.29, respectively. Using these DSC results and the Avrami technique, the X_c developed over time at each isothermal temperature was analyzed to study the isothermal crystallization kinetics. Figs. 5.30 and 5.31 show the corresponding Avrami double-log plots for the neat BC-PP and RC-PP at 653 psi. Tables 5.7 and 5.8 summarize all the values of the Avrami exponent (n) and the kinetic constant (k) derived from the Avrami double-log plots for both PP materials.

The values of n for RC-PP ranged from 1.7-2.6, suggest that the crystals consisted mainly of a two-dimensional disc-like growth. The polymerization of BC-PP through a stepwise process apparently produces increase in n values higher than 2.5 in most isothermal treatments. This suggests that through the polymerization process, it might be possible to alter the crystallization from two-dimensional disc-like growth to three-dimensional spherulitic growth.

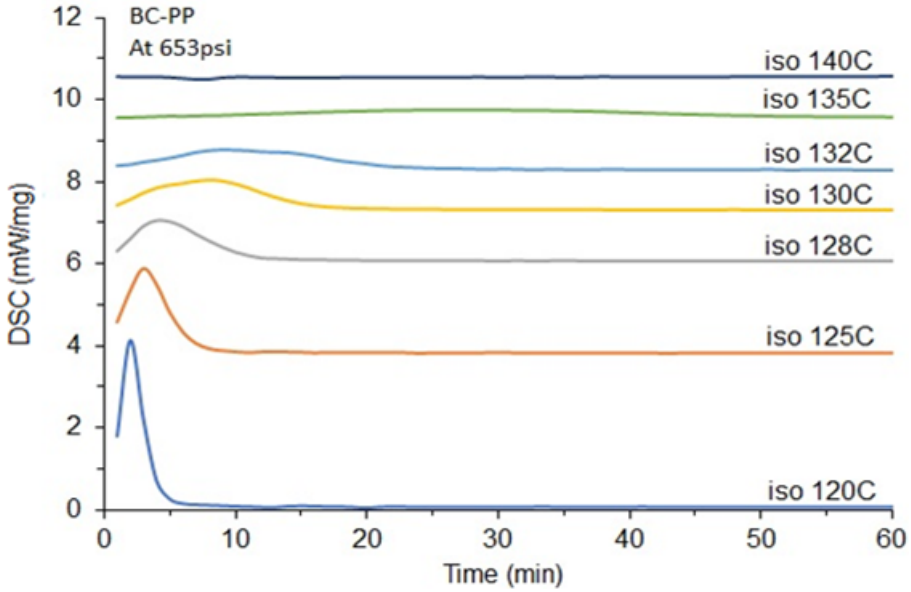

FIGURE 5.28: DSC isothermal scans of BC-PP at various isothermal temperatures and 653 psi CO_2 pressure.

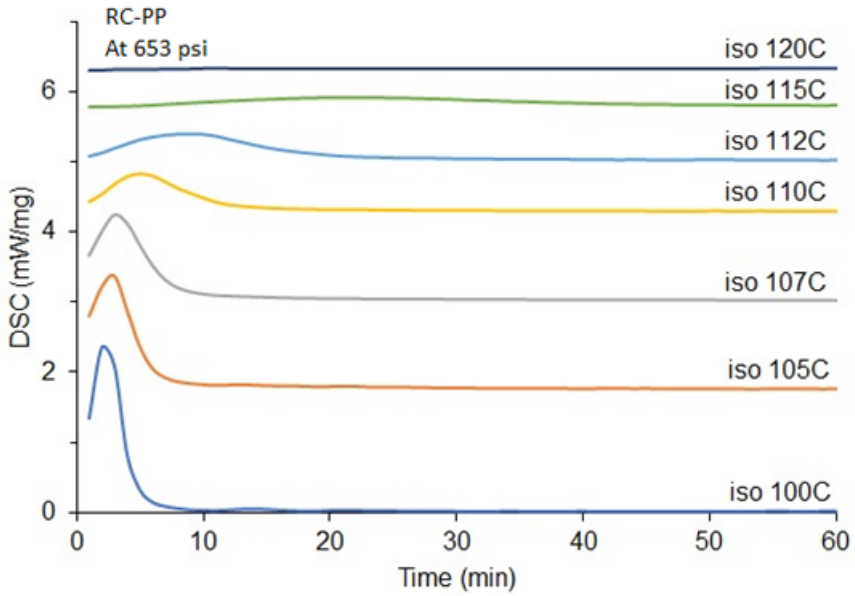

FIGURE 5.29: DSC isothermal scans of RC-PP at various isothermal temperatures and 653 psi CO_2 pressure.

Summary

We conducted a detailed study of the melting behavior and crystallization kinetics of polymer/CO_2 systems using a HP-DSC, which is a powerful tool that provides increased and valuable polymer/gas information. This was done under various pressure conditions in a high-pressure DSC. We found that the presence of CO_2

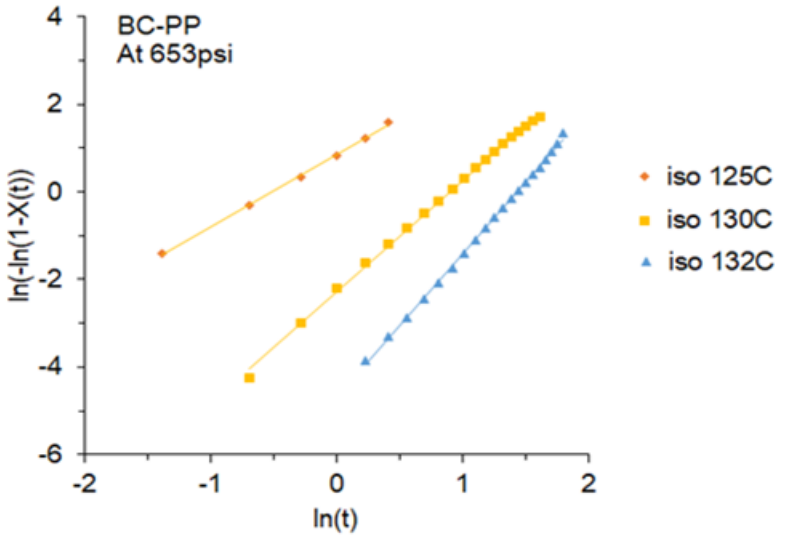

FIGURE 5.30: Avrami analysis of BC-PP at 653 psi CO_2 pressure.

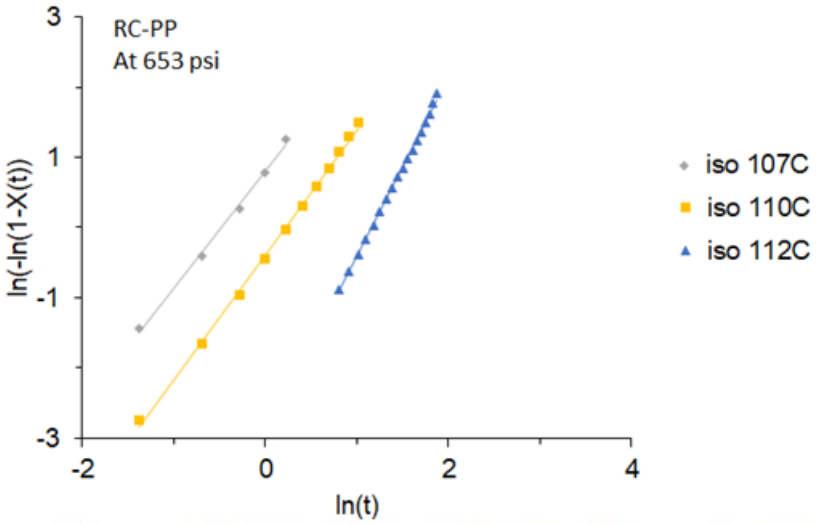

FIGURE 5.31: Avrami analysis of RC-PP at 653 psi CO_2 pressure.

Sample	653 psi					
	T_{iso} (°C)	$t_{1/2}$ (min)	G (min^{-1})	n	ln k	k
BC-PP BA212E	125	0.48	2.102	1.6512	0.86	2.363
	130	3.12	0.471	2.5434	-2.28	1.02E-1
	132	3.72	0.269	3.2815	-4.69	9.29E-3

TABLE 5.7: Summary of the Avrami parameters for BC-PP at 653 psi CO_2 pressure.

had a significant influence on non-isothermal crystallization of PP. Under high CO_2 pressure, a linear depression in T_m and T_c was induced due to the plasticization

Sample	653 psi					
	T_{iso} (°C)	$t_{1/2}(min)$	G ($\min^{-1}$)	n	ln k	k
RC-PP CR200P	107	0.50	2.020	1.6583	0.80	2.225
	110	1.01	0.988	1.7800	-0.39	6.78E-01
	112	2.78	0.360	2.5708	-2.99	5.02E-02

TABLE 5.8: Summary of the Avrami parameters for RC-PP at 653 psi CO_2 pressure.

effect of dissolved CO_2. During the isothermal crystallization process, PP's crystallization kinetics were affected by the pressurized CO_2 and selected isothermal temperature. The crystallization process was accelerated when T_{iso} was closed to T_c, but depressed at higher temperatures. These very high-pressure DSC data will be effectively used for various applications such as foam and supercritical technology.

5.4.3 Blending Study

In this study, polymer blends of PP1 and PP2 with NA were investigated to determine the effects of processing conditions and blend composition. Polymers are often blended to create new functions, which each polymer alone cannot express, or to compensate for the weakness in the mechanical properties of each polymer. The aim of this study is to use polymer blends to create fine cell structures by choosing a suitable temperature.

When polymer blends are foamed, we find that the cellular structure is determined not only by the morphology and viscosity of the blend polymers but also by the solubility and diffusivity of the physical foaming agent in the polymers. Therefore, there is a strong possibility of creating various cell structures by the blending of polymers. The mechanism of foaming such a unique cellular structure of PP1/PP2 was investigated from the viewpoint of cellular structure and foam density of the blend.

Fig. 5.32 shows the SEM results and expansion ratio of foamed PP1/PP2 at various PP1 concentrations. Because PP1 and PP2 are miscible with each other at microscopic level, the micrographs show homogeneous cell morphology for every concentration amount (e.g., 0:100, 10:90, and 20:80 PP1/PP2). An increase in the PP1 weight fraction made the number of cells increase and overall cell size decrease, with average cell size diameter of less than 200 μm and cell density of the order 10E+8 cells/cc (see Fig. 5.33). Therefore, it seems that a prominent difference in cell nucleation is produced by the formation of blend polymer structure, and that the cell density could be altered through introducing different contents of PP2 w NA under CO_2 pressure.

A significant increase in bulk foam density was measured for the samples foamed at higher PP2 content (see Fig. 5.33). The increase of density may be caused by smaller cells of the blend foams in comparison to the cells of neat PP1.

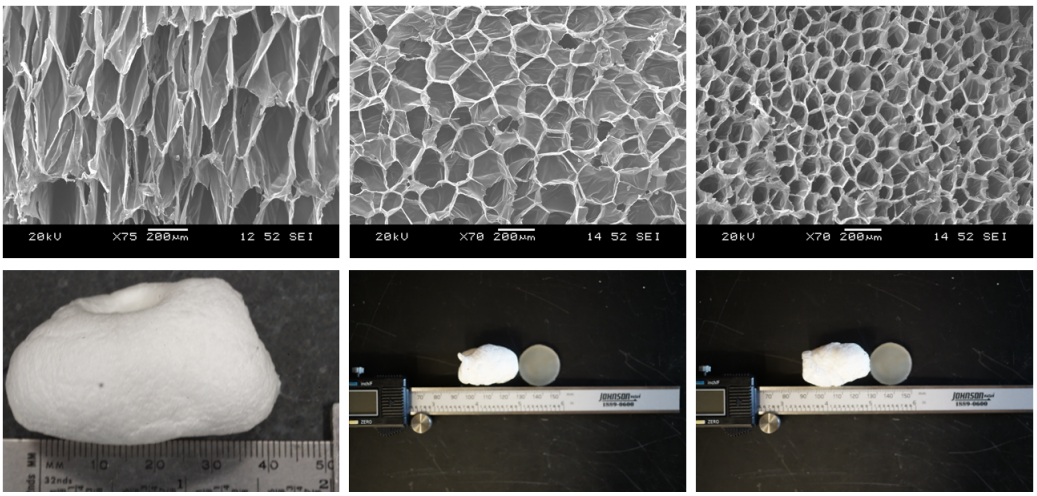

FIGURE 5.32: Cell structures of PP1/PP2 with ratios (a) 100:0, (b) 90:10, and (c) 80:20 foams prepared with % $scCO_2$ at a foaming temperature of 145 °C

For future work, CO_2 contents, temperatures, pressure drops, blend ratios and clay are variables of clear interest. As the solubility of CO_2 would vary with temperature and pressure drop, and with changing parameters of CO_2 contents, temperatures and pressure drops, we could tune the cell structure between bimodal and uniform and could thus verify the possible formation mechanisms regarding bimodal

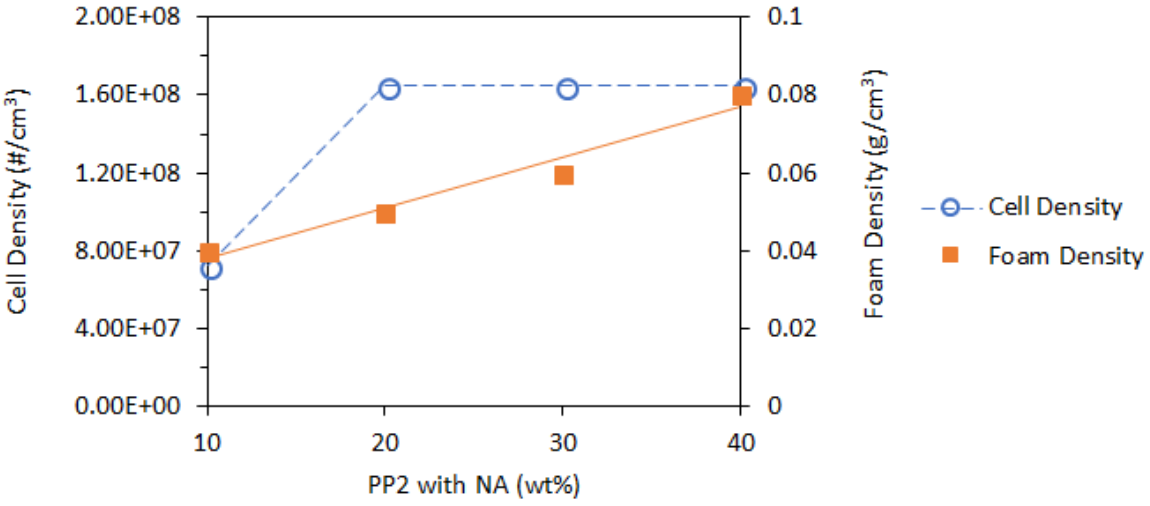

FIGURE 5.33: Effect of PP1:PP2 blending on the foam and cell density of PP1 under 1,500 psi CO_2 pressure and high pressure drop rate.

cell structure. In addition, we could obtain the minimum cell nucleation difference between PP1 phase and PP2 phase required for formation of bimodal cell structure. For the blend ratios, we could build a relationship between the phase morphology and bimodal cell structure. And for the clay, we could verify the uniformizing effect of the nanoparticles on the cell structure. For immediate future work using visualization equipment, we could validate the effect of shear and extensional stresses having a positive effect on cell nucleation. Some studies from other researchers show that bimodal cell structure could form in some binary polymer blends due to a prominent difference in viscoelasticity of the two polymers. Thus, it would be an interesting topic to study the effect of shear on cell nucleation of such polymer blends.

Chapter 6

Summary and Concluding Remarks

6.1 Summary

Crystal nucleation and growth phenomena in plastic foaming processes determine the final foam morphology, and hence the foam's quality and application. The successful study of high-quality foams with customizable cell morphologies (e.g., high cell density foams with low foam density) hinges on the scientific interdisciplinary advancement and knowledges of thermodynamics, kinetics, and rheological behaviors of the polymer. In this context, fundamental mechanisms of the coupled polymer foaming and crystal formation were investigated via in situ observation experiments and numerical simulations, difficult to be achieved in typical foaming equipment. This fundamental understanding could provide valuable insights into the resulting micro- /nanocellular structures and the development of innovative plastic foaming technologies and foams.

6.2 Key Contributions

6.2.1 New Foaming and In-Situ Visualization Techniques

Three custom made high-pressure foaming systems have been successfully utilized for purpose of the presented work in this thesis: 1) a custom build static system with accurate heating and cooling control; 2) a custom build dynamic system with shear stress-inducing ability; 3) a custom designed batch foaming chamber.

The dynamic system with shear stress-inducing ability is novel: in-situ observation of plastic foaming processes under uniform and controlled shear stress has not been achieved previously. Both the static and dynamic systems permit concurrent studies to be conducted with a high-pressure DSC and to compare crystallization kinetics and foaming behavior of semi-crystalline polymers. Both of these systems open a wide range of potential research opportunities, especially with semi-crystalline polymers where crystallization kinetics significantly influence the foaming behavior as well as the mechanical properties of the final foamed products.

The batch foaming chamber with high-pressure, high-temperature, and accurate pressure drop rate control capabilities allows plastic foaming under easily adjustable and controllable variables. This is a key contribution to the field of industrial plastic foaming because plastics are subjected to highly dynamic and complex environments where the control of isolated variables can play an essential role in understanding the fundamental foam behavior of newly developed polymers.

6.2.2 Simulation and Numerical Work

Using a high-pressure static chamber, batch foaming experiments were conducted by pressure release, and the simultaneous nucleation, bubble growth rate, and collapse were observed at very early stages of the foaming process under a high resolution polarized optical microscope (POM). A model was newly developed to account for the simultaneous cell nucleation, growth, and collapse processes of the foaming bubbles. The simulation model and experimental results showed good agreement.

An underlying result of power law distributions was found in the cell size distribution of the final foam structure of experimental and simulation data.

6.2.3 Experimental Work

This study leads to the following contributions and conclusions:

1. The dissolution of CO_2 increased the crystallization rate in the crystal-growth-controlled region (self-diffusion controlled region) and depresses in the nucleation-controlled region.

2. Through in-situ observation of PP and PLA crystallization, the effects of pure shear stress have been examined. It has been shown that the application of pure shear significantly increased crystal nucleation rate and crystal nucleation density for both PLA and PP.

3. It was hypothesized that the stress-inducing crystal nucleation was due to: 1) decrease in local system pressure; 2) increase in gas solubility due to polymer chain alignment; and 3) generation of microvoids that promote heterogeneous nucleation.

4. Through thermal analysis techniques, the synergistic effect of the high plasticization effect of CO_2 have been demonstrated. To be specific, polymer/gas systems subjected at higher pressures showed a linear decrease in T_m and T_c.

5. Low-bulk density ($<$0.1 g/cc) closed to microcellular structure (10^8 cells/cc) thermoplastic foams were successfully achieved by tailoring the material and processing conditions. The experimental results demonstrated the effectiveness of the proposed strategies adopted to promote the desired foam structures.

6. The strategies for the manufacture of a large cell density were threefold:

   (i) to induce a high thermodynamic instability by utilizing a high pressure-drop rate and high temperature drop

(ii) to increase the amount supercritical CO_2 dissolved in the polymer

(iii) to induce heterogeneous nucleation by using polymer blending and/or solid foaming agent

7. The strategies employed for the promotion of a large expansion ratio with thermoplastic materials were threefold:

   (i) to completely dissolve blowing agent(s) in the melt by using a high pressure chamber and to reduce the premature growth of second-phase bubbles by using a high pressure drop rate

   (ii) to increase the injected gas amount while maintaining a single gas/polymer phase solution

   (iii) to decrease cell wall thickness by optimizing temperature conditions and maintaining the soft sections of cell walls

8. When additive between 0.5-1.5 wt% was dispersed in the polymer matrix, the cell count could be promoted with careful control of the processing conditions.

9. As the CO_2 content increased, the expansion ratios and the cell densities increased, and the foam density decreased.

10. The pressure-drop rate also increased the expansion ratios, the cell densities, and decreased the foam density.

Bibliography

Baldwin, DF and NP Suh (1992). "Microcellular poly (ethylene terephthalate) and crystallizable poly (ethylene terephthalate): Characterization of process variables". In: *ANTEC 92–Shaping the Future.* 1, pp. 1503–1507.

Burnett, Bruce B and WF McDevit (1957). "Kinetics of spherulite growth in high polymers". In: *Journal of Applied physics* 28.10, pp. 1101–1105.

Carraher Jr, Charles E (2003). *Seymour/Carraher's polymer chemistry*. CRC Press.

Costeux, Stéphane (2014). "CO2-blown nanocellular foams". In: *Journal of Applied Polymer Science* 131.23.

Ding, WeiDan (2016). "Development of Polylactic Acid/Cellulose Nanofiber Biocomposite Foams". PhD thesis.

Emami, Maryam, Michael R Thompson, and John Vlachopoulos (2014). "Bubble nucleation in nonpressurized polymer foaming systems". In: *Polymer Engineering & Science* 54.5, pp. 1201–1210.

Fan, Jintian, JR Mitchell, and JMV Blanshard (1994). "A computer simulation of the dynamics of bubble growth and shrinkage during extrudate expansion". In: *Journal of Food engineering* 23.3, pp. 337–356.

Faruk, Omar, Andrzej K Bledzki, and Laurent M Matuana (2007). "Microcellular Foamed Wood-Plastic Composites by Different Processes: a Review". In: *Macromolecular Materials and Engineering* 292.2, pp. 113–127.

Feng, James J and Christopher A Bertelo (2004). "Prediction of bubble growth and size distribution in polymer foaming based on a new heterogeneous nucleation model". In: *Journal of Rheology* 48.2, pp. 439–462.

Goren, Kerem et al. (2010). "Influence of nanoparticle surface chemistry and size on supercritical carbon dioxide processed nanocomposite foam morphology". In: *The Journal of Supercritical Fluids* 51.3, pp. 420–427.

Handa, Y Paul, Zhiyi Zhang, and Betty Wong (1997). "Effect of compressed CO2 on phase transitions and polymorphism in syndiotactic polystyrene". In: *Macromolecules* 30.26, pp. 8499–8504.

Harris, Angela M and Ellen C Lee (2008). "Improving mechanical performance of injection molded PLA by controlling crystallinity". In: *Journal of applied polymer science* 107.4, pp. 2246–2255.

Höhne, Günther Walther Heinrich, Wolfgang Hemminger, and H-J Flammersheim (1996). "Theoretical fundamentals of differential scanning calorimeters". In: *Differential Scanning Calorimetry*. Springer, pp. 21–40.

Huang, Erbo et al. (2016). "Effect of unexpected CO2's phase transition on the high-pressure differential scanning calorimetry performance of various polymers". In: *ACS Sustainable Chemistry & Engineering* 4.3, pp. 1810–1818.

Janeschitz-Kriegl, H et al. (1983). "On the kinetics of polymer crystallization under shear". In: *European polymer journal* 19.10-11, pp. 893–898.

Kaewmesri, Wanrudee et al. (2006). "Effects of CO2 and talc contents on foaming behavior of recyclable high-melt-strength PP". In: *Journal of cellular plastics* 42.5, pp. 405–428.

Kee, Eung (2010). *Novel manufacturing processes for polymer bead foams*. Citeseer.

Keith, HD and FJ Padden Jr (1963). "A phenomenological theory of spherulitic crystallization". In: *Journal of Applied Physics* 34.8, pp. 2409–2421.

— (1964). "Spherulitic crystallization from the melt. I. Fractionation and impurity segregation and their influence on crystalline morphology". In: *Journal of Applied Physics* 35.4, pp. 1270–1285.

Klempner, Daniel and Vahid Sendijarevic (2004). "Polymeric foams and foam technology". In: *2nd. ed*.

Koga, Yoshiaki and Hiromu Saito (2006). "Porous structure of crystalline polymers by exclusion effect of carbon dioxide". In: *Polymer* 47.21, pp. 7564–7571.

Leung, Siu Ning Sunny (2009). "Mechanisms of cell nucleation, growth, and coarsening in plastic foaming: theory, simulation, and experiment". PhD thesis.

Li, Junsong et al. (2017). "Crystals in Situ Induced by Supercritical CO2 as Bubble Nucleation Sites on Spherulitic PLLA Foam Structure Controlling". In: *Industrial & Engineering Chemistry Research* 56.39, pp. 11111–11124.

Mizoguchi, Keishin et al. (1987). "CO2-induced crystallization of poly (ethylene terephthalate)". In: *Polymer* 28.8, pp. 1298–1302.

Naguib, Hani E, Chul B Park, and Patrick C Lee (2003). "Effect of talc content on the volume expansion ratio of extruded PP foams". In: *Journal of cellular Plastics* 39.6, pp. 499–511.

Nofar, Mohammadreza et al. (2013). "Comparison of melting and crystallization behaviors of polylactide under high-pressure CO2, N2, and He". In: *Polymer* 54.23, pp. 6471–6478.

Oda, Takafumi and Hiromu Saito (2004). "Exclusion effect of carbon dioxide on the crystallization of polypropylene". In: *Journal of Polymer Science Part B: Polymer Physics* 42.9, pp. 1565–1572.

Okada, Tetsuo, Hiromu Saito, and Takashi Inoue (1994). "Kinetic studies of crystallization in mixtures of isotactic polystyrene and atactic polystyrene". In: *Polymer* 35.26, pp. 5699–5705.

Padden Jr, FJ and HD Keith (1959). "Spherulitic crystallization in polypropylene". In: *Journal of applied Physics* 30.10, pp. 1479–1484.

Park, Hee Eon and John M Dealy (2006). "Effects of pressure and supercritical fluids on the viscosity of polyethylene". In: *Macromolecules* 39.16, pp. 5438–5452.

Patrick Lee, CD (2006). "Extrusion Processing of Low-Bulk Density, Microcellular, Open-cell Thermoplastic Foams". PhD thesis. MSc Thesis, University of Toronto.

Price, Fraser P (1959). "GROWTH AND ORGANIZATION OF HIGH-POLYMER SPHERULITES". In: *Annals of the New York Academy of Sciences* 83.1, pp. 20–26.

Russell, Kenneth C (1980). "Nucleation in solids: the induction and steady state effects". In: *Advances in Colloid and Interface Science* 13.3-4, pp. 205–318.

Schmidt, C et al. (1994). "Differential thermal analysis (DTA) and differential scanning calorimetry (DSC) at high pressures. Experimental techniques and selected results". In: *Thermochimica acta* 238, pp. 321–336.

Schnablegger, Heimo and Yashveer Singh (2011). "The SAXS guide: getting acquainted with the principles". In: *Austria: Anton Paar GmbH*.

Shafi, Muhammad A, James G Lee, and Raymond W Flumerfelt (1996). "Prediction of cellular structure in free expansion polymer foam processing". In: *Polymer Engineering & Science* 36.14, pp. 1950–1959.

Sherwood, Charles Herbert (1977). "The effect of shear on polymer crystallization kinetics." In:

Tabatabaei, Alireza et al. (2017). "Visualization of polypropylene's strain-induced crystallization under the influence of supercritical CO2 in extrusion". In: *Polymer* 122, pp. 312–322.

Takada, Mitsuko, Shigeki Hasegawa, and Masahiro Ohshima (2004). "Crystallization kinetics of poly (L-lactide) in contact with pressurized CO2". In: *Polymer Engineering & Science* 44.1, pp. 186–196.

Takayanagi, Motowo and Tatsuya Yamashita (1956). "Growth rate and structure of spherulite in fractionated poly (ethylene adipate)". In: *Journal of Polymer Science* 22.102, pp. 552–555.

Taki, Kentaro (2008). "Experimental and numerical studies on the effects of pressure release rate on number density of bubbles and bubble growth in a polymeric foaming process". In: *Chemical Engineering Science* 63.14, pp. 3643–3653.

Taki, Kentaro, Hideyuki Hayashizaki, and Kiyoshi Fukada (2014). "A Simplified Bubble Nucleation, Growth and Coalescence Model for Coke Production Process". In: *ISIJ International* 54.11, pp. 2493–2502.

Taki, Kentaro, Daisaku Kitano, and Masahiro Ohshima (2011). "Effect of growing crystalline phase on bubble nucleation in poly (L-lactide)/CO2 batch foaming". In: *Industrial & Engineering Chemistry Research* 50.6, pp. 3247–3252.

Tammaro, D et al. (2016). "Validated modeling of bubble growth, impingement and retraction to predict cell-opening in thermoplastic foaming". In: *Chemical Engineering Journal* 287, pp. 492–502.

Tiang, Jen Shueng and John M Dealy (2012). "Shear-induced crystallization of isotactic polypropylene studied by simultaneous light intensity and rheological measurements". In: *Polymer Engineering & Science* 52.4, pp. 835–848.

Venerus, David C (2015). "Diffusion-induced bubble growth and collapse in yield stress fluids". In: *Journal of Non-Newtonian Fluid Mechanics* 215, pp. 53–59.

Wang, Jing (2009). "Rheology of foaming polymers and its influence on microcellular processing". PhD thesis.

Wong, Anson et al. (2011). "A batch foaming visualization system with extensional stress-inducing ability". In: *Chemical engineering science* 66.1, pp. 55–63.

Wong, Anson Sze Tat (2012). "In Situ Observation of Plastic Foaming under Static Condition, Extensional Flow and Shear Flow". PhD thesis.

Xu, Huan et al. (2012). "Formation of shish-kebabs in injection-molded poly (L-lactic acid) by application of an intense flow field". In: *ACS applied materials & interfaces* 4.12, pp. 6774–6784.

Zhai, Wentao et al. (2007). "Influence of long-chain branching on the crystallization and melting behavior of polycarbonates in supercritical CO2". In: *Macromolecules* 40.1, pp. 73–80.

Zhang, Zheng-Chi et al. (2017). "Enhanced heat deflection resistance via shear flow-induced stereocomplex crystallization of polylactide systems". In: *ACS Sustainable Chemistry & Engineering* 5.2, pp. 1692–1703.

Zhu, Wenli, Nanqiao Zhou, and Hongwei Wu (2006). "Multiplex shear stress-induced nucleation in dynamic microcellular foaming process". In: *Polymer Engineering & Science* 46.12, pp. 1728–1738.

Appendix A

System for Visualizing and Measuring Stress of Plastic Flows Under Shear Conditions

A.1 Introduction

Many previous studies have built novel equipment to better understand properties of polymer melts in-situ under various processing conditions. To better understand crystallization of polylactic acid (PLA) in extrusion, Tabatabaei et al. incorporated a view cell into the die exit, capturing the effect of the complex stress field on polymer melts during industrial polymer processing (Tabatabaei et al. 2017). Additional studies have isolated the shear effect on polymer melts (Tiang and Dealy 2012, Park and Dealy 2006). Anson et al. designed a shearing view cell to study the effect of shear on polymer gas systems (Wong et al. 2011). Anson was able to isolate the effect of shear on the foaming of polystyrene (PS)/CO_2 for various strain and strain rates. While effectively demonstrating a change in foaming properties due to applied shear, this system lacked the ability to measure the shear stress/viscosity due to that action. To better characterize the effect of shear on polymer melts, it was desired to implement a measurement technique into Anson's system to extract rheological data about the flow. A shear stress transducer developed by Dealy and used by Park and Dealy in a high pressure sliding plate rheometer developed (HP-SPR) at McGill. Combining these two aspects into a single system would allow one to characterize in-situ polymer melts—both visually and quantitatively—through

rheological methods.

In summary, the focus of this study was to design and build a system that would maintain the desired function from each system while not detracting from the other. This led to the manufacturing of a so-called high pressure sliding plate chamber (HP-SPC). The components of the HP-SPC are detailed in Figures A.1 and A.2. The processing window of the HP-SPC is as follows: shear rate (0.01-600 s^{-1}), strain (0.01-100) with an 0.5 mm sample, temperature (up to 200 °C), pressures (up to 35 MPa (5000 psi), sample thickness (50-1000 μm), heating rate (up to 15 °C/min), and cooling rate (up to 5 °C/min).

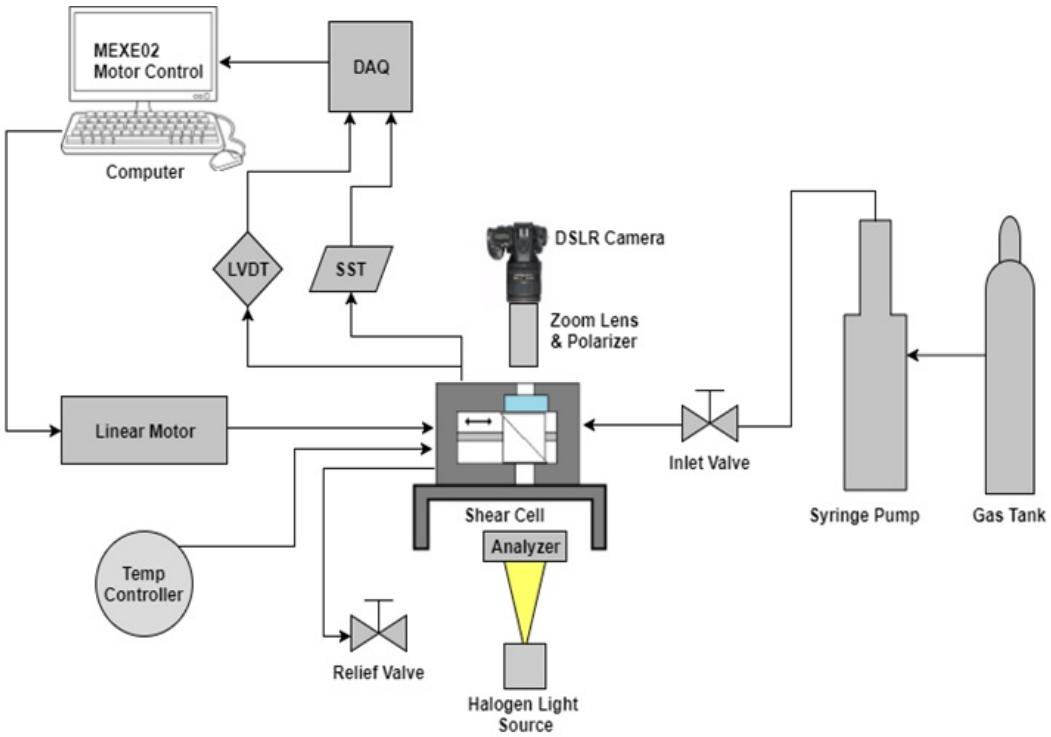

FIGURE A.1: Crystallization visualization facility with strain inducing capability.

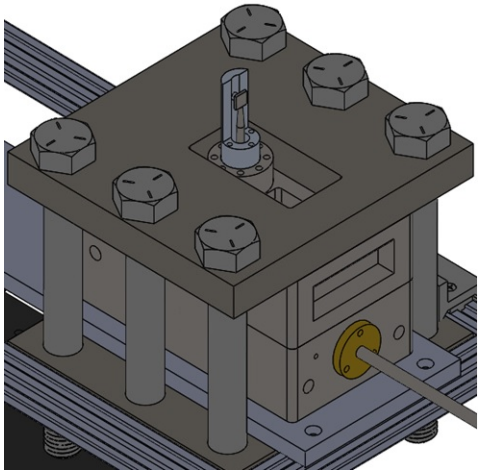

FIGURE A.2: Isometric view of the HP-SPC System.

A.2 Materials and Sample Preparation

To verify the system capability, plastic crystallization experiments were conducted on PLA saturated with CO_2 gas under various conditions. The plastic material used was commercially available semi-crystalline PLA (IngeoTM 8052D, 4.5 mol %D-content) provided by NatureWorks LLC. The PLA had a density and melt flow index of 1.24 g/cm^3 and 14 g/10 min (210 °C/2.16 kg), respectively. CO_2, (99% purity), was used as a saturation gas. The PLA material was compression-molded into thin films 0.06 mm thick using a Carver Press at 200 °C and 4 tons of pressure. While under pressure, the samples were cooled to 25 °C. The samples were cut into rectangles measures 30 mm wide by 50 mm long and 0.06 mm thick.

A.3 Experimental Procedure

The PLA sample was loaded into the HP-SPC shown in Fig. A.3 and heated to 200 °C for 20 minutes under various pressures of CO_2 gas to allow for saturation and erasing thermal history of the sample. After saturation, the sample was raised up to the upper plate of the chamber using a micro-adjuster. The sample was actively cooled to an isothermal temperature, T_{iso}, with a proportional gain to the crystallization temperature, T_c, for a cooling rate of 3 °C/min. Once the T_{iso} was

reached, the sample was subjected to various strains and shear strain rates. Crystal formation was observed and captured using an optical system composed of a high-resolution DSLR camera (SONY α99ii), coupled with a Vimeo Machine Vision lens system, polar optical microscopy (POM) filters, and transmittive halogen light source. Figure A.4 details high-resolution images of crystals formed under various pressures of CO_2, during both static and shear (γ = 25, $\dot{\gamma}$ = 30 s^{-1}) conditions. This proved that the capability of visualizing high spatial resolution features in-situ.

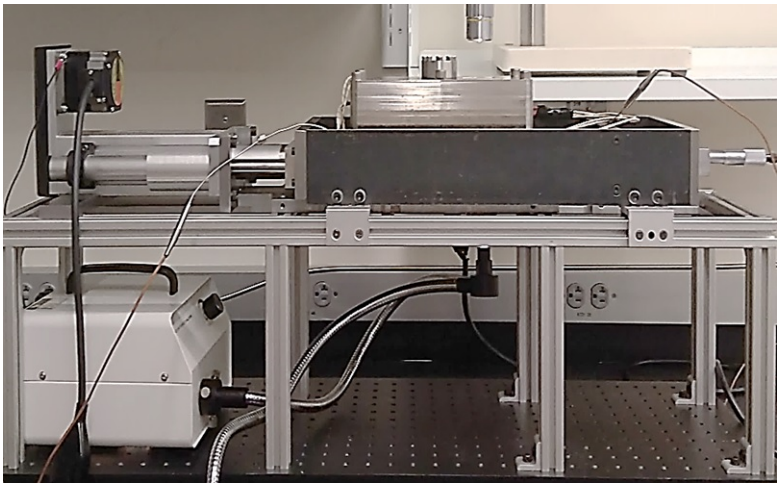

FIGURE A.3: Visualization system of HP-SPC

A.4 System Development

A.4.1 Function I: Saturating the Plastic Melt with High Pressure Gas and Maintaining High Pressure

The first modification we made to Anson's et. al design was to greatly increase the pressure capability of the system (Wong et al. 2011). Many foaming studies use pressures upwards of 25 MPa (3,626 psi) to increase nucleation density and decrease cell size in foams. To accommodate these and other studies of interest, an addition of a clamping system was employed. The clamping system consists of two 1" thick plates of hardened 4340 steel which are connected by six 1" x 9" steel bolts and encase the HP-SPC as shown in Figure A.2.

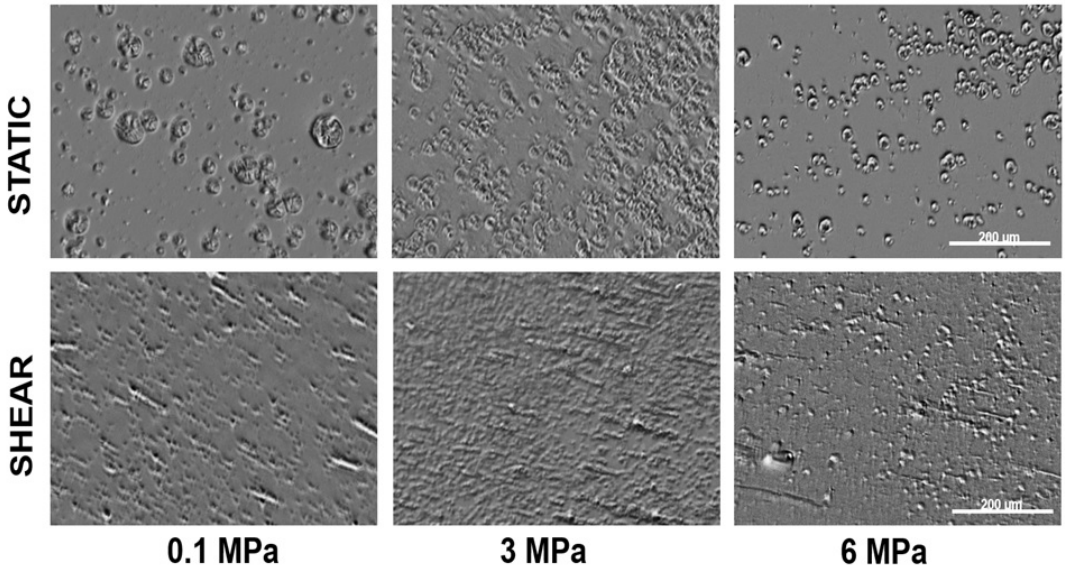

FIGURE A.4: POM micrographs of neat PLA at various CO_2 pressures during isothermal melt crystallization under static (upper) and shear conditions (γ= 25, $\dot{\gamma}$ 30 s^{-1}) (lower).

Prior to machining, an FEA analysis of the plates was conducted to verify that under the expected loads that the plates would a) withstand the mechanical stress and b) resist deflection near the primary o-ring seal.

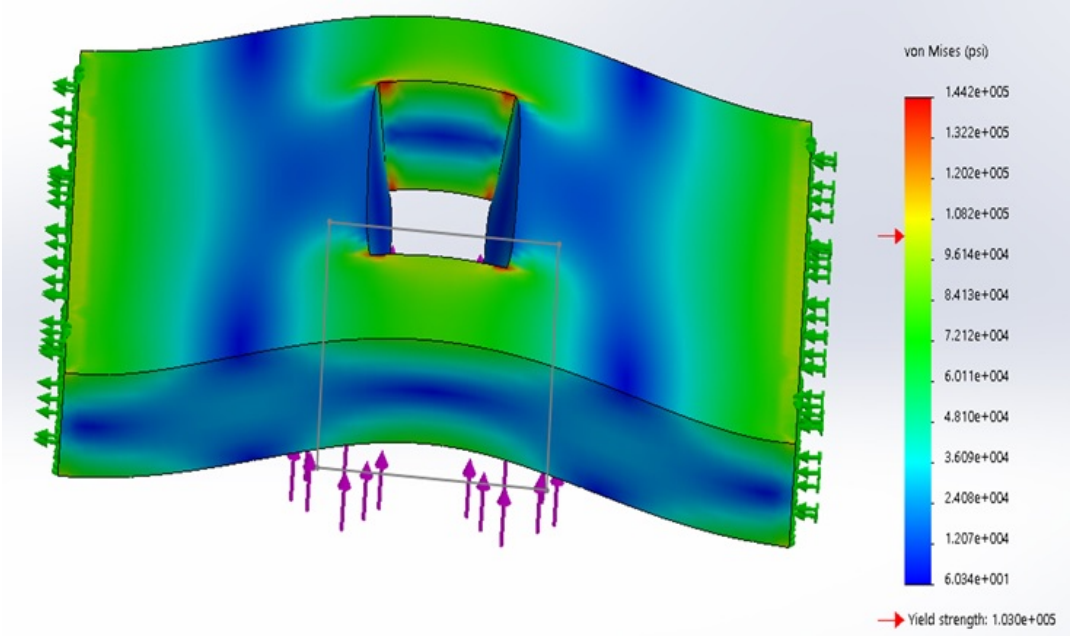

FIGURE A.5: Yield Stress and Von Mises stress simulation on the stainless steel top plate.

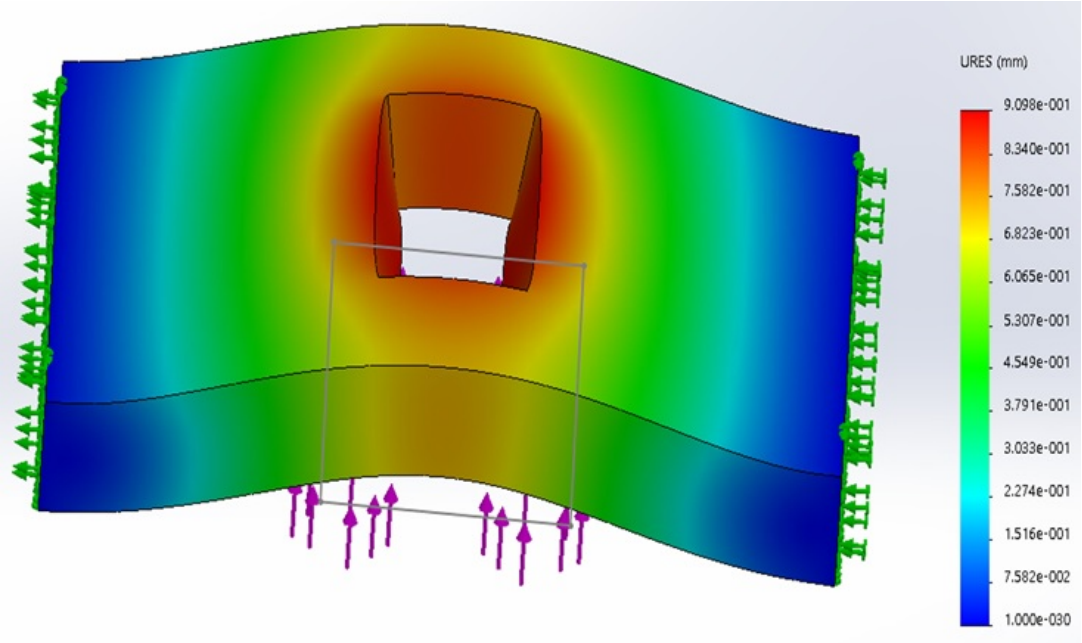

FIGURE A.6: Displacement of top plate under simulated load of chamber pressurized to 35 MPa (5,000 psi) with a safety factor of 2.

Under loads produced from a pressure of 35 MPa (5,000 psi), the clamping plate was far below the yielding threshold as shown in Figures A.5 and A.6. Additionally, the deflection near the o-ring was lower than the tolerable 0.3 mm at this condition. A major difficulty in applying shear to a pressurized system is maintaining pressure through the shaft entrance. The shaft must reciprocate in and out of the chamber in order to shear the sample. Figure A.7 shows the components for maintaining the dynamic seal between the shaft and the chamber.

A.4.2 Function II: Applying a Uniform Simple Shear Flow to the Saturated Plastic Melt

Shearing of the sample was achieved using an Oriental Motor (ARM66AC) stepper motor attached to an external frame which translated linear motion to the sample, as outlined in Anson's Thesis (Wong et al. 2011). The speed of the motion can be controlled through changing the parameters Hz and Steps in the MEXE02 software. The Hz parameter is directly proportional to the linear speed, and the Steps

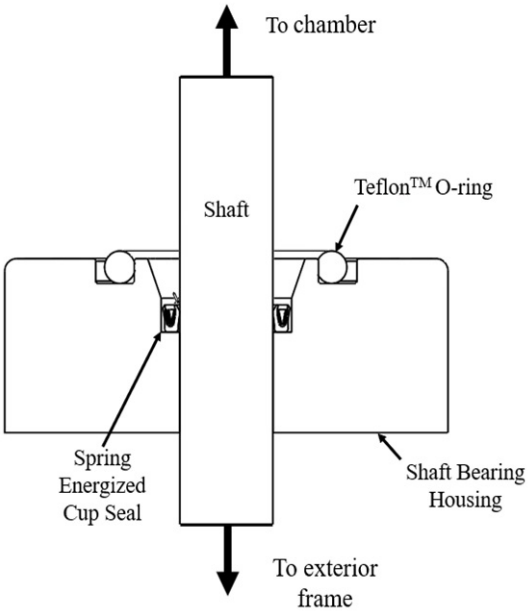

FIGURE A.7: Shaft seal design

parameter is directly proportional to linear translation of the sample.

During experimentation, known amounts of shear strain at a specific shear rate are exerted on the loaded sample. For verification of the linear travel distance and velocity of the step motor, an Omega LD620-50 LVDT was used in conjunction with a Measurement Computing USB-2408-2a0, with a resolution of approximately $\pm$ 0.7 mV. In principle, an LVDT provides a voltage output proportional to the position of the rod. When mounted parallel to the frame, linear displacement of the frame will cause an equivalent change in the position of the rod of the LVDT. By collecting the change in the voltage output of the LVDT with varying distance, conversion factors for motor position in steps to linear displacement in mm was obtained, as well as a conversion factor for LVDT voltage output to linear displacement in mm. Specifically, conversion factors of 10.054 mm to 1 V, 1674.7 step to 1 V, and 166.57 step to 1 mm were obtained, allowing for precise calculation of shear strain and position verification of the sample during experimentation (see Fig. A.8).

The quotient of the desired strain and the sample thickness (mm) yields the required linear displacement of the motor (mm), conversion factors obtained by the

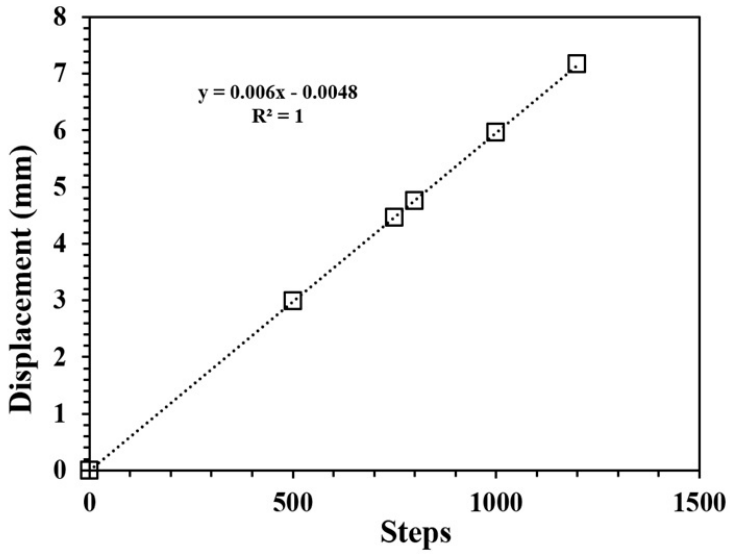

FIGURE A.8: Displacement to steps (motor) calibration

LVDT produce reliable means of programming the motor to achieve the desired strain.

Precise measurement of the linear velocity of the motor is required. During experimentation, a linear relationship of position of the frame versus time was observed, allowing the slope of the relationship to represent the derivative of the function as shown in Figure A.9.

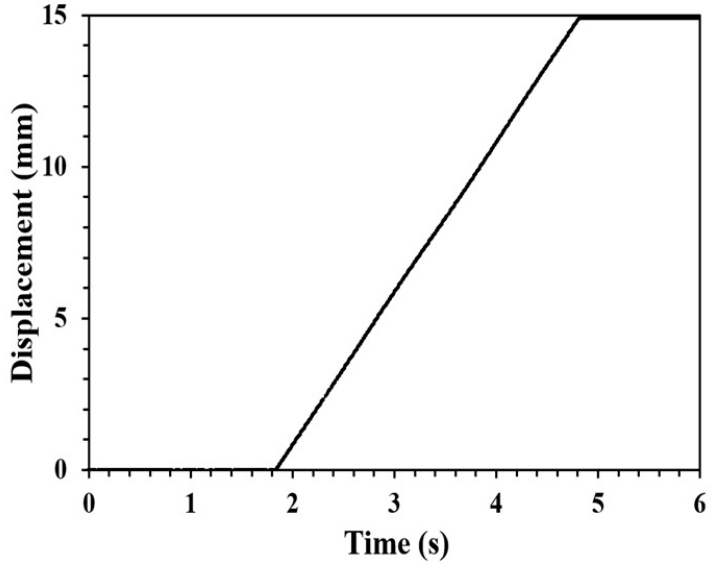

FIGURE A.9: Resultant displacement curve due to programmed 15 mm displacement at a speed of 5 mm/s

As such, velocity of the motor was obtained by averaging the slope of this relationship among several trials. Comparing the calculated linear velocity of the frame to the speed input (Hz) of the motor, a conversion factor of 166.57 Hz to 1 mm/s was obtained as shown in Figure A.10.

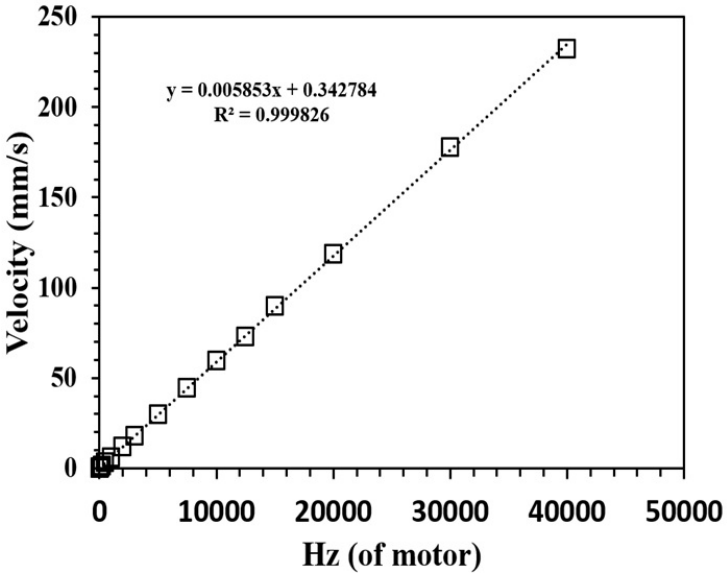

FIGURE A.10: Velocity to Hz (motor) calibration

By taking the quotient of the desired shear rate and sample thickness (mm), the required linear velocity of the motor (mm/s) can be calculated. Using this conversion factor, use of an LVDT provides a meaningful way to calculate the required speed input (Hz) required of the motor to achieve the desired shear stress.

A.4.3 Function III: Accurate Heating and Cooling

The chamber was equipped with a CN 7523 proportional–integral–derivative (PID) controller from Omega, which controlled four 500W ceramic cartridge heaters in the chamber body of the HP-SPC. Two 150W fans were attached to HP-SPC and controlled by the same PID controller through the dual heating and cooling setting. Additionally, two thermocouples (Omega PT110) were placed near the sample area and in the chamber body to monitor temperatures during both heating and cooling.

The system was capable of linear heating up to 15°C/min and linear cooling up to 5°C/min with proper parameter inputs.

A.4.4 Function IV: Capturing Crystal Nucleation and Growth Processes with Fine Spatial Resolution

Crystal size, density, and orientation are important morphological aspects that determine physical properties of the polymer. These properties include: mechanical strength, optical, thermal, acoustic, and oxygen barrier properties that are essential to the functionality of polymer products. As such, they are of particular interest for study in the HP-SPC.

A.4.5 Function V: Measuring Local Shear Stress

Rheology equipment utilizes torque transducers to measure the response of the polymer melt. In a parallel plate geometry J.M. Dealy developed a force transducer that measures local shear stress of a polymer melt undergoing simple shear, otherwise known as a Shear Stress Transducer (SST) (Park and Dealy 2006). The SST acts as a disk-spring between the polymer melt and a measurement apparatus. As the polymer melt drags along the surface of the SST, it engages its so-called active face, causing a moment about a torsion bar. This results in deflection of the target, measured using a gap displacement technique.

For precise deflection measurements, a Capacitec 4100S series Non-Contact Gap Measurement Amplifier was utilized. In theory, a displacement sensor is held parallel to a target and connected to a driver, which provides a voltage readout based on the linear distance between the probe and target face. When the target is deflected, the change in the distance from the target face to the probe face yields a measurable change in voltage.

To calibrate the system, the SST was fitted with an identical calibration head of equal mass and dimension. A small screw was affixed to the center of the calibration head and tightened on the active face in order to secure a high-tension line (see Fig.

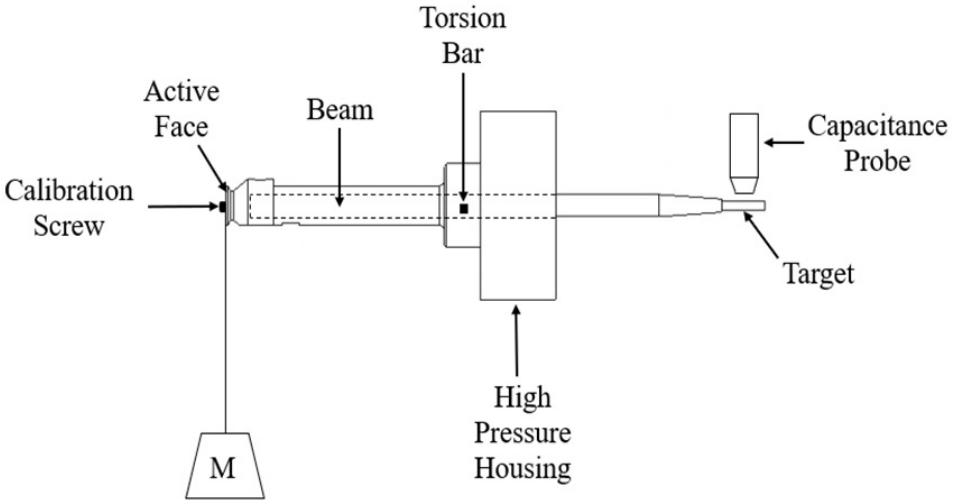

FIGURE A.11: SST Design and Application

A.11). Weights of known mass were attached to the line and hung from a pulley system within the HP-SPC as shown in Figure A.11. For our calibration purposes, 10 g, 20 g, 50 g, 100 g, 200 g, 500 g, and 1000 g weights were utilized.

Due to changes in thermal expansion, the calibration procedure must be done for all testing temperatures. In this setting, we calibrated the system at 200 °C and atmospheric pressure. Note that the method employed only works for atmospheric conditions. Any high pressure conditions are assumed to follow a similar trend, but would have to be calibrated using another method (spring, etc.). Figure A.12 shows the relationship between simulated stress and the resultant voltage. The simulated stress is a function of the hanging mass (M) and the area of the active face (A_a), $\sigma = Mg/A_a$. Due to the applied force to the calibration head being perfectly flush with the force exerted by a sheared polymer melt, the simulated stress and the measured stress during testing will be equal. The specific deflection properties of the SST are due to the material (305 stainless steel) and the rigidity of its components.

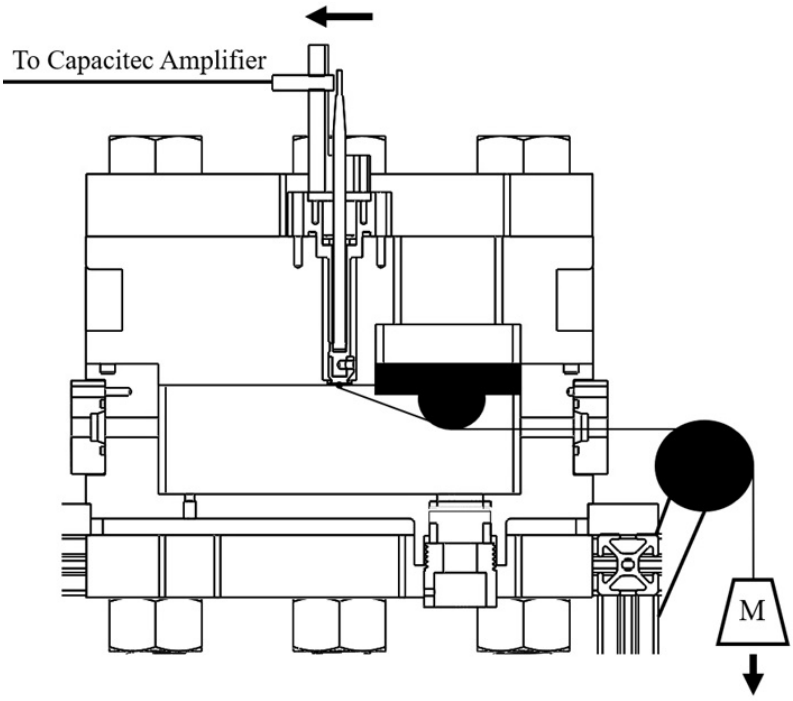

FIGURE A.12: HP-SPC in calibration configuration

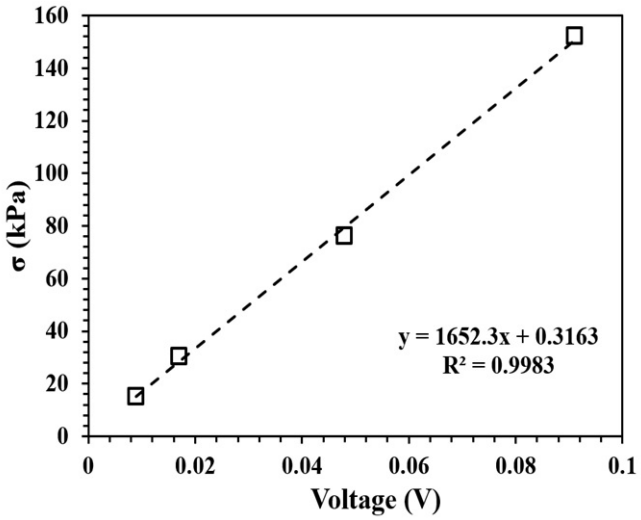

FIGURE A.13: SST Calibration curve at 200 °C and atmospheric pressure

A.5 Discussion

Although the visualization capability of this system is proven, and the calibration of the SST is possible, therein lies complexity in ascertaining proper rheological

data. Like all rheological equipment, precision and accuracy of the applied condition and measured torque signal are essential to the validity of any obtained data. As such, this study discovered that there are many improvements to be made to the current SST that would help prove its capabilities. Force measurements made through the SST can be distorted in many ways, both mechanical and electrical. While some factors are more influential than others, the sensitivity of the measurement requires attention to all aspects of the system. We have identified some root causes for the discrepancy between the theoretical and experimental signals.

1. Perfect XY plane parallelism between the probe and target face.
2. Effect of concentricity of active face relative to its position along the sliding surface.
3. Rigidity of the torque bar in the SST. This will change bending characteristics.
4. The effect of lubricant on all sliding surfaces, and how it impacts mechanical noise.
5. Improvement of signal resolution to obtain clearer data for lower shear rates.
6. Parallelism of the top and bottom plate.
7. Monitoring motor performance.
8. Isolating the SST from mechanical vibrations in surroundings.
9. Temperature variation in chamber.
10. Ability to maintain sample thickness during experimentation.

A.6 Conclusions

A high pressure sliding plate chamber (HP-SPC) was designed and proven to produce high resolution images of crystallization processes. Additionally, initial

calibrations were made of the shear stress transducer (SST) employed to measure local shear stress of molten polymer flows. Once proven, this system will have dual capability of visualizing and measuring polymer processes under pure shear. This will better our understanding of how explicitly shear affects polymer flows under the complex stress field experienced during industrial settings.

Appendix B

Scanning Electron Microscopy

Series of micrographs of batch foaming for low and high viscosity polystyrene are presented. Micrographs were taken under polarized optical microscope (POM) every 0.4 s per frame. Each micrograph was analyzed using an image processor in order to count the number of cells and cell size over time. Matlab codes for image process analysis and simulation of cell growth are presented here.

B.1 Low Viscosity Polystyrene (PS) - POM Images

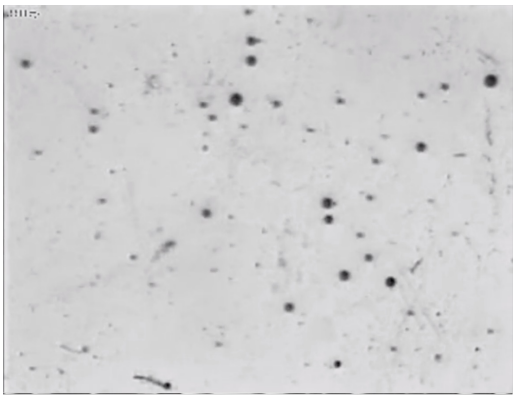

Frame Nr. 120

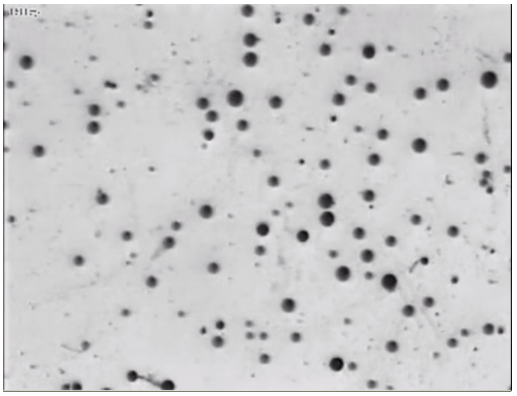

Frame Nr. 140

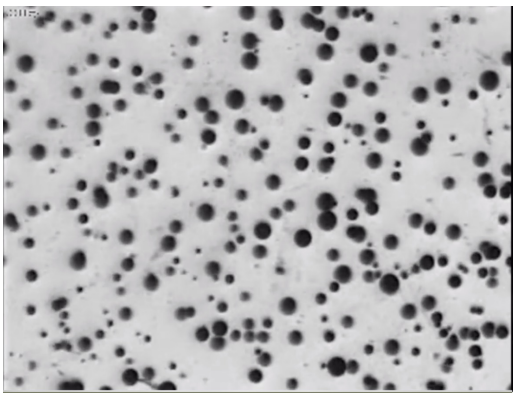

Frame Nr. 160

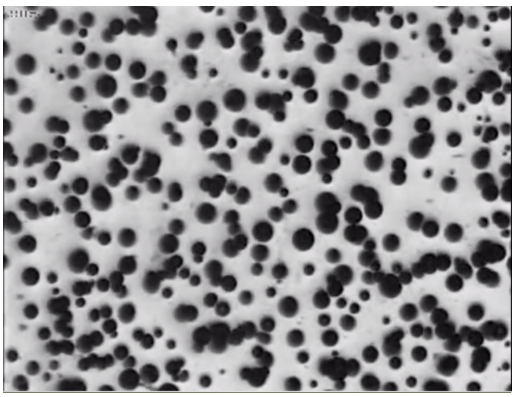

Frame Nr. 180

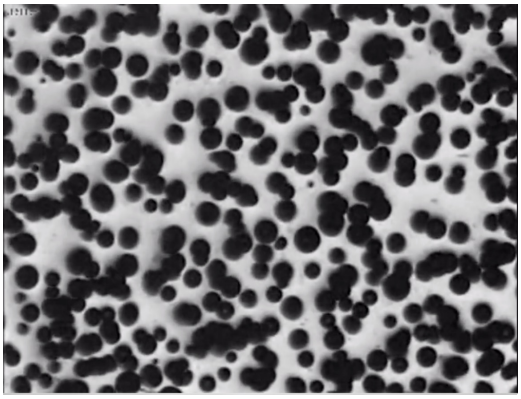

Frame Nr. 200

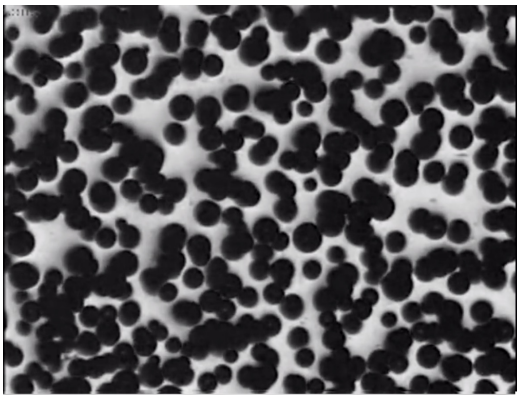

Frame Nr. 220

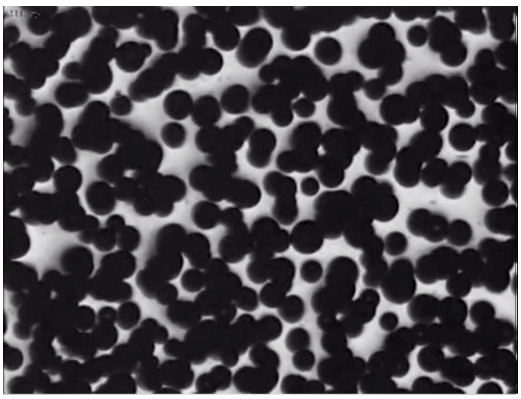

Frame Nr. 240

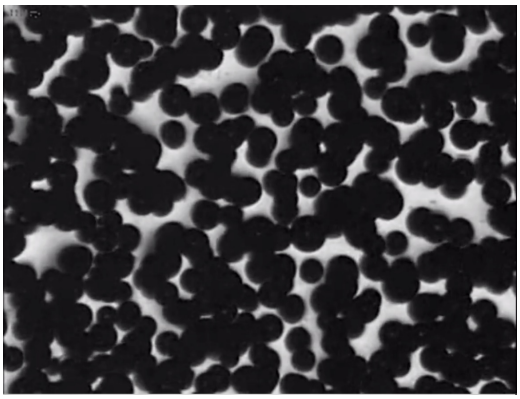

Frame Nr. 260

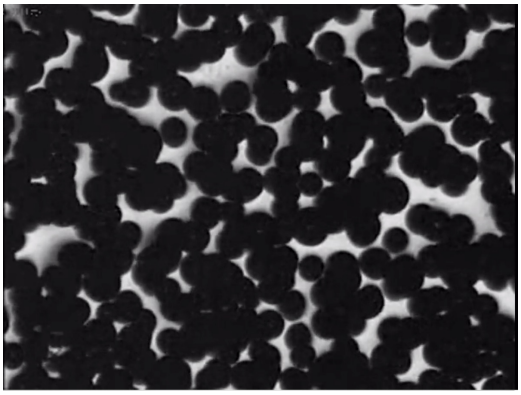

Frame Nr. 280

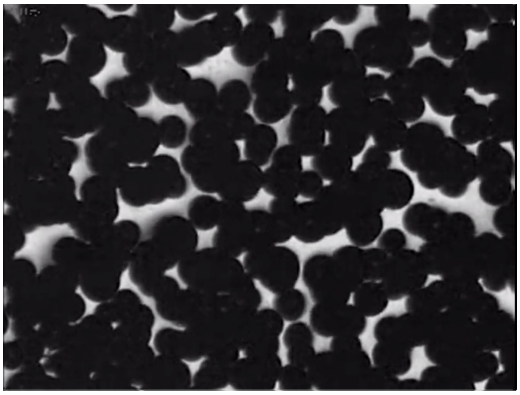

Frame Nr. 300

High Viscosity Polystyrene (PS) - POM Images

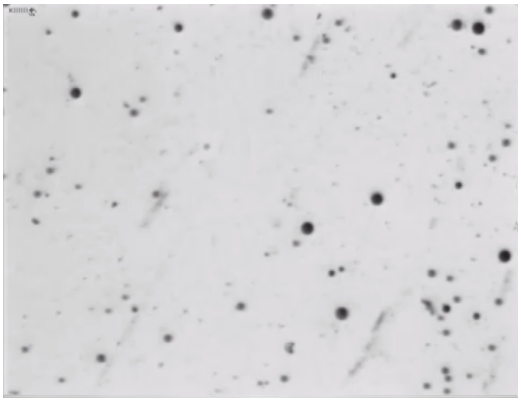

Frame Nr. 120

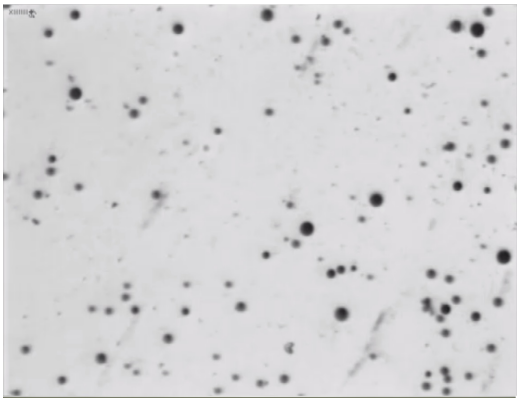

Frame Nr. 140

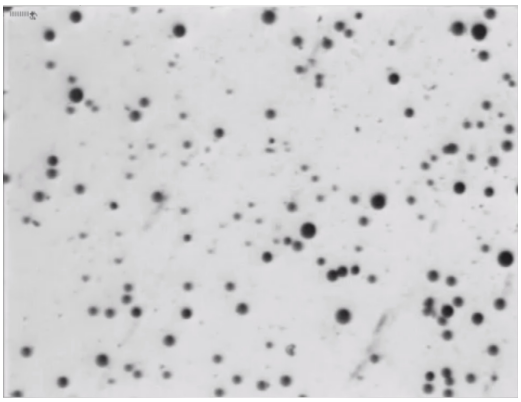

Frame Nr. 160

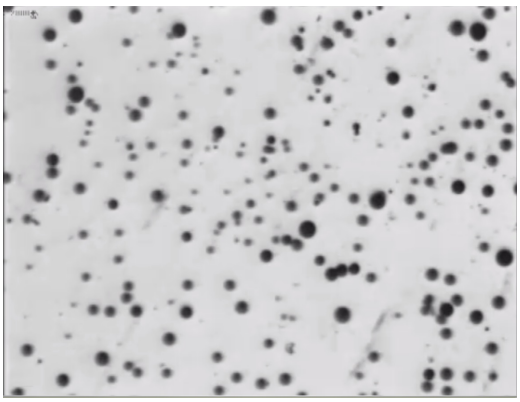

Frame Nr. 180

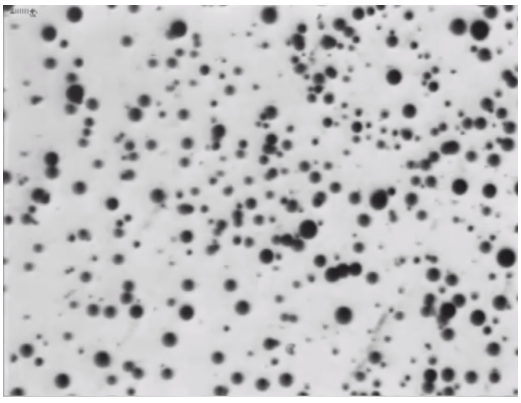

Frame Nr. 200

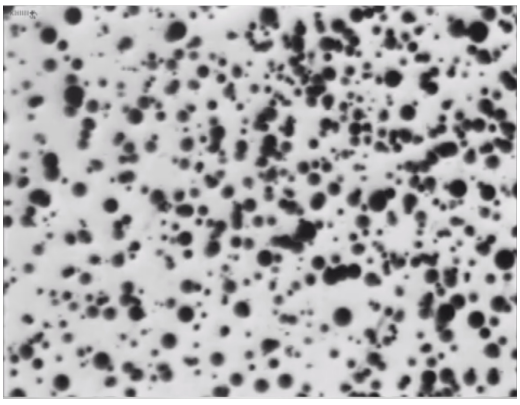

Frame Nr. 220

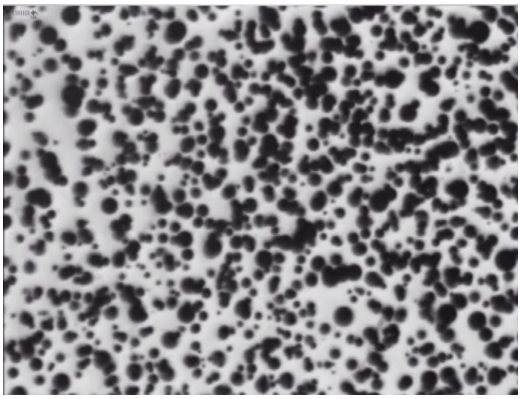

Frame Nr. 240

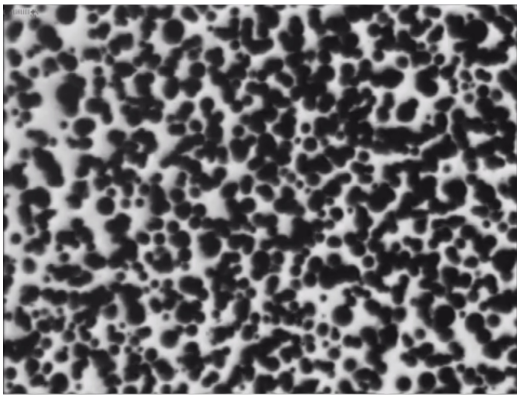

Frame Nr. 260

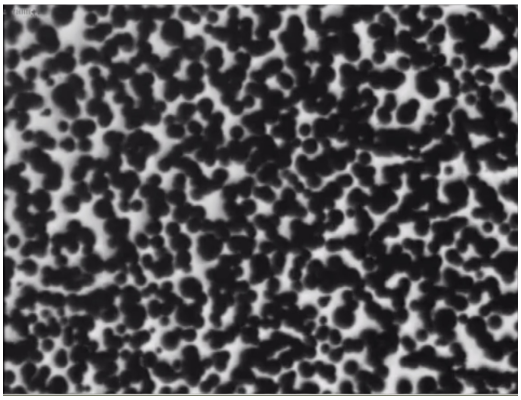

Frame Nr. 280

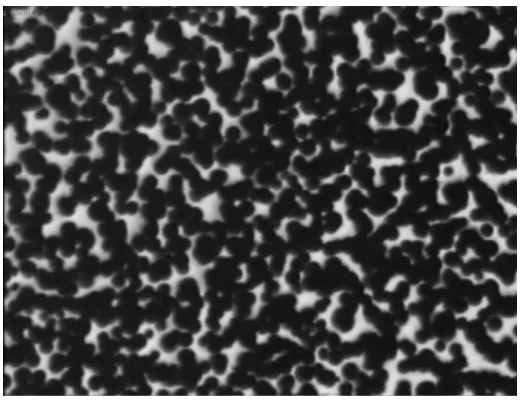

Frame Nr. 300

Process Image Analysis - Matlab Code

```
close all
clear all

A = imread('WB140.jpg');
figure,imshow(A)
A = imcomplement(A);
figure, imshow(A)
I = rgb2gray(A);
figure,imshow(I)
I = adapthisteq(I);
figure,imshow(I)
I = imclearborder(I);
figure,imshow(I)
I = wiener2(I, [5 5]);
figure,imshow(I)
bw = im2bw(I, graythresh(I));
figure,imshow(bw)
bw2 = imfill(bw,'holes');
figure,imshow(bw2)
bw3 = imopen(bw2, strel('disk',2));
figure,imshow(bw3)
bw4 = bwareaopen(bw3, 100);
figure,imshow(bw4)
bw4_perim = bwperim(bw4);
figure,imshow(bw4_perim)
%overlay1 = imoverlay(I, bw4_perim, [1 .3 .3]);
%figure,imshow(overlay1)
```

```
28 % Discover putative cell centroids
29 maxs = imextendedmax(I,  5);
30 %figure,imshow(maxs)
31 %maxs = imclose(maxs, strel('disk',3));
32 %figure,imshow(maxs)
33 %maxs = imfill(maxs, 'holes');
34 %figure,imshow(maxs)
35 maxs = bwareaopen(maxs, 2);
36 figure,imshow(maxs)
37 %overlay2 = imoverlay(I, bw4_perim | maxs, [1 .3 .3]);
38 %figure,imshow(overlay2)
39 % modify the image so that the background pixels and the
       extended maxima pixels are forced to be the only local
       minima in the image.
40 Jc = imcomplement(I);
41 figure,imshow(Jc)
42 I_mod = imimposemin(Jc, ~bw4 | maxs);
43 figure,imshow(I_mod)
44 L = watershed(I_mod);
45 figure,imshow(L)
46 labeledImage = label2rgb(L);
47 figure,imshow(labeledImage)
48 [L, num] = bwlabel(L);
49
50 % Area of cells
51 stat = regionprops(bw2,'Area','PixelIdxList');
52 [maxValue,index] = max([stat.Area]);
53 %[a,b]=hist(y,unique(y));
```

Cell Growth Modeling - Matlab Code

```
clf
clear all
close all

n=1000;

Plightning = .000007; %.000005;
Pgrowth = .007; %.01

z=zeros(n,n);
%o=ones(n,n);
veg=z;
sum=z;


imh = image(cat(3,z,veg*.02,z));
set(imh, 'erasemode', 'none')
axis equal
axis tight

% burning -> empty
% green -> burning if one neigbor burning or with prob=f (
    lightning)
% empty -> green with prob=p (growth)
% veg = {empty=0 burning=1 green=2}
rho = zeros(001,300);
cells = zeros(1,300);
```

```
27 Num = zeros(1,300);
28 L = zeros(1,300);
29  for i=1:1000 %200
30     %nearby  fires?
31
32     sum = (veg(1:n,[n 1:n-1])==1) + (veg(1:n,[2:n 1])==1) +
           ...
33             (veg([n 1:n-1], 1:n)==1) + (veg([2:n 1],1:n)==1) ;
34
35     veg = ...
36           2*(veg==2) - ((veg==2) & (sum>0 | (rand(n,n)<
                Plightning))) + ...
37           2*((veg==0) & rand(n,n)<Pgrowth) ;
38
39     set(imh, 'cdata', cat(3,(veg==1),(veg==2),z) )
40     drawnow
41
42     % compute density
43     a = unique(veg);
44     k = find(a==1);
45     out = [a,histc(veg(:),a)];
46
47     % label connected components found in the binary image
48     cc = bwconncomp(veg);
49     labeled = labelmatrix(cc); %create label matrix with the
          connected components
50     cells(:,i) = cc.NumObjects;
51
52     %the area of all objects in the image is calculated
```

```
53      l=bwlabel(veg);
54      %stat = regionprops(l,'Area','PixelIdxList','Centroid
            ',...
55      %'MajorAxisLength'); % Area of cells
56      %stat = regionprops(l,'MajorAxisLength');
57      % Compute number of elements = burning
58      %[L, num] = bwlabel(l);
59      %MajorAxisLength(i) = stat.MajorAxisLength;
60      %Area(i) = stat.Area;
61      if isempty(k)==1
62          rho(:,i) = 0;
63      else
64          rho(:,i) = out(k,2);
65      end
66
67  end
68
69  % pseudo-color image, where the label identifying each object
        in the label
70  % matrix maps to a different color
71  figure;
72  RGB_label = label2rgb(labeled, @copper, 'c', 'shuffle');
73  imshow(RGB_label,'InitialMagnification','fit')
```

Appendix C

Design of Experiments (DOE)

Design of experiments using JMP with material, CBA content, talc content, foaming pressure and pressure drop rate, and foaming temperature as independent variables. The activation time of the CBA, saturation time of the sample were selected as dependent variables for this study.

Exp #	Material	CBA (%)	Talc (%)	Foaming Pressure (MPa)	Pressure Drop Rate (MPa/s)
1	MFX6	3	0.5	10.34	47.41
2	MFX6	0.5	3	17.24	47.41
3	PDH025	0.5	1.5	24.13	47.41
4	PDH002	3	0.5	17.24	153.9
5	PDH002	3	3	17.24	153.9
6	PDH025	3	0.5	10.34	47.41
7	MFX6	3	3	10.34	47.41
8	MFX6	3	1.5	24.13	47.41
9	PDH002	0	0.5	10.34	153.9
10	PDH025	1.5	0	10.34	47.41
11	WB140	3	3	10.34	153.9
12	MFX6	3	1.5	24.13	47.41
13	PDH002	3	3	24.13	153.9
14	WB140	0	1.5	17.24	153.9
15	WB140	0	1.5	17.24	153.9
16	WB140	0.5	3	17.24	153.9
17	WB140	3	3	10.34	153.9
18	PDH025	1.5	3	17.24	153.9
19	PDH002	0.5	0	17.24	153.9
20	MFX6	1.5	3	24.13	47.41
21	PDH025	0.5	0.5	17.24	47.41
22	WB140	1.5	1.5	10.34	153.9
23	PDH025	1.5	3	24.13	47.41
24	MFX6	1.5	0.5	24.13	153.9
25	MFX6	1.5	0.5	24.13	153.9
26	PDH002	3	0	24.13	153.9
27	WB140	0	0.5	17.24	153.9
28	PDH025	0	3	17.24	47.41
29	MFX6	0	0	24.13	47.41
30	PDH002	3	3	24.13	153.9
31	WB140	0	0.5	17.24	153.9
32	WB140	1.5	1.5	24.13	153.9
33	PDH025	3	0	10.34	47.41
34	PDH002	1.5	1.5	24.13	153.9
35	WB140	3	0.5	17.24	153.9